December 2017

# Polaron Dynamics in Conjugated Polymer Nanoparticles and Applications in Superresolution Imaging

Yifei Jiang
*Clemson University*, YIFEIJ@CLEMSON.EDU

Follow this and additional works at: https://tigerprints.clemson.edu/all_dissertations

POLARON DYNAMICS IN CONJUGATED POLYMER NANOPARTICLES AND
APPLICATIONS IN SUPERRESOLUTION IMAGING

A Dissertation
Presented to
the Graduate School of
Clemson University

In Partial Fulfillment
of the Requirements for the Degree
Doctor of Philosophy
Chemistry

by
Yifei Jiang
December 2017

Accepted by:
Dr. Jason McNeill, Committee Chair
Dr. Jeffrey Anker
Dr. Leah Casabianca
Dr. Steven Stuart

## ABSTRACT

Charge carrier dynamics in conjugated polymers are of fundamental interest as they directly affect the performance of conjugated polymer based devices. Through efficient fluorescence quenching by hole polarons, dynamics of individual charge carriers, including generation, recombination, and transport, can be observed through single particle fluorescence study of conjugated polymers nanoparticles (CPNs). In this dissertation, the hopping dynamics of hole polarons in CPNs were studied using superresolution microscopy. Due to quenching of the local fluorescence, a hole polaron can form a "dark spot" that moves with the polaron and results in displacements in the fluorescence centroid. These position fluctuations were used to track the nanoscale motion of hole polarons. In long trajectories, we observed random walk-like behavior consistent with multiple trap sites, whereas in some short segments, repeated hopping between two traps was observed. The hopping times range from a few ms to seconds, following a power law distribution, while the hopping distances range from 2-5 nm, following an exponential distribution. From the hopping time distribution, we estimated the energy barrier height for polaron hopping in CPNs to be from 430 to 570 meV, indicating the presence of deep traps with nearest-neighbor distances of 2-5 nm, consistent with a low or moderate density of structural or chemical defects dominating charge transport at low carrier densities.

Based on polaron generation and recombination dynamics, we developed a new class of photoswitchable nanoparticles for superresolution imaging. By doping nanoparticles of conjugated polymer PFBT with fullerene derivative PCBM, a large population of

polarons can be efficiently generated in CPNs, sufficient to nearly completely quench the nanoparticle fluorescence. However, fluctuations in the number of quenchers lead to occasional bursts of fluorescence. $3\text{-}5 \times 10^4$ photons were detected during each burst event (1-2 orders of magnitude brighter than photoswitchable dyes), resulting in a localization precision of 0.6 nm, ~4 times better than the typical resolution obtained by localization of dye molecules. In addition, since polaron generation is a photo-driven process, we demonstrated that the blinking duty cycle of PCBM doped CPNs can be controlled by excitation intensity as well as by PCBM fraction. The unprecedented brightness and tunable spontaneous photoswitching properties of PCBM doped PFBT CPNs make them a promising class of superresolution probes, which provide clear advantages for imaging of various biological systems.

ACKNOWLEDGMENTS

During my time at Clemson University, I have made lots of friends and received help from many people. I want to thank all of them, even though I only have space to mention a few in this dissertation.

It has been a lot of fun working in Dr. Jason McNeill's lab. I would like to thank him for all the compounds, optics, cables that I purchased, for the time he spent editing my manuscripts, and for his sound advises about my research as well as career. I enjoyed talking to him about science and research because he always has some good stories to share. I have learnt a lot from him and am eternally grateful for the experience.

The McNeill's group is populated by great people. Louis Groff, Xiaoli Wang, Teeranan Nongnual, Amirhossein Jafariyan and Muskendol Nova have all given me great help in research. Outside of lab, we also shared lots of good memories (and food). I want to thank Louis for the bulgogi beef, thank Teeranan for the mango sticky rice, thank Xiaoli for the cucumbers that she grew, thank Amir for the kabab barg.

I have also made many friends while working in the physical chemistry lab, including Umesh Shrestha, Sidath Wijesinghe, Justin Talbert, and many others. I want to thank them for their help in lab management and their friendship.

I would also like to thank my committee, Dr. Jeffrey Anker, Dr. Leah Casabianca, and Dr. Steven Stuart, for their patience and guidance. I appreciate the research advises they gave me and their support in my search for post-doc positions.

Finally, I want to thank my girlfriend, Yu Shen, for her unconditional support throughout my graduate education. I also want to thank my family for letting me follow my own path. I wouldn't be able to accomplish this without their encouragement.

TABLE OF CONTENTS

Table of Contents (Continued)

LIST OF TABLES

LIST OF FIGURES

List of Figures (Continued)

List of Figures (Continued)

List of Figures (Continued)

CHAPTER ONE

INTRODUCTION

## 1.1 Overview

## 1.1.1 Conjugated Polymers

In recent years, conjugated polymers have been employed in a variety of electro-optical applications, including photovoltaic devices,[1-3] field-effect transistors,[4-6] light-emitting diodes (LEDs)[7-9] as well as fluorescent nanoparticles[10-12] and nanoscale sensors[13, 14]. Conjugated polymers exhibit high absorption coefficients with electronic band gaps ranging from UV to near infrared. The HOMO and LUMO gap of conjugated polymers can be fine-tuned by controlling side chain interactions and inclusion of heteroatoms.[15, 16] When doped with fullerene derivatives, photon energy can be efficiently converted to electricity through electron transfer from the conjugated polymers to the dopant species.[17, 18] In addition, the good flexibility and processability of conjugated polymers makes them ideal materials for thin-film electronic devices.[19, 20] Due to the high degrees of conformational freedom of conjugated polymer chains and the weak inter-chain interactions, the structures of conjugated polymer films are typically heterogeneous, including both crystalline and disordered regions.[5, 21, 22] The complexity of the structure reduces the generation/transport efficiency of charge carriers in conjugated polymer solar cells and limits the quantum efficiency of conjugated polymer based LEDs.[9, 23] Further development of conjugated polymer devices requires better control over the film morphology as well as deeper

understanding of the structure-property relationship. In this dissertation, through the studies of nanoscale aggregates consisting of a small number of conjugated polymer chains, we hope to provide a unique window for various photophysical processes in conjugated polymer devices.

### 1.1.2 Conjugated Polymer Nanoparticles

Conjugated polymer Nanoparticles (CPNs) are formed by one or more aggregated hydrophobic conjugated polymer chains. Due the high extinction coefficient and the high chromophore density of conjugated polymers, CPNs are the brightest fluorescent nanoparticles within its size range (one or two orders of magnitude brighter than similar-sized colloidal semiconductor quantum dots or dye loaded silica nanoparticles under typical imaging conditions).[10, 24, 25] CPNs also exhibit good photostability (~$10^9$ photons emitted before photobleaching) and high saturated emission rates (on the order of $10^8$ s$^{-1}$),[10, 26] which makes it suitable for fast applications involving high excitation intensities, such as flow cell cytometry and fast particle tracking. Using a co-precipitation method, dopant species can be easily incorporated into CPNs to red-shift the emission,[27, 28] improve photostability[25] or provide sensing/photoswiching capabilities[13, 29]. CPNs exhibit many interesting and useful photophysical properties, including highly efficient energy transfer,[11, 30] anomalous fluorescence blinking,[31] and energy cascade to low energy emitters.[32] These phenomena are dictated by interactions between densely-packed polymer chains as well as dynamics of various photogenerated species. In order to tune CPNs for specific applications, it is critical to obtain better understanding of various

photophysical processes in conjugated polymers, such as exciton diffusion, energy transfer, charge generation and charge transport, and how nanostructure dedicates these processes. In this dissertation, we will use single molecule spectroscopy as a method to characterize various photophysical dynamics in CPNs and use the knowledge gained to design photoswitchable CPNs for superresolution imaging.

### 1.1.3 Structure of CPNs

The diameter of CPNs typically ranges from a few to hundreds of nanometers, depending on the preparation method. CPNs can exhibit various aspect ratios at different size ranges.[33] Typically, at smaller sizes (<50 nm in diameter), a spherical conformation is expected since interfacial tension dominates at high surface to volume ratios. The overall shape of larger CPNs is also controlled by the rigidity of the polymer backbone and the chain-chain interactions. Through self-assembly method or using substrate, nanostructures with very high aspect ratios, such as nanorod,[34] nanofiber,[35] can be prepared from poly(3-hexylthiophene) (P3HT). Chain packing inside CPNs typically ranges from semi-crystalline to highly disordered.[36, 37] The ordering of the polymer chains can be improved using solvent vapor annealing methods. As observed for poly(9,9-dioctylfluorene) (PFO) nanoparticles, addition and evaporation of organic solvents can induce the formation of the highly ordered β-phase.[36] CPNs prepared from certain conjugated polymers tend to have small crystalline regions as indicated by TEM studies.[37] Typically, the signature of J-aggregate is observed in the spectra of these CPNs,[36, 37] which is likely caused by a

combined effect of the higher fluorescence quantum yield of J-aggregates and the energy funneling from high energy chromophores to low energy J-aggregates. It is likely that both J- and H-aggregates are randomly formed inside CPNs, depending on local intra- and inter-chain coupling strength, as suggested by the study of highly ordered P3HT nanofiber.[35] The small crystalline regions could act as both exciton and polaron traps. The polaron trapping is due to the grain boundary between the crystalline and the glassy regions,[38] whereas the exciton trapping is due to the energy funneling effect.[32] The crystalline regions could be formed by several closely-packed polymer chains[37] or a single collapsed polymer chain[39]. As indicated by single molecule study of isolated polymer chains, conjugated polymers with tetrahedral defects can fold into highly ordered cylindrical conformations, resulting in red-shifted emission spectra.[39] In some cases, CPNs could adopt a kinetically trapped conformation. Solvent molecules and impurities could be trapped inside CPNs during the particle formation process. In addition, dopant molecules can also interrupt the chain packing inside CPNs and lead to formation of aggregation species.[40] Overall, there is still a lot to be learnt about CPNs structure. Improving our understanding of structure-optical property relationship is important to the continued development of conjugated polymer based fluorescence tags and sensors.

**1.2 Exciton Dynamics in CPNs**

**1.2.1 Frenkel Excitons in Conjugated Polymers**

In conjugated polymers, due to kinks, twists in the molecular backbones and thermal disorder caused by inter- and intra-molecular vibrations, polymer chains break into segments of various conjugation lengths (typically 2-10 monomer units), which are referred to as chromophores. Electronic transition from the HOMO to the LUMO states of a $\pi$-conjugated chromophores results in the formation of a neutral excited state, which could be shared among adjacent chromophores through strongly coupled transition dipoles, known as the Frenkel or molecular exciton.[41] Due to the effect of inter- and intra-chain coupling, conjugated polymers often exhibit optical properties that differ greatly from those of isolated chromophores, including red/blue shifts in the absorption and emission spectra,[42] changes in the radiative rate/fluorescence lifetime,[35] loss of vibronic structure,[43] etc. In order to provide a theoretical framework for understanding of these phenomena, we will present a dimer model, based loosely on the approach of Kasha, et al.[44] Key phenomena, including Davydov splitting, behavior of J/H aggregates, and coherent energy transport, will be discussed.

Here, we shall consider 2 identical chromophores at sites $a$ and $b$. The excitation at site $a$ is denoted by $|a\rangle$ and the excitation at site $b$ is denoted by $|b\rangle$. The dipole coupling between the two sites is introduced as a time-independent perturbation $\hat{V}$, which is given by,

$$\hat{V} = V_{ab}(|a\rangle\langle b| + |b\rangle\langle a|), \tag{1.1}$$

where $V_{ab}$ indicates the coupling strength, depending on the distance between the sites and the relative orientation of the transition dipoles. The dimer states are given by,

$$|+\rangle = \frac{1}{\sqrt{2}}(|a\rangle + |b\rangle), \tag{1.2}$$

$$|-\rangle = \frac{1}{\sqrt{2}}(|a\rangle - |b\rangle), \tag{1.3}$$

where $|+\rangle$ corresponds to a state with the dipoles oscillating in-phase, $|-\rangle$ corresponds to a state with the dipoles oscillating out-of-phase, respectively. The energies of the states $|+\rangle$ and $|-\rangle$ are given by,

$$E_\pm = \hbar\omega_0 \pm V_{ab}, \tag{1.4}$$

where $\hbar\omega_0$ is the eigenvalue of the unperturbed Hamiltonian. The splitting in the excited state energy $2V_{ab}$ is referred to as the Davydov splitting.[45] For J-aggregates, the transition dipoles are oriented head-to-tail (Fig. 1.1), which results in a negative $V_{ab}$ value. In such case, the state $|+\rangle$ is lower in energy and has a higher net transition dipole moment than that of the isolated chromophore, whereas the state $|-\rangle$ has higher energy and a much smaller net transition dipole moment. Since radiative rates are proportional to the transition dipole moment squared, J-aggregates exhibit strong, red-shifted absorption/fluorescence emission and reduced fluorescence lifetime.[44] For H-aggregates, the transition dipoles are oriented face-to-face and the $V_{ab}$ value is positive (Fig 1.1). In such case, the in-phase $|+\rangle$ state is higher in energy, which results in the blue-shifted absorption/fluorescence spectra. Due to relaxation to the out-of-phase $|-\rangle$ state and its low overall transition dipole moment, H-aggregates typically exhibit low fluorescence quantum yields.[44]
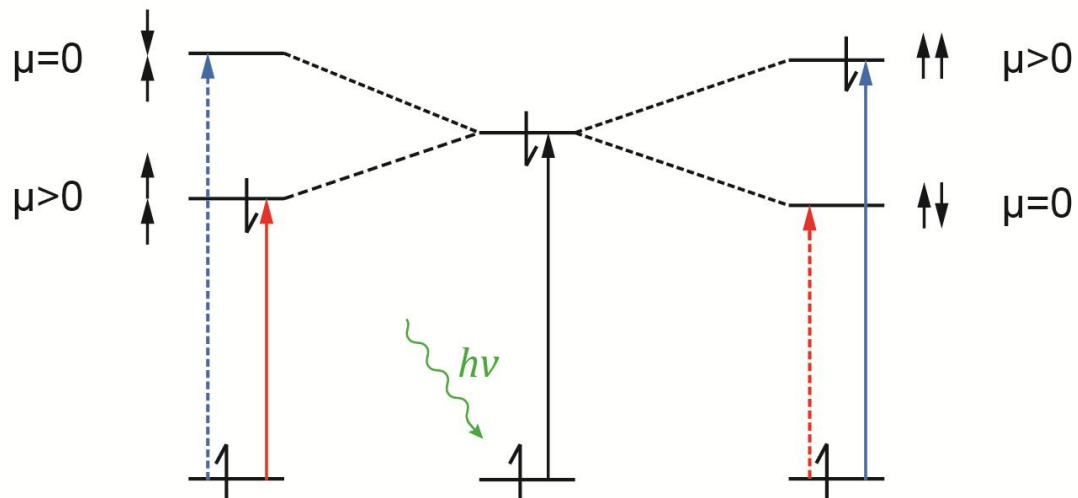
**Figure 1.1** Energy diagrams of an isolated chromophore (middle), J-aggregate (left) and H-aggregate (right). The allowed transitions are given by the solid arrows and the forbidden transitions are given by the dashed arrows. For each state, the corresponding dipole orientation is given next to it.

Above, we considered the dipole coupling as a time-independent perturbation, which leads to the Davydov splitting and red/blue shifts in the absorption and emission spectra. If we introduce the dipole coupling as a time-dependent perturbation, we shall see that the excitation is shared among the two chromophores. If we assume that excitation is at site $a$ at t=0, following the time-dependent perturbation theory, we obtain the probability that the excitation is at site $b$ some later time in the following functional form,

$$P_b = |\langle a|\hat{V}|b\rangle|^2 = sin^2\left(\frac{V_{ab}t}{2\hbar}\right). \tag{1.5}$$

As indicated by the equation 1.5, the excitation oscillates between the two chromophores with a frequency of $V_{ab}/\hbar$. For systems with 3 or more chromophores, the sign and magnitude of the transition dipole coupling term can vary for each pair of chromophores, which add complexity to the solution. However, the basic physical picture is still the same that the excitation can oscillate between multiple strongly coupled chromophores. For systems with higher dimensions, the excitation can be shared among multiple axes. For example, in the case of polymer $\pi$-stacks, the excitation can oscillate along the polymer backbone as well as across the polymer chains within the stack.[46]

Similarly, using the non-degenerate perturbation theory, we can obtain the solution for a dimer system with energetic disorder. In such case, the splitting in the excited state energy is reduced as compared to the degenerate dimer. If we assume that $\hbar\omega_a$ and $\hbar\omega_b$ are the eigenvalues of the unperturbed Hamiltonian and site $a$ has higher energy, the first order energies of the perturbed Hamiltonian are given by,

$$E_+ = \hbar\omega_a + \frac{V_{ab}^2}{\hbar\omega_a - \hbar\omega_b}, \tag{1.6}$$

$$E_- = \hbar\omega_b - \frac{V_{ab}^2}{\hbar\omega_a - \hbar\omega_b}. \tag{1.7}$$

As shown by the equations 1.6 and 1.7, the energetic disorder reduces the effect of dipole coupling between the chromophores, resulting in a smaller Davydov splitting and less symmetric wavefunctions. When the coupling strength is small comparing to the energetic disorder between the chromophores, the energy transfer is incoherent, as describe by Förster's theory, which we will discuss in the next section.

### 1.2.2 Förster Resonance Energy Transfer

Förster Resonance Energy Transfer (FRET) is developed by Theodor Förster in the 1940s to describe long-range (<10 nm), incoherent energy transfer occurring through weak dipole coupling.[47] In this mechanism, energy transfer can either occur between identical chromophores (homo-FRET) or chemically distinct chromophores (hetero-FRET). As discussed in the previous section, in conjugated polymers, due to structural/energetic disorder and exciton-phonon coupling, the excitation is localized and exhibit fast coherent transfer between strongly coupled chromophores and slower incoherent transfer between weakly coupled chromophores through the Förster mechanism. At high temperatures, inter- and intra-molecular vibrations destroy the coherence between adjacent chromophores, exciton transport is dominated by FRET, while at low temperatures, coherent transport dominates. A rough dividing point between coherent transport and the Förster mechanism is where either the energetic disorder or thermal energy ($k_B T$) is roughly equal to the dipole coupling strength.

Based on the dimer picture described in the previous section, we can derive the rate constant for FRET using Fermi's golden rule,

$$k_{ET} = \frac{2\pi V_{ab}^2 \rho}{\hbar},$$  (1.8)

where $\rho$ is the density of state, which is related to the spectra overlap between the donor and the acceptor. $V_{ab}$ describes the dipole interactions between the donor and the acceptor, which is proportional to $r^{-3}$ ($r$ is the inter-chromophore distance). If we assume that at the beginning, the excitation is at site $a$, denoted by $|\psi_a^*\psi_b\rangle$, after the energy transfer, the excitation is at site $b$, denoted by $|\psi_a\psi_b^*\rangle$, $V_{ab}^2$ thus can be written as,

$$V_{ab}^2 = \left| \left\langle \psi_a^*\psi_b \left| \frac{\kappa}{4\pi\epsilon_0} \frac{\mu_a\mu_b}{r^3} \right| \psi_a\psi_b^* \right\rangle \right|^2,$$  (1.9)

where $\epsilon_0$ is the electric constant, $\kappa$ is a geometry factor that depends on the relative orientation of the dipoles. By separating the dipole operators, the equation above can be transformed into the following functional form,

$$V_{ab}^2 = \frac{\kappa^2}{16\pi^2\epsilon_0^2} \frac{R_a R_b}{r^6},$$  (1.10)

where $R_a$ and $R_b$ are the transition dipole moments of the $a^* \to a$ and $b \to b^*$ transitions, respectively. The transition dipole moments can be converted to spectroscopically measurable properties, such as the radiative rate of the donor $\phi_D/\tau_D$ and the molar extinction coefficient of the acceptor $\varepsilon_A$, through the Einstein coefficients. After the conversion and taking the density of states into account, we obtained the final functional form of FRET,

$$k_{ET} = \frac{9ln10}{128\pi^5 n^4 N_A} \frac{\phi_D}{\tau_D} \frac{\kappa^2}{r^6} \int_0^\infty f_D(\lambda)\, \varepsilon_A(\lambda)\lambda^4 d\lambda,$$  (1.11)

where $n$ is the refractive index of the medium, $\phi_D$ and $\tau_D$ are the fluorescence quantum yield and lifetime of the donor in the absence of the acceptor. The last term is the spectral overlap integral of the donor and the acceptor.

### 1.2.3 Exciton Decay Pathways

When a chromophore is excited from the HOMO to the LUMO state, there is a range of excitation decay pathways, as illustrated by the Jablonski diagram (Fig. 1.2). The excitation quickly undergoes internal conversion to relax to the lowest vibrational level of the electronic excited state, as explained by Kasha's rule.[48] From there, the excitation can decay radiatively by emitting a photon or non-radiatively through internal conversion. The excitation can also undergo inter-system crossing to the triplet excited state or transfer its energy to another chromophore or a defect/quencher through the Förster or Dexter mechanism.[47, 49]

The optical transition probabilities between the states are governed by the Franck-Condon principle.[50] The Franck-Condon principle is based on the Born-Oppenheimer approximation. It assumes that the nuclear motion is very slow such that the nuclear position can be regarded as fixed during electronic transitions. As a result, the electronic wavefunction can be separated from the nuclear wavefunction. Since the electric dipole operator $\hat{\mu}$ only acts on the electronic component, the transition probability is given by,

$$k = \frac{2\pi}{\hbar} |\langle \psi_{el,f}|\hat{\mu}|\psi_{el,i}\rangle|^2 |\langle \psi_{vib,f}|\psi_{vib,i}\rangle|^2 \rho, \tag{1.12}$$

where the subscripts $i$ and $f$ indicate the initial and final states, respectively. $\rho$ is the density of the final state. The electronic part controls the overall oscillator strength of the
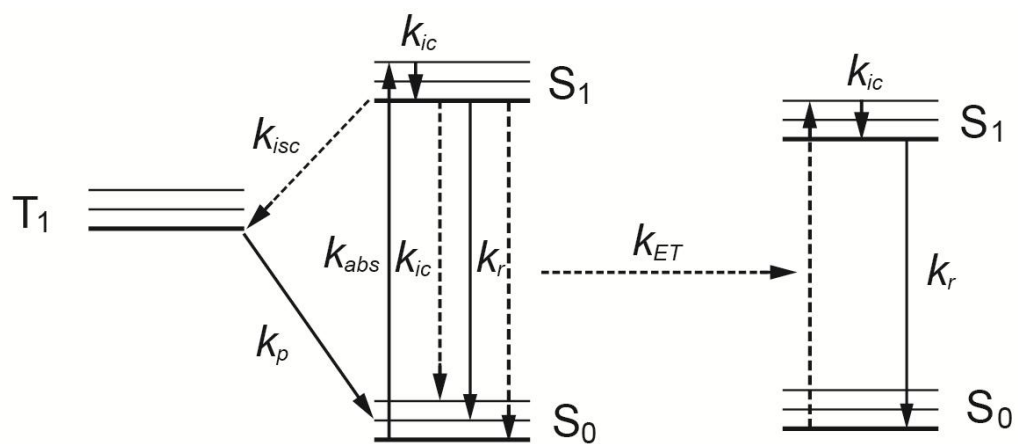
**Figure 1.2** Exciton decay pathways illustrated by the Jablonski diagram.

transition and the vibrational overlap integral determines the line shape of the spectrum, which is referred to as the Franck-Condon factor. The Franck-Condon factor is a sum over all the possible transition channels and is dominated by the channel for which the vibrational wavefunctions of the initial and the final states have the most overlap. If we consider the initial and the final states as two identical displaced harmonic oscillators, the vibrational overlap integrals of the 0-0 and 0-1 transitions are given by (note that the integrals for absorption and emission are the same. This together with the Boltzmann distribution and the Kasha's rule result in the mirror images of the absorption and emission spectra),

$$\langle \psi_{0,f} | \psi_{0,i} \rangle = e^{-\alpha(R_e - Q_e)^2/4}, \tag{1.13}$$

$$\langle \psi_{1,f} | \psi_{0,i} \rangle = \left(\frac{\alpha}{\pi}\right)^{1/2} (R_e - Q_e) e^{-\alpha(R_e - Q_e)^2/4}, \tag{1.14}$$

where $\alpha = \sqrt{mk}/\hbar$, $k$ is the force constant. As indicated by the equations, the vibrational overlap integrals are associated with the nuclear coordinate shift between the initial and the final states $R_e - Q_e$, which is often measured by the Huang-Rhys factor $S = \frac{k}{2\hbar\omega}(R_e - Q_e)^2$.[51] For a rigid molecule exhibiting small geometry change between the initial and final states, the Huang-Rhys factor is typically small and the transition is dominated by the 0-0 channel. Whereas for a flexible molecule, the Huang-Rhys factor is large that transitions to higher vibrational levels could be the dominate channel.

So far, we have only considered isolated chromophores. In conjugated polymer films, the electronic coupling between the chromophores results in the Dayvdov splitting of the excited states, as discussed in the dimer picture. Spano et al considered the electron-
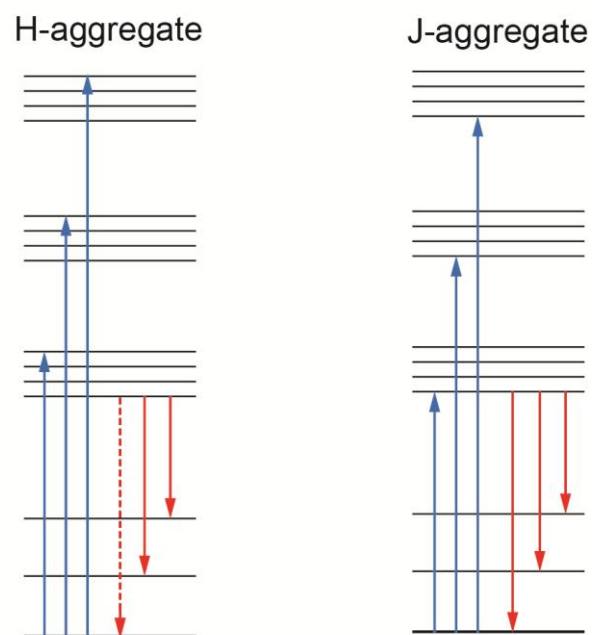
**Figure 1.3** Approximate energy diagrams of H- and J-aggregates, according to Spano's model. The solid blue and red arrows indicate allowed absorption and emission transitions, respectively. The dashed arrow indicates a forbidden transition.

vibrational coupling in the conjugated polymer aggregations and developed a model to explain the spectrum line shape of conjugated polymer films.[52, 53] As shown in Fig 1.3, due to the coupling, the vibrational levels of the excited state are split to form isolated bands. Similar to the dimer picture, for H-aggregate, the absorption occurs on the high energy edge of each vibronic band, while for J-aggregate, the absorption occurs on the low energy edges of the vibronic bands, as predicted by the overall transition dipole moments. Assuming a Huang-Rhys factor of 1, the model predicts that for both H- and J-aggregates, the 0-0 transition is the highest intensity peak in the absorption spectrum (the wavelength of the 0-0 transitions in the two cases are different). Due to fast internal conversion, emission occurs on the lowest energy excited state. For J-aggregate, radiative relaxations to all the vibrational levels of the electronic ground state are allowed. Whereas for H-aggregate, emission from the lowest energy excited state is forbidden due to a zero net transition dipole moment. However, when disorder and vibronic coupling are presented, the selection rule is relaxed. Side band emission becomes weakly allowed while the 0-0 emission is still forbidden. This leads to an interesting phenomenon that for J-aggregate, the 0-0 emission has the highest intensity whereas for H-aggregate, the 0-1 emission has the highest intensity, which has been used to identify H- and J-aggregates in P3HT films.[52]

### 1.2.4 Exciton Quenching Processes

Fluorescence quenching in conjugated polymers typically involves formation and energy transfer to nonfluorescent or weakly-fluorescent species. There are a variety of

aggregation species in conjugated polymers, including J- and H-aggregates as well as excimer and exciplex. As discussed in the previous section, due to relaxation to the lower excited state and its low overall transition dipole moment, H-aggregates typically exhibit low fluorescence quantum yields. It is worth noticing that J- and H-aggregates in conjugated polymers could both be originated from π-stacking conformations. The inter- and intra-chain coupling strength determines whether the optical property is J- or H-aggregation type. Pertubations from the environment could interrupt the weak Van der Waals force between the polymer chains and cause changes between the staggered conformation (J-type) and eclipsed conformation (H-type), as observed by John Grey et al in study of P3HT nanofibers.[35] Excimer and exciplex are formed by face-to-face stacking of identical (excimer) or chemically distinct (exciplex) π-conjugated chromophores. The difference between excimer/exciplex and H-aggregate is that excimer/exciplex exhibit bound excited-state and dissociated ground state, which results in broad, red-shifted emission spectra.[54, 55] Exciplex typically involves electron transfer between the donor and acceptor's excited states (Fig. 1.4). The transferred electron can relax to the donor's ground state or back transfer to the donor's excited state. As a result, formation of exciplex can lead to long-lived excited state and reduced fluorescence quantum yield.[55]

As discussed earlier, hole polarons are efficient fluorescence quenchers in conjugated polymers. In the early research of conjugated polymer thin film devices, the substantial quenching of film emission under electric field was attributed to the weakly bound electron-hole pairs (Wannier-Mott type excitons), as suggested by the SSH model.[56]
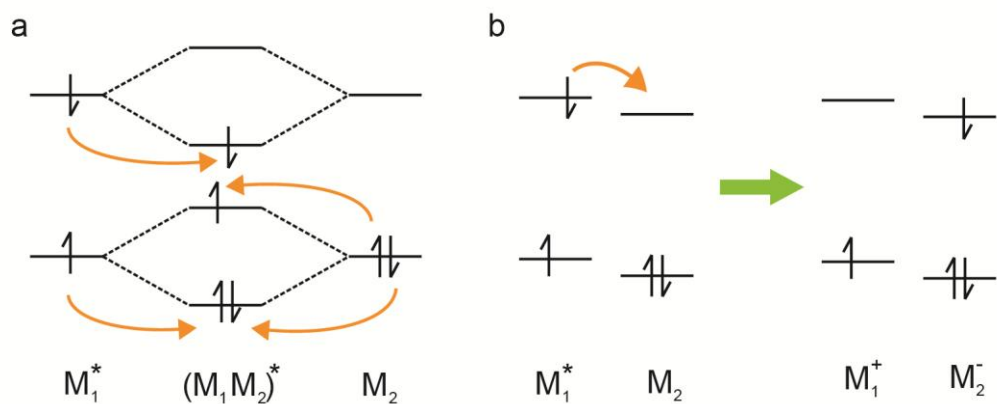
**Figure 1.4** Energy diagrams of excimer (left) and exciplex (right). Through the interactions between an excited molecule ($M_1^*$) and another molecule in the ground state ($M_2$), a neutral excited dimer or a charge-transfer complex can be formed.

However, later researches conducted by Heinz Bässler et al have shown that the Coulomb interaction between the electron-hole pairs in conjugated polymers is strong and the fluorescence quenching observed is due to injection of holes.[57] Hole polarons are essentially nonfluorescent. Due their red-shifted absorption spectra comparing to neutral polymers, energy transfer from excitons to hole polarons are highly efficient. As indicated by researches conducted by Paul Barbara et al, hole polarons are preferably generated at the bottom of a funnel shaped energy landscape.[32] As a result, the effect of quenching by hole polarons is amplified by exciton diffusion and energy cascade. In some cases, a single hole polaron can quench the fluorescence of a entire polymer chain. Polaron dynamics have great impact on single particle fluorescence of CPNs, resulting in a variety of phenomena, including fluorescence blinking, reversible fluorescence decay and fluorescence saturation.[12] These phenomena can be utilized for various imaging applications, which will be discussed in detail in later chapters.

## 1.3 Charge Carrier Dynamics in Conjugated Polymers

### 1.3.1 Charge Generation in Conjugated Polymers

The process of charge generation in conjugated polymers is of fundamental interest as it is directly related to the efficiency of conjugated polymer based photovoltaic devices. In addition, hole polaron is known to be efficient fluorescence quenchers in conjugated polymer systems. Generation and recombination dynamics of charge carriers have great impact on the performance of conjugated polymer based light-emitting devices and fluorescence tags. While conjugated polymers are often compared to inorganic

semiconductors, there is fundamental difference between the charge generation processes in the two systems. In inorganic crystals, due to the large dielectric constants, Coulomb force between electrons and holes is effectively shielded, which results in instantaneous photo-induced charge separation. While in organic semiconductors, the dielectric constants are typically small, the typical exciton binding energy is in the range of 0.5-1 eV. As a result, charge generation in conjugated polymers is either through injection/extraction of electrons/holes from electrodes or through oxidation/reduction reactions (i.e., electron transfer) between polymers and dopant molecules, for example, fullerene and its derivatives. Single molecule studies conducted by Paul Barbara and co-workers have provided insight about charge generation mechanism on isolated conjugated polymer chains. They concluded that through oxidation/reduction reactions between singlet oxygen and conjugated polymers, hole polarons are generated on the low energy emission sites on a conjugated polymer chain.[32] As a result, the fluorescence of the polymer chain is effectively quenched. Singlet oxygen is a meta-stable excited state of oxygen.[58] Under low pressure, singlet oxygen can have a lifetime of 2700 s. Single oxygen is typically generated by energy transfer from triplet excitons to the ground state oxygen and is very reactive toward organic molecules. The oxidation process of conjugated polymers is partially reversible. By accepting an electron from the environment or the doped radical scavenging species, the fluorescence of the polymer chain can be restored. However, over exposure to oxygen molecules and repeated generation of hole polarons eventually lead to irreversible photo-destruction of conjugated polymer chains.

In CPNs, the process of hole polaron generation is similar to the case of isolated conjugated polymer chains. The polaron generation is typically slow in absence of dopants, involving electron transfer to singlet oxygen or chemical defects. The hole polaron is stabilized by the geometric relaxation of the surrounding chromophores or through interaction with solvent molecules. As a result, under some conditions, the lifetime of hole polarons can be as long as 30 s in CPNs.[59] Due to the larger system dimensions, CPNs can have a larger polaron population comparing to isolated conjugated polymer chains. Typically, under moderate excitation intensities, the polaron population in CPNs ranges from 2-5 per particle, as determined from the levels of single particle fluorescence intensity fluctuations.[12] CPNs doped with fullerene derivative phenyl-C61-butyric acid methyl ester (PCBM) can establish a much larger polaron populations (10+ per particle) due to the efficient electron transfer from the conjugated polymers to the PCBM.[29] One of the interesting observations is that charge generation in PCBM doped CPNs occurs over a wide range of timescales, which likely indicates a high level of structural heterogeneity and disorder. At the polymer/PCBM interface, charge separation is almost instantaneous whereas in the regions far away from the interface, charge generation is much slower. It is likely that the slow fluorescence blinking observed (millisecond to second scale) for PCBM doped CPNs is mostly caused by hole polarons generated far away from the polymer/PCBM interface, or perhaps, in some cases, the hole polarons can escape and diffuse away from the interface, which results in the decreased polaron recombination rate and the increased steady-state hole polaron concentration.

**1.3.2 Charge Transport in Conjugated Polymers**

Understanding charge transport processes in organic semiconductors has been an ongoing challenge. Organic semiconductors are held together by weak van der Waals forces, which results in complex morphology at the nanoscale. Depending on ordering of the structure, there are various physical pictures that can apply to charge transport dynamics. In very pure molecular crystals or highly ordered polymer films, band conduction provides a good description of charge transport, especially at low temperatures.[56, 60] In contrast, when the coherence of adjacent sites is destroyed, either by disorder or inter- and intramolecular vibrations (at high temperature), charge transport occurs mainly through a hopping mechanism.[61, 62] The difficulty of obtaining a detailed picture of charge transport in disordered materials is due to the great dynamic heterogeneity present in the system and lack of tools for probing charge transport at single electron level. Traditional methods for probing charge transport in semiconductors are Time of flight (ToF) and current-voltage (I-V) analysis, which are ensemble measurements that average over large areas and many charge carriers.[63] In order to obtain the transport parameters of individual carriers, these methods are often combined with extensive modeling and Monte Carlo simulations. In this section, we will focus on the basic picture of charge transport. Advanced modeling of charge transport and examples of ToF studies can be found in the reviews written by Heinz Bässler. [64, 65]

For simplicity, let's consider the case of a single electron in an organic semiconductor matrix. Without considering the complex Coulomb interaction between multiple electrons, the Hamiltonian of the system can be written by the following expression,

$$\hat{H} = \hat{H}_{el} + \hat{H}_{ph} + \hat{H}_{el-el} + \hat{H}_{el-ph} + \hat{H}_{dis}, \tag{1.15}$$

where $\hat{H}_{el}$ is the electronic excitation term, $\hat{H}_{ph}$ is the vibrational excitation term, $\hat{H}_{el-el}$ describes the electronic coupling between the sites, $\hat{H}_{el-ph}$ is the electron-phonon coupling term, and $\hat{H}_{dis}$ is the static disorder term. $\hat{H}_{el}$ and $\hat{H}_{ph}$ are given by,

$$\hat{H}_{el} = \sum_n \varepsilon_n a_n^\dagger a_n, \tag{1.16}$$

$$\hat{H}_{ph} = \sum_\lambda \hbar\omega_\lambda \left( b_\lambda^\dagger b_\lambda + \frac{1}{2} \right), \tag{1.17}$$

where $a_n^\dagger$, $a_n$ are the creation and the annihilation operators of an electronic state of energy $\varepsilon_n$ at site n. $b_\lambda^\dagger$, $b_\lambda$ are the creation and the annihilation operators of an vibrational mode with energy spacing of $\hbar\omega_\lambda$. Without considering polaron effect and disorder, the electron transfer rate is determined by the inter-site electronic coupling, which is given by,

$$\hat{H}_{el-el} = \sum_{\substack{n,m \\ n \neq m}} J_{nm} a_n^\dagger a_m. \tag{1.18}$$

Coupling of the electronic excitation and the lattice vibration reduces the energy of the electron resident site and alters the electron transfer probability to the adjacent sites, which is referred to as polaron effect or dynamic disorder. This term is given by,

$$\hat{H}_{el-ph} = \sum_\lambda \sum_n g_{n\lambda}^2 \hbar\omega_\lambda a_n^\dagger a_n (b_\lambda^\dagger + b_\lambda)$$

$$+ \sum_\lambda \sum_{\substack{n,m \\ n \neq m}} f_{nm\lambda}^2 \hbar\omega_\lambda a_n^\dagger a_n (b_\lambda^\dagger + b_\lambda). \tag{1.19}$$

The first and second terms in the equation 1.19 correspond to the diagonal (intra-molecular) dynamic disorder and the off-diagonal (inter-molecular) dynamic disorder,

respectively. In the end, let's consider the effect of static disorder by adding variations to site energies and electronic coupling strengths,

$$\widehat{H}_{dis} = \sum_n \delta\varepsilon_n a_n^\dagger a_n + \sum_{\substack{n,m \\ n \neq m}} \delta J_{nm} a_n^\dagger a_m. \tag{1.20}$$

As shown above, there are multiple parameters that can affect charge transport in conjugated polymers. Fortunately, in many cases, charge transport is dominated by a few terms in the Hamiltonian and the complexity of the model can be greatly reduced, which will be discussed in the following sections.

## 1.3.2.1 Band Conduction in Conjugated Polymers

In a perfectly ordered lattice that $\widehat{H}_{el-ph}$ and $\widehat{H}_{dis}$ are negligible compared to $\widehat{H}_{el-el}$, band transport is the dominate charge transport mechanism, i.e., charge carriers are delocalized and transport as propagating waves. In a molecular picture, band structure is formed by splitting of the molecular orbitals caused by electronic coupling between the adjacent sites. The band structure of conjugated polymers was first investigated by Su, Schrieffer and Heeger.[56] They considered a theoretical system of one-dimensional, infinite chain of polyacetylene , which is later referred to as the SSH approach. Formation of bands is expected for such a system with periodic potential. To understand this better, we shall consider the simple case of one-dimensional Dirac comb. The potential of the system is given by,

$$\widehat{V}(x) = \alpha \sum_j \delta(x - ja), \tag{1.21}$$

which is a periodic delta function with spacing of $a$. According to the Bloch's theorem,[66]

the eigenfunction of systems with periodic potential obeys the following rule,

$$\psi(x + a) = e^{iKa}\psi(x). \tag{1.22}$$

Therefore, we only need to solve the Schrödinger equation within a single cell and use

the equation above to obtain solutions elsewhere. In the region $0 < x < a$, the solution is

given by,

$$\psi(x) = A sin\left(\frac{\sqrt{2mE}}{\hbar}x\right) + B cos\left(\frac{\sqrt{2mE}}{\hbar}x\right), (0 < x < a) \tag{1.23}$$

Apply the equation 1.22, we obtain the following expression,

$$\psi(x) = e^{-iKa}\left[A sin\left(\frac{\sqrt{2mE}}{\hbar}x\right) + B cos\left(\frac{\sqrt{2mE}}{\hbar}x\right)\right], (-a < x < 0) \tag{1.24}$$

By using the boundary condition (continuity) to solve A and B, we obtain the following

equation,

$$cos(Ka) = cos\left(\frac{\sqrt{2mE}}{\hbar}a\right) + \frac{\alpha}{2E}sin\left(\frac{\sqrt{2mE}}{\hbar}a\right). \tag{1.25}$$

The equation above determines the possible energy $E$ of the system. The left side of the

equation is in range [-1, 1]. Therefore, there is a continuous range of energies that are

forbidden, which correspond to band gaps. The values of the allowed energies depend on

the wave vector $K$. In a highly ordered system, $K$ can be regarded as continuum, which

leads to densely-packed states and formation of bands. In the more complicated case of a

conjugated polymer chain, due to alternating single and double bonds, the potential

energy is dimerized, which causes Peierl's distortion.[56] In addition, Su, Schrieffer and

Heeger considered the effect of lattice mismatch and formation of solitons. They derived energy eigenstates for the dimerized potential in the following expression,

$$E(K) = \pm\sqrt{(2t_0 \cos Ka)^2 + (2\alpha\mu_0 \sin Ka)^2}, \qquad (1.26)$$

where $K$ is the wave vector, $a$ is the length of a unit cell. The energy gap between the conduction and valence band is given by $4\alpha\mu_0$, depending on the displacement of dimerized chain $\mu_0$ and the electron-phonon coupling strength $\alpha$, as shown in Fig. 1.5. One of the key assumptions in the SSH model is that the interaction between electrons and holes is weak in conjugated polymers, which corresponds to the Wannier-Mott type excitons.[67, 68] The binding energy of the electron-hole pair is considered to be on the order of the thermal energy (Wannier-Mott excitons essentially do not exist at room temperature). As a result, optical excitation results in instantaneous separation of charges. While this assumption works for inorganic semiconductors, it is not realistic considering the small dielectric constants of conjugated polymers. As we discussed earlier, a more appropriate physical picture is the Frenkel exciton, which had been used to describe excitations in molecular crystals for a long time,[69] before the development of the SSH model. In addition, the band gap in the SSH model is directly related to the Peierl's distortion caused by the bond alternation. According to the model, poly(silylene) should exhibit a minimal band gap and metallic properties. However, such phenomenon hasn't been experimentally observed.[70] While there are discrepancies between the model and experimental observations, the SSH approach is still considered as one of the most important early attempts to understand the electro-optical properties of conjugated polymers and has great influence on later research in this field.
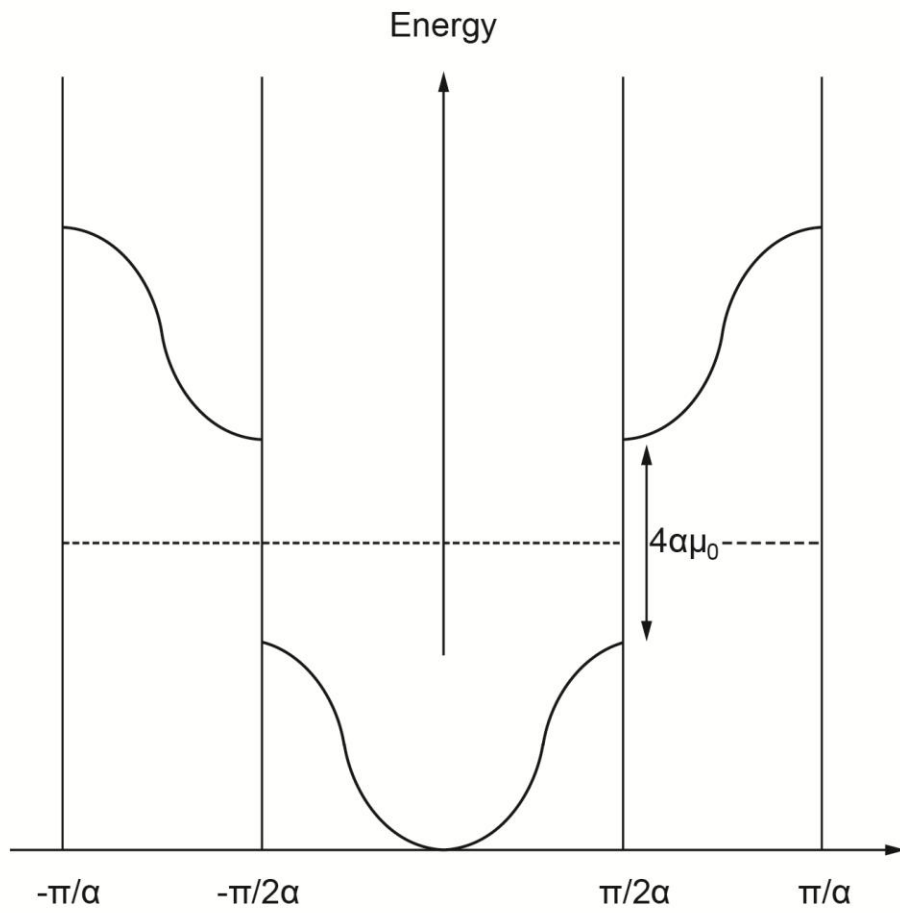
**Figure 1.5** The band structure of a conjugated polymer chain with dimerized potential, obtained from the SSH model.

### 1.3.2.2 Hopping Conduction in Conjugated Polymers

In amorphous polymers, ordering is only remained for a few repeat units. As a result, the band transport picture described above no longer applies. Due to the geometric relaxation caused by charge carrier ($H_{el-ph}$) and variations in inter-site distance/site energy ($H_{dis}$), charge carriers are localized and move by uncorrelated, phonon-assisted hopping. The theory of polaron transport was pioneered by Mott, Holstein and Emin.[61, 62, 71] The transport equation obtained is equivalent to the Marcus theory of electron transfer. The Marcus theory was developed by Rudolph Marcus in 1956 to describe electron transfer between weakly coupled electron donor-acceptor pairs, which can be represented as two displaced harmonic oscillators.[72] One of the important results of the Marcus theory is that the electron transfer rate doesn't increase monotonically with the decrease of $\Delta G^0$.[73] As shown in Fig. 1.6, the electron transfer process is most efficient when the reorganization energy $\lambda$ associated with polaron effect is compensated by the overall free energy of the reaction. As predicted by the Marcus theory, due to the effect of reorganization energy, the electron transfer rate would slow down at very negative $\Delta G^0$, which is referred to as the inverted region. After the experimental observation of the inverted region by John Miller et al (first observation in 1984, almost 30 years after the theory was proposed),[74] Rudolph Marcus was awarded Nobel Prize in chemistry in 1992.

Historically, the Marcus equation was developed based on the Franck-Condon principle. It assumes that the electron transfer is very fast that the nuclear coordinates of the donor and the acceptor remain unchanged during the process. The weak electronic
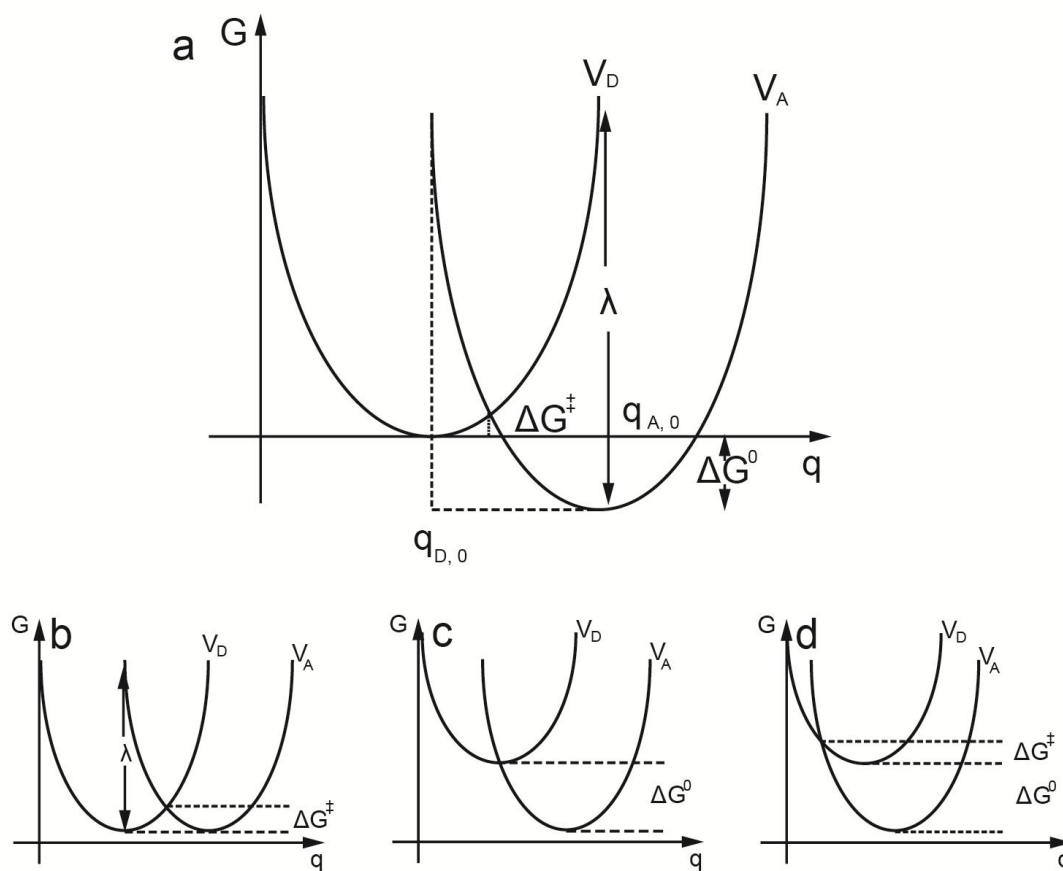
**Figure 1.6** (a) The potential energy curves of two displaced harmonic oscillators. (b) The potential energy curves when $\Delta G^0 = 0$. The activation energy required is $\lambda/4$. (c) The potential energy curves when $\Delta G^0 = -\lambda$, which corresponds to the most efficient electron transfer. (d) The potential energy curves when $\Delta G^0 < -\lambda$., which corresponds to the inverted region.

coupling between the donor and the acceptor is introduced as a perturbation. According to Fermi's golden rule, the electron transfer rate can be written as,

$$k_{ET} = \frac{2\pi}{\hbar} |\langle \psi_{el,D}|H'|\psi_{el,A}\rangle|^2 |\langle \psi_{vib,D}|\psi_{vib,A}\rangle|^2 \rho(E_A). \qquad (1.27)$$

The first part of the equation contains the matrix element of electronic mixing between the donor and the acceptor, which dictates the electron transfer rate in the absence of a barrier. The second part consists of a Franck-Condon factor and the classical density of state. For an electron to be transferred from the lowest vibrational state of the donor to the acceptor, the rate is given by,

$$k_{ET} = \frac{2\pi}{\hbar} H_{DA}^2 (FC)(\frac{1}{4\pi\lambda k_B T})^{\frac{1}{2}}, \qquad (1.28)$$

$$FC = \sum_{v'} \frac{S^{v'} e^{-S}}{v'!} e^{\frac{-(\lambda + v'\hbar\omega + \Delta G^0)^2}{4\lambda k_B T}}, \qquad (1.29)$$

where $S$ is the Huang-Rhys factor related to the displacement of the two harmonic oscillators, $v'$ is the vibrational level of the electron on the acceptor after the transfer. As indicated by the Franck-Condon factor, the transfer probability is a sum over all the possible reaction channels and is dominated by the channels for which $\Delta G^0 \approx \lambda + v'\hbar\omega$, which indicates that the electron transfer is mostly likely to occur when the sum of the reorganization energy $\lambda$ and the vibrational energy of the final state $v'\hbar\omega$ are matched by the overall free energy of the reaction $\Delta G^0$. For a highly disordered system that the polaron binding energy is small comparing to the energetic disorder, a simplified version of the Marcus equation can be used, which is referred to as the Miller-Abrahams equation:

$$k_{ET} = v_0 e^{-2\gamma r_{DA}} e^{-\frac{\Delta E_{DA}}{kT}}, \qquad\qquad (1.30)$$

where $k_{ET}$ is the hopping rate, $r_{DA}$ is the hopping distance, $\Delta E_{DA}$ is the energy barrier height, $v_0$ is the attempting rate.[75] The Miller-Abrahams equation neglects polaron effect in that the Franck-Condon factor in the Marcus equation is simplified to an Arrhenius term. The exponential term of distance dependence in front of the Arrhenius term is a result of the electronic overlap integral $H_{DA}^2$ in the Marcus equation.

Overall, charge transport in conjugated polymers is a complex process dictated by multiple factors, such as chain packing, structural/chemical defects, static/dynamic disorder, etc. In a heterogeneous polymer film, charge carriers can adopt different transport mechanisms depending on the local structure. Under a electric field, charge carriers are transported across the material via the fastest paths available, through a combination of band and hopping transport, which can be described by the percolation theory.[76] The complexity of the dynamics causes difficulty for ensemble measurements in that the equations of single carrier transport can only be inferred indirectly through extensive modeling and simulation. In later chapters, we will demonstrate that, using single particle localization method, the nanoscale motion of a single charge carrier can be directly resolved, and the distances and the frequencies of carrier hopping between various traps, *i.e.*, the key parameters of the single carrier equations of motion, can be determined.

## 1.4 Superresolution Microscopy

In the conventional light microscopy, due to diffraction, light emitted from a point source is observed as a point-spread-function (PSF). The width of the PSF is often referred to as the diffraction limit, which is given by $d = \frac{\lambda}{2NA}$, related to the excitation wavelength λ and the numerical aperture of the microscope objective *NA*.[77] Typically, imaging with visible light excitation using oil immersion microscope objective (*NA*, ~1.25) results in a resolution of 200-250 nm, which is larger than the length scales of many biomolecular assemblies and cellular structures. For example, the width of the microtubule is typically less than 50 nm, an the diameter of clathrin coated vesicles typically ranges from 50-100 nm. Driven by the interest of imaging cellular structures beyond the diffraction limit, multiple superresolution imaging techniques have been developed in the last 30 years.

**1.4.1 Near-Field Scanning Optical Microscopy**

One of the strategies to overcome the diffraction limit involves focusing through a nanoscale aperture that has a smaller diameter than the excitation wavelength. The aperture is placed very close (less than a few nm) to the specimen and the image is obtained through a point-to-point scanning of the sample, which is referred to as near-field scanning optical microscopy (NSOM).[78] The concept of NSOM was proposed as early as 1928, by Synge [79]. However, due to the technological challenges in the aperture fabrication and positioning (through shear-force or tapping feedback), imaging using NSOM with visible light excitation had not been achieved until 1980s. One of the important contributions in development of NSOM was from Eric Betzig at Bell

laboratory,[78] who introduced a single-mode optical fiber as the NSOM probe. Unlike other superresolution techniques, NSOM doesn't strictly rely on the photophysical properties of the fluorophores. Therefore, NSOM is regarded as a true superresolution method. However, near-field scanning typically results in very shallow depth of field and long imaging time for large samples.

**1.4.2 Deterministic Functional Techniques**

Stimulated emission depletion (STED) and ground state depletion (GSD) microscopy are two closely-related superresolution techniques that were both proposed and realized by Stefan Hell.[80-82] The basic idea behind these two methods is to use a Gaussian shaped laser beam to excite fluorophores and use a donut shaped depletion laser beam to send most of the fluorophores into dark states. By combining these two laser profiles, only the fluorophores within the center of the Gaussian shaped excitation beam are able to emit, which allows sub-diffraction limit imaging. The difference between the two methods is that, in STED, the fluorophores in the excited state are sent back to the ground state through stimulated emission, whereas in GSD, the fluorophores in the excited state are sent to the long-lived triplet state through intersystem crossing. The effective resolution of STED and GSD is given by,

$$d = \frac{\lambda}{2NA\sqrt{1 + I_D^{max}/I_s}},$$

(1.31)

where $\lambda$ is the excitation wavelength, $NA$ is the numerical aperture of the microscope objective, $I_D^{max}$ is the maximum intensity of the depletion beam and $I_s$ is the saturation

intensity for the fluorophore. Typically, dyes used for GSD microscopy have high saturation intensities (~10 kW/cm$^2$). According to the equation 1.31, in order to achieve 10 nm spatial resolution,[82 84 84 84] the depletion beam should have peak intensity around 1000 kW/cm$^2$, which could cause damage to the sample. Development of fluorescence tags with low saturation intensity is desired for further development of these techniques.

### 1.4.3 Stochastic Reconstruction Techniques

Fluorescence photo-activation localization microscopy (PALM) and stochastic optical reconstruction microscopy (STORM) are another two closely-related superresolution techniques published separately by Eric Betzig and Xiaowei Zhuang.[83, 84] Both techniques rely on the single molecule localization method. As derived by Thompson et al,[85] the precise location of a fluorophore can be determined by fitting a 2D Gaussian to the PSF. The localization precision is given by $\sigma = s/\sqrt{N}$, where $s$ is the standard deviation of the PSF and $N$ is the number of detected photons used in the fitting. Experimentally, prior to the publication of PALM and STORM, fluorescence imaging with one-nanometer accuracy (FIONA) has been demonstrated for molecular rotor Myosin V.[86] However, fluorescence imaging of densely labeled system remained challenging due to overlapping of PSFs. To avoid this problem, PALM and STORM utilized the photoactivation behavior of the green fluorescence protein (GFP) and the photoswitching behavior of the paired cyanine dyes, respectively.[83, 84] In PALM, GFPs at random locations are subsequently photoactivated, imaged and photobleached. In the
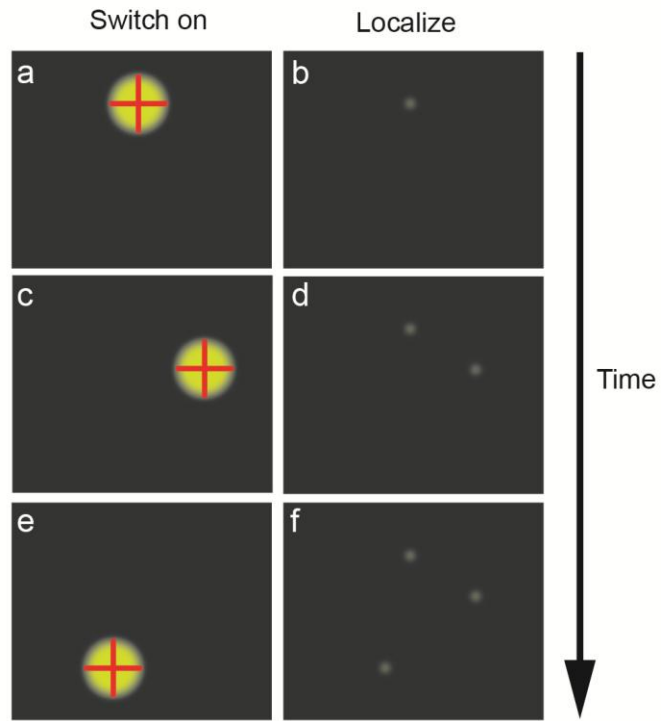
**Figure 1.7** Illustration of the working principle of STORM. Fluorophores at different locations are switched on randomly over time (left), which allows the position of the fluorophores to be determined with high precision (right).

next cycle, another set of GFPs will be localized using the same principle. In the end, a sub-diffraction limit image is constructed from the fluorophore locations determined from each cycle. The principle of STORM is similar (Fig. 1.7). The only difference is that by the end of a cycle, the dyes are switched off by a red laser rather than photobleached. [84] The photoswitchable dyes can often be switched on and off for tens to hundreds of cycles, which is an advantage of STORM. However, PALM is better suited for in vivo studies, as GFPs can be genetically encoded in a variety of cells/bacteria and selectively expressed. Both PALM and STORM are wide-field superresolution techniques, which are much more efficient for imaging of large samples, compared to sample scanning superresolution methods such as NSOM, STED or GSD.

### 1.4.4 Superresolution Optical Fluctuation Imaging

Both PALM and STORM have strict requirements on the photophysical properties of the fluorophores (photoactivation, photoswitching). In certain wavelength ranges, there are very limited choices of fluorophores that satisfy those requirements. Superresolution optical fluctuation imaging (SOFI) is an imaging method that greatly expands the choice of fluorophores for superresolution imaging. The main idea behind SOFI is that no two fluorophore show intensity fluctuation in the same way, i.e., blinking is a stochastic process. Therefore, by running correlation analysis between pixels, we can tell whether the photons detected in a certain pixel comes from a single fluorophore or multiple fluorophores with overlapping PSFs.[87] In principle, any

fluorophore that shows fluorescence intensity fluctuations can be used in SOFI. However, complex fluctuations with small amplitudes can cause problems in correlation analysis and result in long imaging as well as processing time. SOFI works well for blinking fluorophores that can't completely turn off. However, due to the nature of this method, the spatial resolution of SOFI can't surpass the pixel size of the image, in contrast to FIONA, PALM and STORM, which typically exhibit sub pixel resolution.

# CHAPTER TWO

# EXPERIMENTAL METHODS

## 2.1 Materials

Poly[(9,9-dioctylfluorenyl-2,7-diyl)-*co*-(1,4-benzo-{2,1′,3}-thiadiazole)] (PFBT, MW 10,000, polydispersity 1.7) was purchased from ADS Dyes, Inc. (Quebec, Canada). Tetrahydrofuran (THF, HPLC grade, 99.9%), phenyl-C61-butyric acid methyl ester (PCBM, 99.5%) and (3-Aminopropyl) trimethoxysilane (APS, 97%) were purchased from Sigma-Aldrich (Milwaukee, WI). All chemicals were used as received without further purification.

## 2.2 Preparation of CPNs

CPNs were prepared by a nano-precipitation method described previously.[10, 88] A stock solution of conjugated polymers in THF (inhibitor-free HPLC grade) was prepared at a concentration of 1000 ppm. (THF solvent tends to form peroxide over time and cause oxidation of conjugated polymers. Therefore, THF was tested with potassium iodide starch test papers before preparation.). The solution was stirred for 1 hour to allow conjugated polymers to dissolve and filtered through a 0.45 μm membrane filter (Millipore). The stock solution was stored in a fridge at 5 $^\circ$C (typically, new stock solutions were prepared every month). To prepare CPNs, the stock solution was diluted to 20 ppm. Under mild sonication, 2 ml of the 20 ppm conjugated polymer THF solution was rapidly mixed with 8 ml of water. The mixture solution was then placed in a vacuum oven at 40 $^\circ$C for 6 hrs to remove THF (Due to formation of azeotrope, the boiling point

of THF/water mixture is lower than the boiling points of both THF and water. Under partial vacuum, the sample should only be heated mildly to prevent bumping of the sample.). In the end, the sample was filtered through a 100 nm PVDF membrane filter (Millipore) to remove aggregates. Typically, less than 10% of the polymer was removed by the filtration, as determined by UV-Vis absorption spectroscopy, indicating that most of the polymers formed nanoparticles. The resulting suspension was clear and stable for weeks without aggregation. The formation of CPNs is governed by hydrophobic interaction, interfacial tension as well as surface free energy. The size of the CPNs can be controlled by multiple steps in the preparation procedure. Rapid mixing of THF and water results in a sudden decrease in solvent quality and favors small particle formation. In contrast, large aggregates are typically observed when conjugated polymer THF solution is added drop-by-drop into water. In addition, increase of the precursor concentration typically results in larger particle sizes and larger fraction of polymer loss during the filtration due to aggregation.

Similar procedures can be employed to prepare doped CPNs. To prepare PCBM doped PFBT nanoparticles, conjugated polymer PFBT and fullerene derivative PCBM were dissolved in THF and diluted to 20 ppm. The solutions of PFBT and PCBM were mixed in various ratios to form precursors of varying dopant percentages (5%, 10%, 20%, 40%). 2 mL of the precursor solution was rapidly injected into 8 mL of water under mild sonication. Then the THF solvent was removed by partial vacuum evaporation. After evaporation, the sample was filtered through a 100 nm membrane filter (Millipore) to remove aggregates.

## 2.3 Characterization Methods

A variety of techniques were employed to characterize CPNs. Atomic force microscopy (AFM) and dynamic light scattering (DLS) were used to determine the size distribution of CPNs. Phase analysis light scattering (PALS) was used to determine the zeta potential of CPNs. Steady-state absorption and emission properties of CPNs were characterized by UV-Vis and fluorescence spectroscopy, respectively.

## 2.3.1 Atomic Force Microscopy (AFM)

AFM is a type of scanning probe microscopy, which was originally developed from scanning tunneling microscopy (STM) to characterize samples with low conductivity. AFM involves scanning through the surface of a sample using a cantilever with a sharp tip. The tip radius typically ranges from 5-20 nm. When the tip is brought into close range with the sample, mechanical or Van der Waals force between the tip and the sample surface results in deflection of the cantilever, which is monitored by an optical level (Fig. 2.1 a). Depending on the properties of the sample, a variety of scanning mode can be used in AFM, including contact mode, non-contact mode and tapping mode.

The contact mode is also called static mode, which involves bringing the tip into direct contact with the sample (Fig. 2.1 b). To obtain the topology of the sample, the cantilever deflection is kept constant by raising or lowering the tip during the scan. Typically, cantilevers with low spring constant are used in the contact mode to increase the sensitivity and keep the interaction force low.[89] The contact mode suits for hard samples

39

with spring constants larger than the spring constant of the cantilever.[90] The excessive tracking force applied from the tip to the sample in the contact mode is problematic for scanning of soft materials. In addition, caused by liquid meniscus layer or trapped charges on the sample surface, the attractive force can cause the tip to "snap-in" the surface during the scan and cause damage to the sample.[90]

To overcome the problems mentioned above, dynamic scanning modes were developed. One of the dynamic scanning modes is called non-contact mode. In the non-contact mode, the cantilever oscillates at its resonance frequency. When the tip is brought into close range with the sample, Van der Waals force dampens the oscillation of the cantilever. During the scan, the oscillation frequency or amplitude of the cantilever is kept constant by adjusting the tip-to-sample distance (Fig. 2.1 c). In the non-contact mode, the tip doesn't directly touch the sample, thus has advantages in scanning of soft materials. However, the Van der Waals forces are much weaker than the mechanical force used in the contact mode. As a result, obtaining the highest resolution with the non-contact mode often requires measuring the Van der Waals gradients that only extend a few nanometers above the sample surface.[91] Trapping of the tip could still occur, if there is thick fluid layer on the sample surface.

Another dynamic scanning mode is called tapping mode or intermittent contact mode. Similar to the non-contact mode, the cantilever in the tapping mode also oscillates at or near its resonance frequency. Once the tip is brought into periodic contacts with the sample surface (Fig. 2.1 b), the cantilever oscillation is dampened due to energy loss caused by the tip tapping the surface. The damping amplitude is used to identify and
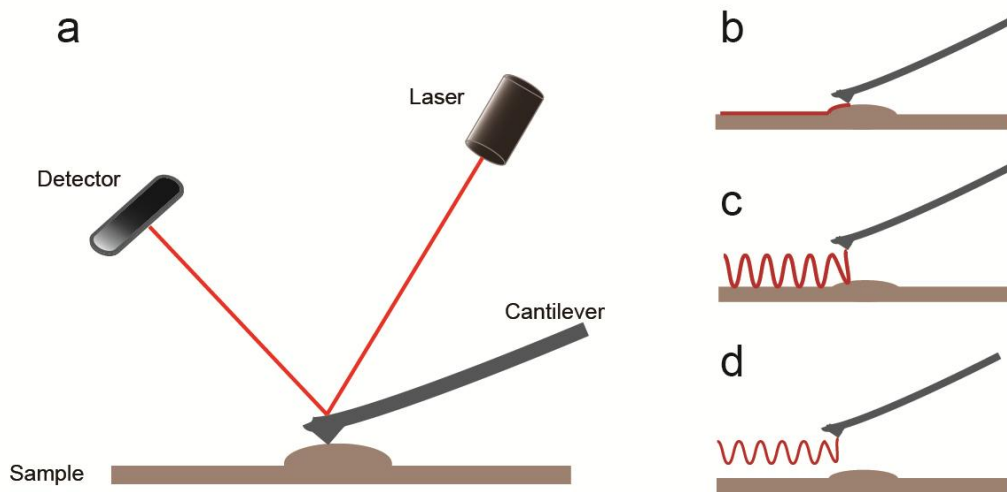
**Figure 2.1** (a) Illustration of AFM operation and comparison between various scanning modes: (b) contact mode, (c) tapping mode, (d) non-contact mode.

measure surface features. The tapping mode combines the advantages of the contact and the non-contact modes. Through oscillating the cantilever at high frequency (50k-500k Hz) and large amplitude (~100 nm), the tapping mode effectively overcomes the tip-sample adhesion forces without sacrificing the resolution, which makes this method ideal for scanning of soft materials.[91]

The size distribution of CPNs was measured from an Ambios Q250 multimode AFM in tapping mode. To prepare the AFM sample, a clean coverslip was functionalized with 70 μL of freshly prepared $5\times10^{-4}$ M APS in anhydrous ethanol. The functionalized coverslip was submerged under diluted CPNs suspension for 40 min. The coverslip was then rinsed with DI water and allowed to dry in a vacuum oven. Typical parameters employed for the AFM scans were a scan area of 5 μm, 500 lines/scan, and a scan rate of 0.5 Hz. There are tradeoffs between image accuracy (in terms of resolution and artifacts), scan speed, and tip-sample forces. The force feedback parameters and scan speed are adjusted to reduce tip trailing or streaking artifacts (typically observed as an asymmetric particle shape due to slow return of the tip to the surface after contact with a particle) to acceptable levels while avoiding excessive tip force that could damage the sample or the tip. The apparent topographic shape of individual particles is analyzed to check for tip damage. Occasionally, multiple scans of the same area are performed to check for scan-induced damage, as evidenced by progressive deterioration of the image in a series of scans. The piezoelectric scanner is calibrated periodically in the XY direction by AFM imaging of standard gratings, while the Z direction calibration is tested by imaging of standard polystyrene spheres. The AFM image was analyzed using custom Matlab

scripts. The diameters of CPNs were determined by the peak z-heights of each nanoparticle in the image. Dozens of CPNs were analyzed to determine the distribution of the particle sizes. While AFM is often not the primary method of choice for particle sizing (there are several likely sources of systematic error and artifacts, and additional time and expertise are required), it can be valuable in that it provides particle size and morphology information on a particle-by-particle basis, and the overall shape of the resulting size distributions is arguably more reliable than that of bulk techniques such as DLS (discussed below) since the determination of the distribution for such techniques involves an inversion problem which may not have a unique solution.

**2.3.2 Dynamic Light Scattering (DLS)**

DLS, also known as photon correlation spectroscopy, is a method for determining particle size distribution in solution. DLS measurement involves illuminating the sample with a laser. The scattered light from different particles in solution can interfere constructively (in-phase) or destructively (out-of-phase) and results in the speckle pattern. As particles undergo Brownian motions in solution, the intensity of the spots on the speckle pattern will fluctuate overtime due to changes in the distances between particles. The intensity fluctuations thus contain the time scale of the particle movements and can be used to determine the translational diffusion coefficients of the particles through autocorrelation analysis. Applying Stokes-Einstein equation, the hydrodynamic diameters of the particles can be calculated from the translational diffusion coefficients. Since the diffusion coefficient is also temperature dependent, DLS measurement is

typically performed under isothermal environment. In addition, at high particle concentrations, multiple scattering and viscosity effect occur, which could distort size distributions obtained from DLS measurement. Therefore, DLS is typically performed with diluted samples (sometimes involves a series of dilutions and extrapolating the result to the limit of zero concentration). When the particle size is small compare to the wavelength of the laser ($< \lambda/10$), the scattering process is isotropic, known as Rayleigh scattering.[92] However, when the particle size is comparable to the wavelength of the laser, the scattering intensity shows strong angle dependence, known as Mie scattering.[92] As a result, at certain angles, the scattering intensity of some particles will completely overwhelm the signal from the others. In addition, the scattering angle also controls the decay rates $\Gamma$ in the autocorrelation function ($\Gamma = q^2 D$, where $D$ is the translational diffusion coefficient, $q$ is the wave vector, depending on the scattering angle), thus could affect data analysis. Therefore, for highly dispersed samples (especially with large particles), it is necessary to perform DLS at multiple angles in order to obtain complete information about the particle size distribution. Highly dispersed particle size distribution also results in a broad range of decay time scales in the autocorrelation function and complicates the analysis. For a relative simple size distribution (a Gaussian shaped distribution), the cumulant method is typically used, which involves fitting a polynomial of third degree to the logarithm of the autocorrelation function.[93] The width (STD) of the particle size distribution is given by the second order cumulant of the fitted polynomial function. For a multimodal size distribution with clear separations between the species as well as for the case of narrow to moderately broad size distributions, the nonnegative
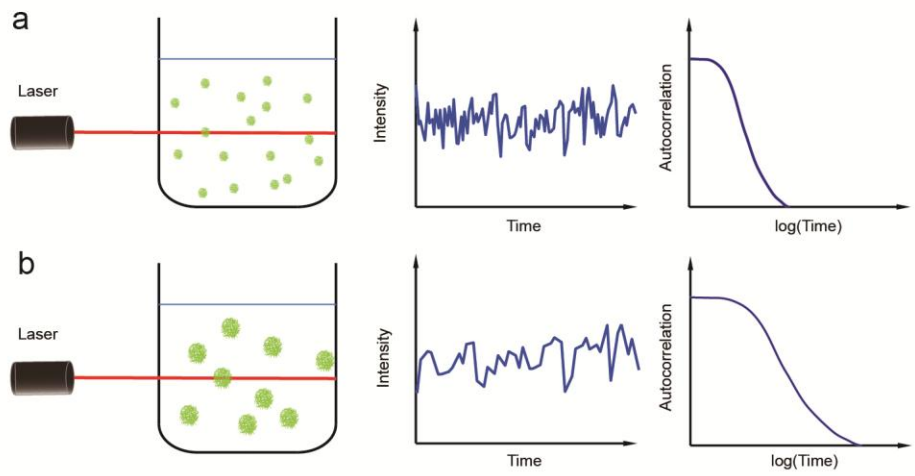
**Figure 2.2** (a) Scattering intensity fluctuations caused by Brownian motions of small particles and the corresponding autocorrelation function. (b) Scattering intensity fluctuations caused by Brownian motions of large particles and the corresponding autocorrelation function.

constrained least squares method (NNLS) and Laplace transform based methods, such as CONTIN, are typically used. [92]

DLS measurements of CPNs were performed using a Nanobrook Omni (Brookhaven Instruments Corporation, NY) with BIC Particle Solutions Software (V 3.1). The CPN suspensions were diluted to a peak absorbance of ~0.1. Typical conditions employed for the DLS measurements were 25 ℃, count rate of 500 kcounts/s, scattering angle of 90 °, and acquisition time of 180 seconds. Polystyrene spheres (Thermo Fisher, 24 nm) were used as a size standard. Typically, CPNs suspension consists of mostly small nanoparticles with small populations of larger aggregates (>100 nm). The NNLS method provided reliable fitting results of the particle size distributions, which were highly consistent with the results from AFM measurements.

### 2.3.3 Phase Analysis Light Scattering (PALS)

Zeta potential is the electric potential difference between the stationary layer of ions/solvent molecules attached to the particle surface and the dispersion medium. The zeta potential determines the repulsion force between the particles, thus can be used to predict the stability of the colloid. PALS is a DLS based technique that is commonly used in zeta potential measurement. PALS involves applying an oscillating electric field to the dispersion medium. Due to surface charges, particles will diffuse according to the electric field. The particle movements result in small shifts in the frequency and the phase of the scattered light, which can be used to measure the particles velocity under electric field and estimate the zeta potential of the particles. PALS measurements of CPNs were

46

performed using a Nanobrook Omni (Brookhaven Instruments Corporation, NY) with BIC Particle Solutions Software (V 3.1). The CPNs suspensions were diluted to a peak absorbance of ~0.1. Typical conditions employed for the measurements were 25 ℃, count rate of 500 kcounts/s, scattering angle of 15°, and 30 cycles. Typically, CPNs exhibit zeta potentials ranging from -30 mV to -40 mV, which is consistent with the moderate to good colloidal stability of CPNs.

## 2.3.4 Steady-State Absorption and Fluorescence Spectroscopy

The UV−vis absorption spectra were collected using a Shimadzu UV-2101 PC scanning spectrophotometer with 1 cm quartz cuvettes. To determine the molar extinction coefficients/absorption cross-section of conjugated polymers, conjugated polymers were dissolved in THF and diluted to a peak absorbance of ~0.1. According to the Beer's Law, the molar extinction coefficient is given by $\varepsilon = A/lc$, where $A$ is the absorbance of the sample, $l$ is the sample path length (1 cm) and $c$ is the molar concentration of conjugated polymer. If we replace the molar concentration $c$ in the Beer's law with molecule density $N$ (molecules/cm$^3$), we can calculate the absorption cross-section $\sigma$ using equation $\sigma = 2.303 * A/lN$. The extinction coefficient/absorption cross-section of CPNs were calculated by the molar extinction coefficients/ absorption cross-section of the corresponding conjugated polymer times the number of polymer molecules per nanoparticle $N_{np}$. $N_{np}$ is determined from the mean nanoparticle volume (calculated from nanoparticle diameters determined by AFM) and the polymer molecular weight (assuming a polymer density of ~1 g/cm$^3$).

The fluorescence emission spectra of CPNs were measured with a commercial fluorometer (Quantamaster, PTI, Inc.). The fluorometer uses a xenon arc lamp as the excitation source and a photomultiplier tube (PMT, model 814) as the detector. The slit widths are set to 0.5 mm to prevent saturation of the PMT. The CPN suspensions were diluted to a peak absorbance of ~0.05 to prevent inner-filter effect. To measure the fluorescence quantum yield of CPNs, a standard fluorescent dye with absorption and emission maxima similar to the corresponding CPNs under study was used. A common excitation wavelength was chosen between the absorption maxima of the CPNs and the standard. All the solutions were diluted to an absorbance of ~0.05 at the common wavelength. The fluorescence quantum yield of CPNs was calculated using the following expression,

$$\phi_f(x) = \frac{A_s F_x n_x^2}{A_x F_s n_s^2} \phi_f(s), \tag{2.1}$$

where subscripts $s$ and $x$ denote the standard and the CPNs, respectively. $\phi_f$ is the fluorescence quantum yield, $A$ is the absorbance at the excitation wavelength, $F$ is the integrated intensity, and $n$ is the refractive index of the solvent.

For dye doped CPNs, the Förster radius between the donor and the acceptor is calculated using the following equation,

$$R_0{}^6 = \frac{9000 \ln(10)\,\phi_D \kappa^2}{128\pi^5 N_A n^4} \int_0^\infty f_D(\lambda)\,\varepsilon_A(\lambda)\lambda^4 d\lambda, \tag{2.2}$$

where $\phi_D$ is the fluorescence quantum yield of the donor in the absence of the acceptor, $n$ is the refractive index of the solvent, $\varepsilon_A(\lambda)$ is the molar extinction spectrum of the acceptor. The fluorescence quantum yield and molar extinction coefficient were
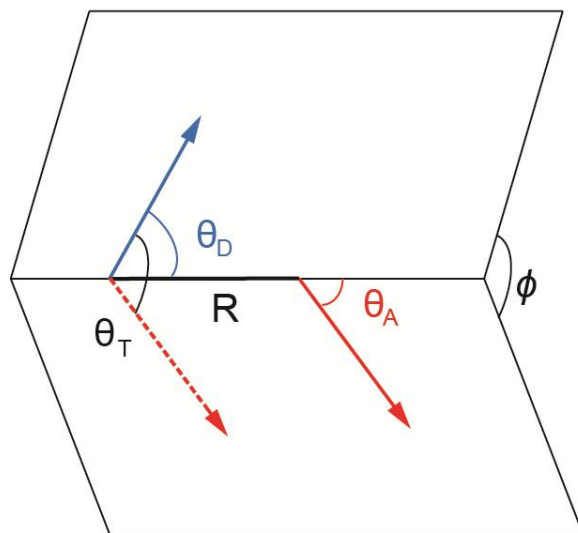
**Figure 2.3** Illustration of two transition dipole vectors. The inter-chromophore distance is given by $R$. The angle between the donor (blue) and the acceptor (red) dipole vectors is given by $\theta_T$. The angles of the donor/acceptor dipole vectors and the inter-chromophore axis are given by $\theta_D$ and $\theta_A$, respectively.

determined according to the procedures given above. The last term is the spectral overlap integral of the donor and the acceptor. The factor $\kappa^2$ describes the relative orientation of the donor and the acceptor transition dipoles, which is given in the following expression

$$\kappa^2 = (\cos\theta_T - 3\cos\theta_D \cos\theta_A)^2, \qquad (2.3)$$

where $\theta_T$ is the angle between the donor and the acceptor transition dipole vectors, $\theta_D$ is the angle between the donor dipole vector and the inter-chromophore axis, $\theta_A$ is the angle between the acceptor dipole vector and the inter-chromophore axis, as shown in Fig. 2.3. For random dipole orientations, $\kappa$ value of 2/3 was used.

### 2.4 Time-Correlated Single Photon Counting (TCSPC)

TCSPC is a time-resolved fluorescence measurement technique used to study fluorescence relaxation of molecules. TCSPC uses a pulsed light source as the excitation source. Typical light sources used include pulsed LEDs (~ns pulsewidths), dye lasers (~ps pulsewidths) as well as Ti:Sapphire lasers (~fs pulsewidths). The excitation light is split into two, one part is used to excite the sample and the other part goes to the fast electronics as the reference signal. The reference pulse is detected by a PIN diode and sent to a constant fraction discriminator (CFD) to generate a start pulse (or a stop pulse in the case of reverse mode). The start signal is then passed to a time-to-amplitude converter (TAC) to generate a voltage ramp that increases linearly over time. The fluorescence emission from the sample is detected by a single photon detector (a PMT or an avalanche photodiode (APD)). Once the detector detects the emitted photons from the sample, the CFD generates a stop timing pulse (or a start pulse in the case of reverse mode) and stops
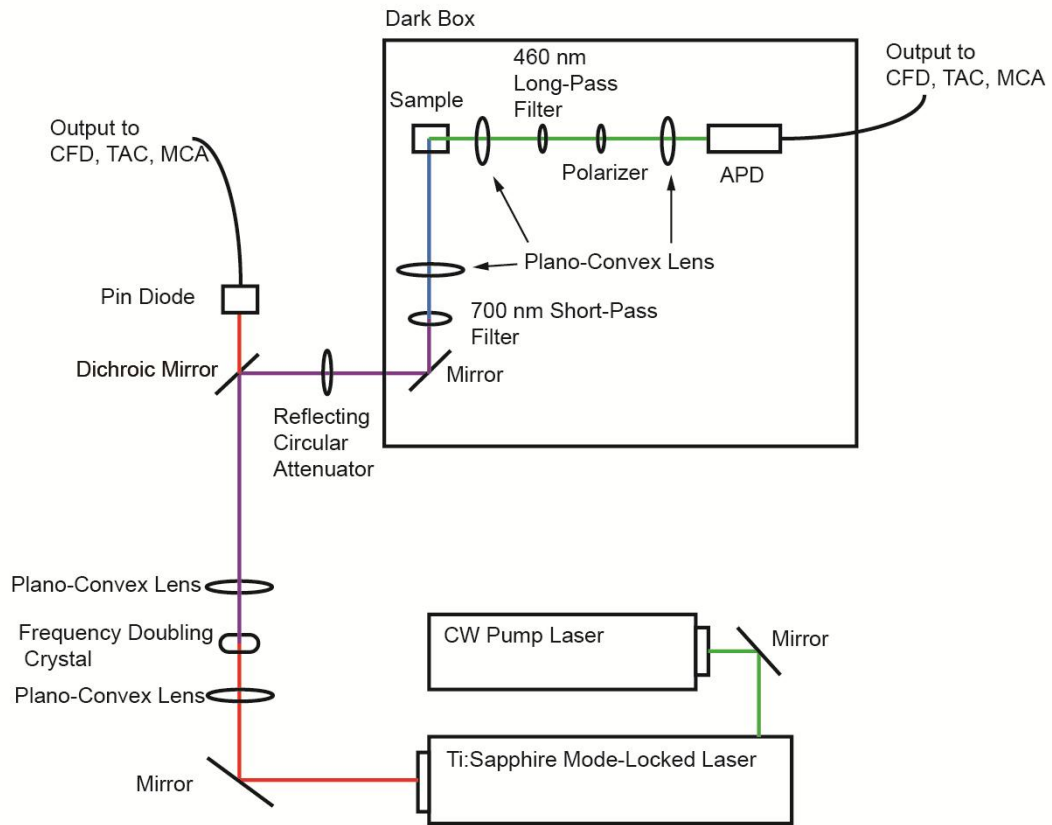
**Figure 2.4** Block diagram illustration of the time-correlated single photon counting setup.

the voltage ramp in the TAC. The interval between the arrival times of the two pulses is measured by the voltage and digitized by a multichannel analyzer (MCA) to store into corresponding bins. The arrival time of many photons were measured. The photon counts in the MCA bins were used to construct a decay histogram, which is the convolution of the instrument response function (IRF) and the actual fluorescence decay of the sample. The IRF is the instrument response to a zero lifetime sample, which is typically measure from a diluted scattering solution. The width of the IRF indicates the timing precision of the instrument, which is related to characteristics of the detector (the timing uncertainty in conversion of a photon to an electrical pulse) and the timing jitter/walk in the electronics.

Fluorescence lifetimes of CPNs were measured under $N_2$ atmosphere, using a home-built TCSPC setup operating in reverse mode (Fig. 2.4). The samples were excited by the second harmonic (420 nm) of a mode-locked Ti:Sapphire laser (Coherent Mira 900, 840 nm pulses, ~150 fs pulsewidth). The CPN fluorescence was collected in perpendicular to the excitation, passed through a 460 nm long pass filter, and detected by an APD (id Quantique, id100-50). The output of the detector was used as the start timing pulse for a TAC (Canberra Model 2145) and the output of a fast PIN diode (Thorlabs, DET210) was used as the stop pulse. The laser was attenuated (between 300 µW and 1 mW) to maintain a count rate of ~200 kHz at the APD for different samples. The analog TAC output was digitized by a 13 bit MCA (FastComTec, MCA-3A). The IRFs were measured using scattered excitation light from a dilute polystyrene microbeads (Invitrogen) suspension. To measure the dwell time per MCA bin, the delay times on the TAC was varied until

two IRF pulses showed up on the 20 ns time window. Based on the separation of the IRFs and the repetition rate of the Ti:sapphire laser, a dwell time of 2.63 ps/bin was obtained. The IRFs were measured before and after each lifetime measurement. The typical full width half maximum (fwhm) of the IRF was determined to be ~70 ps. The signal-to-noise ratio (SNR) of the measurement is governed by Poisson statistics,

$$SNR = \frac{N}{\sigma} = \frac{N}{\sqrt{N}} = \sqrt{N}.$$ (2.4)

As indicated by the equation 2.4, a SNR of 100:1 requires 10000 detected photons/bin. The typical SNR employed for measurement of CPNs was 500:1 at the peak (250000 detected photons/bin). The fluorescence lifetime of each sample was measured 3 times to ensure consistency.

As discussed above, the decay trace obtained from the TCSPC measurement is a convolution of the IRF and the actual fluorescence decay of the sample. To determine the fluorescence decay time constant, we convolve a trial decay function with the measured IRF,

$$S_{sim}(t) = IRF(t) \otimes F_{trial}(t).$$ (2.5)

We start from a single exponential trial function and gradually change the trial time constant to minimize the sum of the squared residuals. Typically, the fluorescence decay traces obtained from the measurements of conjugated polymers in THF could exhibit good fit to single exponential decay functions whereas the fluorescence decays of CPNs are more complex, require fitting with bi-exponential or Kohlrausch-Williams-Watts (KWW) functions. For the bi-exponential function, the average fluorescence lifetime was calculated by the weighted sum of the two time constants, $\langle \tau \rangle = (A_1 * \tau_1 + A_2 *$

$\tau_2)/(A_1 + A_2)$, whereas for the KWW function, the average fluorescence lifetime was calculated by the zero order moment of the KWW fit function, $\langle\tau\rangle = \tau_{kww}\,\beta^{-1}\Gamma(\beta^{-1})$.

## 2.5 Single Particle Spectroscopy

## 2.5.1 Single Particle Imaging

Single particle imaging was performed with a custom wide-field epifluorescence microscope described as follows (Fig. 2.5). A 445 nm excitation laser (Thorlabs, LP450) is passed through a liquid crystal noise eater (Thorlabs, NEL01) and then is guided to the rear epi port of an inverted fluorescence microscope (Olympus IX-71) by an optical fiber. The laser beam is reflected by a 500 nm long-pass dichroic (Chroma 500 DCLP) to a high numerical aperture objective (Olympus Ach, 100×, 1.25 NA, Oil). At the sample plane, the laser excitation exhibits a Gaussian profile with fwhm of ~5 μm. Various laser intensities were employed for the single particle imaging. Depending on the experiment, the typical excitation power at the center of the laser spot ranges from 50-500 W/cm$^2$. CPNs were dispersed on a glass coverslip by the same method used for preparing AFM samples. Fluorescence from the CPNs is collected by the objective lens, passes through a 500 nm long-pass filter and then is focused onto a sCMOS detector (Andor, Neo sCMOS), yielding a pixel pitch of 66 nm/pixel, as determined using a calibration slide. A piezoelectric scanning stage (P-517.3CL, Polytec PI) is used to position the sample. The overall fluorescence detection efficiency of the microscope is ~3%, determined from nile red loaded polystyrene beads (Thermo Fisher) as standards. Depending on the experiment, a variety of framerates ranging from 10 Hz to 1 kHz were used. At fast
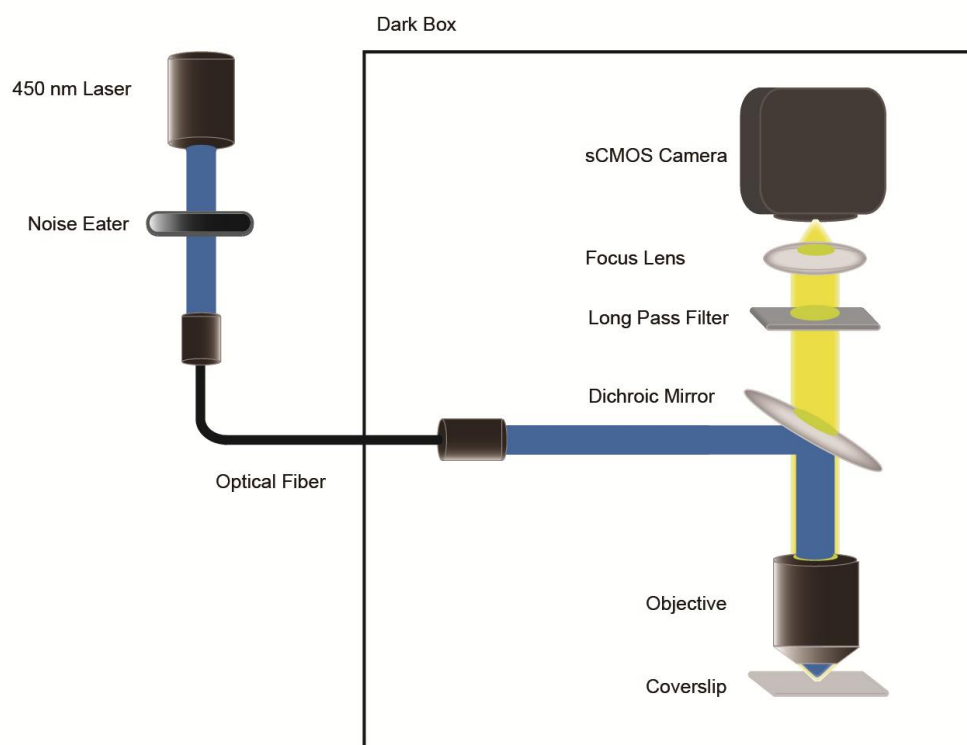
**Figure 2.5** Block diagram illustration of the single particle fluorescence microscopy setup.

framerates, the region of interest was set to the center of the sCMOS chip to maximize the performance of the camera. When the number of photons detected per pixel is small comparing to the well-depth, the typical camera settings are 11 bits per pixel, gain setting of 0.6, rolling shutter mode. When the particles are bright and the number of photons detected per pixel is comparable to the well-depth, the typical camera settings are 16 bits per pixel, gain setting of 1.6, rolling shutter mode. The experimental gain factors are determined by analysis of photon counting noise for a flat field, which are consistent with the factory values.

### 2.5.2 Single Particle Spectrum

To measure single particle fluorescence spectra, a transmission grating with 300 grooves/mm (Thorlabs, GT25-03) was placed between the 500 nm long-pass filter and the sCMOS camera to disperse the fluorescence emission from CPNs. Gaussian-shaped PSFs of single particles can be observed at the $n = 0$ spot while long stripes, which correspond to the fluorescence spectra of individual CPNs, can be observed at the $n = 1$ spot (Fig. 2.6 c, d). The bright stripe of each CPN was summed along the Y axis (10 pixels in total) to obtain the single particle emission spectrum. To calibrate the spectra, we replaced the 500 nm long-pass filter with a $540 \pm 10$ nm band-pass filter. We determined that the center of the $n = 0$ and $n = 1$ spots were separated by 773 pixels (Fig. 2.6 a, b). By dividing 450 nm with 773 pixels, we obtained a dispersion of 0.7 nm/pixel. Based on the single particle fluorescence spot width (PSF) of roughly 4-5 pixels
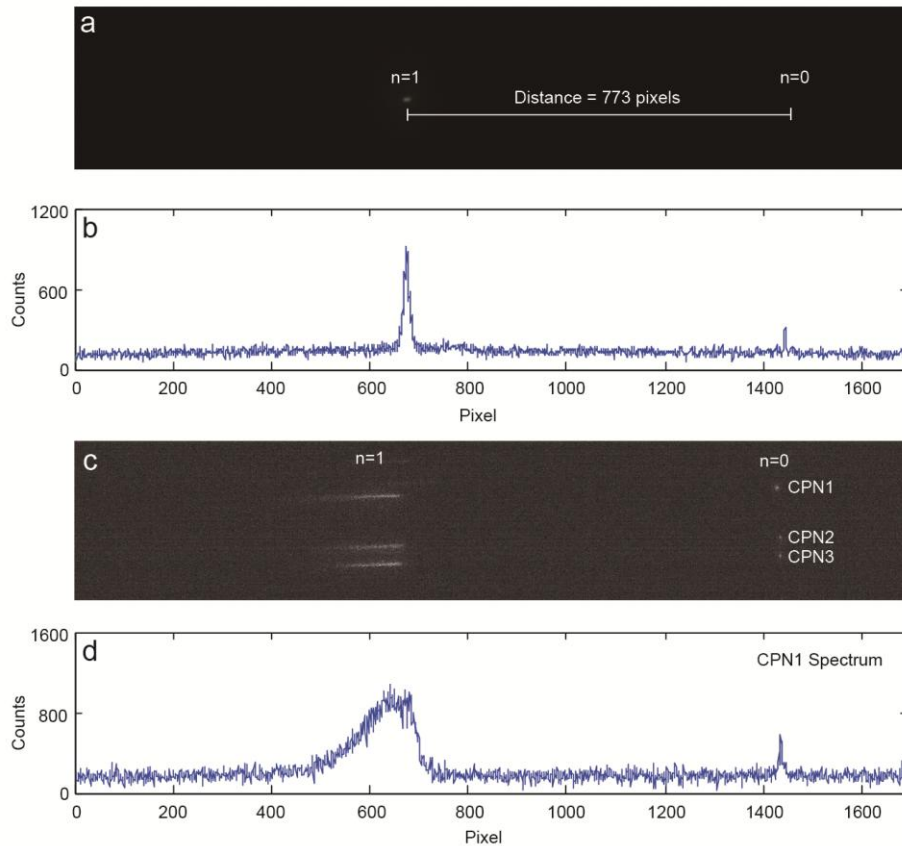
**Figure 2.6.** (a) Fluorescence microscopy images of a CPN, passed through a 540±10 nm band-pass filter. The distance between the n = 0 and n = 1 spot is highlighted by the white line. (b)The profile of the n = 0 and n = 1 spots in figure (a), along X axis. (c) Fluorescence microscopy images of 3 CPNs, passed through a 500 nm long-pass filter. (b) The profile of the n = 0 and n = 1 spots of CPN1, along X axis.

(FWHM), which roughly corresponds to the "slit width" of the spectrometer, the spectroscopic resolution is roughly 3.5 nm.

### 2.5.3 Single Particle Localization

The localization analysis of CPNs was performed using custom scripts written in Matlab (Mathworks). To determine small movements in the fluorescence centroid associated with polaron motion, the scripts first sum over all the frames, find the intensity of the brightest pixel in the summed image and use 5-10% of the intensity as a threshold to distinguish CPNs from the background noise. Then the scripts search for pixels above the threshold in the summed image and compare their intensities to the neighboring pixels to roughly locate the central pixel of the fluorescence spot of each CPN. Based on the rough locations of CPNs, a 2D Gaussian function was fit to the fluorescence spot of each CPN, frame by frame. Typically $9 \times 9$ pixels were used for the fitting (4 pixels on each side of the central pixel). The scripts check the FWHM obtained from the fitting (should be around ~270 nm) to make sure it is not from multiple CPNs that are close to each other. In the end, the centroid position trajectory of a CPN was constructed from the centroid positions determined from the corresponding fluorescence spot in all the frames.

A slightly different method was used to determine the position of photoswitching CPNs. When imaging a biological sample, sometimes background subtraction is needed in order to ensure optimal localization accuracy. The background fluorescence was determined from the frames with no CPN switched "on". ~100 frames of the background fluorescence were averaged and subtracted from each frame prior to analysis. After the

subtraction, the scripts first find the intensity of the brightest pixel of all frames, then use 5-15% of the intensity as a threshold to distinguish CPNs from the background noise (a higher threshold might be needed, if the autofluorescence is not effectively corrected). For each frame, the scripts search for pixels above the threshold and compare their intensities to the neighboring pixels to roughly locate the central pixel of the fluorescence spot of each CPN. Then the fluorescence centroid positions of the CPNs were determined by nonlinear least-squares fitting of a 2D Gaussian function to the fluorescence spots. Typically $9 \times 9$ pixels were used for the fitting (4 pixels on each side of the central pixel). In the end, the scripts check the FWHM obtained from the fitting to make sure it is not from multiple close by CPNs. The localized positions obtained from each frame were then used to construct the shape of the biological sample.

Vibration correction is needed for both cases. In general, there are typically a few percent of the CPNs showing minimal photoblinking, consistent with large particles or aggregates. It was observed that the non-blinking particles or aggregates in the image exhibit highly correlated slow movement in the centroid position, due to drift and vibrations from the environment. For each frame, the non-blinking particles were used as markers to measure at each frame how far the sample travelled relative to the previous frame. The displacement was then subtracted from the localized positions of all the CPNs in the current frame. The experimental localization precision can be measured in multiple ways. For photoswitching CPNs, the experimental localization precision was determined from the standard deviation of the localized position distribution (i.e., the per-frame position uncertainty is obtained from a sequence of consecutive frames during an "on"

cycle). For CPNs showing clear movements in the fluorescence centroid caused by polaron motion, the experimental localization precision was determined from the root mean square displacement of the centroid position trajectory at lag time 0. Under typical imaging conditions, due to the high brightness of CPNs, the number of photons used in the localization is typically large (>2000). The experimentally determined localization precision is consistent with the theoretical localization uncertainties determined from the equation $\sigma = s/\sqrt{N}$, where $s$ is the standard deviation (STD) of the PSF and $N$ is the number of detected photons used in the fitting. When the number of photons used in the localization is small (<1000), addition source of localization uncertainty should be considered. Thompson et al modeled the effect of pixel size and background noise on the localization precision (assuming a gaussian PSF), which is given by the following expression,[85]

$$\sigma = \sqrt{\frac{s^2}{N} + \frac{\alpha^2/12}{N} + \frac{8\pi s^4 b^2}{\alpha^2 N^2}}, \tag{2.6}$$

where $s$ is the STD of the PSF and $N$ is the number of detected photons used in the fitting, $\alpha$ is the pixel size, $b$ is the background noise. STD of the single particle fluorescence spot is 130 nm. The pixel size of the setup is 66 nm and the background noise (due primarily to readout noise, autofluorescence, and scattered light) ranges from roughly 1.5 to 10, depending on conditions. Assuming that $N$=2000, $b$=1.5, we obtained a localization precision of 3.0 nm. The shot noise term contributed to 95% of the uncertainty. The second (pixel size) and the third term (background noise) only contributed to 5%. If we lower the number of detected photons to 500, the shot noise term still contributed to 85%

of the uncertainty, the background noise contributed to 14% and the pixel size term only contributed to <1%. According to these results, the shot-noise-limited expression, $\sigma = s/\sqrt{N}$ is fairly accurate for most of the conditions. Only when $N$<1000, background noise needs to considered. That said, in some cases, due to the presence of a high background caused by autofluorescence of the sample or residual fluorescence of dyes or particles in the "off" state, background subtraction is required in order to perform single particle localization. The subtraction procedure can introduce additional uncertainty (for example, shot noise from autofluorescence), and thus equation 2.6 is not a reliable estimate of the overall localization uncertainty. In such cases, experimental uncertainty is typically compared to computer-generated quasi-random data with noise characteristics that closely match the experiment. In other words, a Monte Carlo approach to estimating the expected localization uncertainty is performed, based on the standard Monte Carlo approach for propagating uncertainty.[94]

It should be noted that the procedures discussed above only suit for analysis of fixed particles. For localization of particles exhibiting Brownian motion in solution, the situation is more complicated. The size of the fluorescence spot could change over time due to particles diffusing in and out of focus, which requires carefully setting of thresholds for intensity and PSF width. In some algorithms, local maxima detection is used instead of a global threshold.[95] Additionally, random motion of the particle during the integration period for a given frame can give rise to blurred or even asymmetric spot shapes (i.e., motion blur) and can contribute to the measured mean squared displacement.[96] Proper corrections for motion blur need to be applied to obtain accurate

diffusion coefficients and to correct the estimate of tracking uncertainty obtained by extrapolating the mean squared displacement to zero lag time (e.g., in some cases motion blur leads to a negative value of the mean squared displacement extrapolated to zero lag time). Linking particle positions in different frames to obtain trajectories is also challenging. A variety of methods, including nearest-neighbor linking, multiple hypothesis tracking, multiple frame association, could be used to construct the trajectory. Detailed reviews of particle tracking and comparison of different algorithms can be found elsewhere.[95, 97]

CHAPTER THREE


SUPERRESOLUTION IMAGING USING TELEGRAPH NOISE IN ORGANIC

SEMICONDUCTOR NANOPARTICLES

## 3.1 Introduction

In recent years, driven by the interest of studying cellular structures and processes beyond the diffraction limit, superresolution imaging techniques have undergone rapid growth. Various photophysical processes, such as, photoactivation,[83] photoswitching,[84] stimulated emission[98] and inter-system crossing[82], have been utilized to overcome the diffraction limit. The development of superresolution fluorescent probes, including photoactivatable proteins,[83, 99] photoswitchable dyes,[100, 101] proteins[102, 103] and nanoparticles[104, 105] have improved the spatial resolution of optical microscope to <10 nm, which enables us to image cellular structures in an unprecedented level of detail.

To further improve the spatial resolution of superresolution microscopy, photoswitchable fluorescent probes with high brightness, good reversibility, and high on/off contrast are required. Owing to the exceptional brightness and photostability of CPNs,[10-12] there has been considerable interest in developing photoswitchable nanoparticle based on CPNs.[105, 106] Previous efforts in modifying CPNs or other

fluorescent nanoparticles for superresolution imaging typically involve incorporating or linking photochromic dyes to the nanoparticles. However, these nanoparticles either do not exhibit single-step switching or suffer from poor on/off contrast due to incomplete quenching of the nanoparticle fluorescence. In this work, we demonstrate a novel method that utilizes controlled reversible generation and recombination of hole polarons inside CPNs to achieve superresolution imaging. Hole polarons are known to be highly efficient fluorescence quenchers in conjugated polymer systems.[31, 32, 107, 108] Nanoparticles of the conjugated polymer PFBT doped with the fullerene derivative PCBM, rapidly establish a large population of hole polaron charge carriers, sufficient to nearly completely suppress nanoparticle fluorescence. However, fluctuations in the number of charges lead to occasional bursts of fluorescence, which is similar to the random telegraph signal noise observed in semiconductor devices.[109] The repeated, spontaneous generation of short, intense bursts of fluorescence photons ($3-5 \times 10^4$ photons detected per switching event, on average) are roughly 1-2 orders of magnitude brighter than those of photoswitching dye molecules, resulting in a localization precision of ~0.6 nm, about 4 times better than the typical resolution obtained by localization of dye molecules.[110]

## 3.2 Nanoparticle Preparation and Characterization

Nanoparticles of the conjugated polymer PFBT doped with various percentages of PCBM were prepared using nano-precipitation method described previously.[26, 30, 111] 20 ppm solutions of PFBT and PCBM in THF were prepared and filtered through a 0.45 μm membrane filter (Millipore). The solutions of PFBT and PCBM were mixed in various
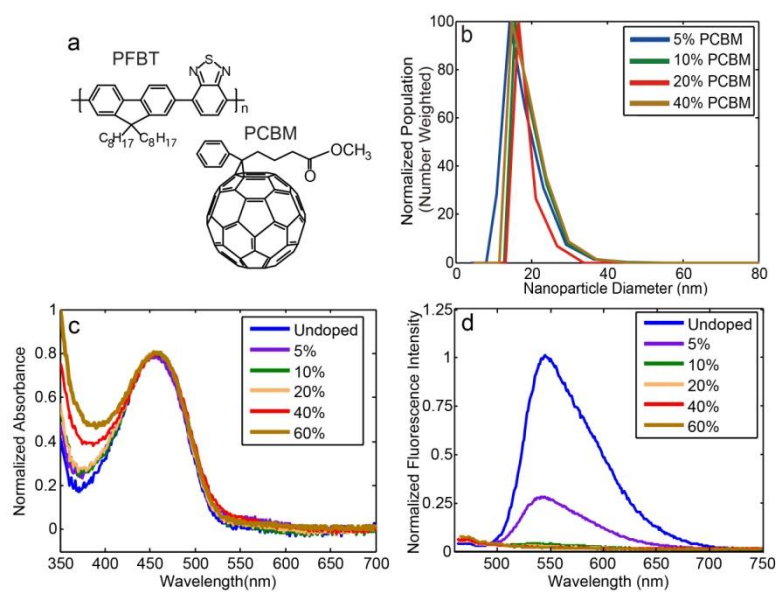
**Figure 3.1.** (a) Chemical structures of PFBT and PCBM. (b) Number weighted particle size distributions of PCBM doped PFBT CPNs at various PCBM doping percentages, determined from DLS measurements. (c, d) Normalized absorption and fluorescence spectra (excited at 450 nm) of PCBM doped PFBT CPNs at various PCBM doping percentages.
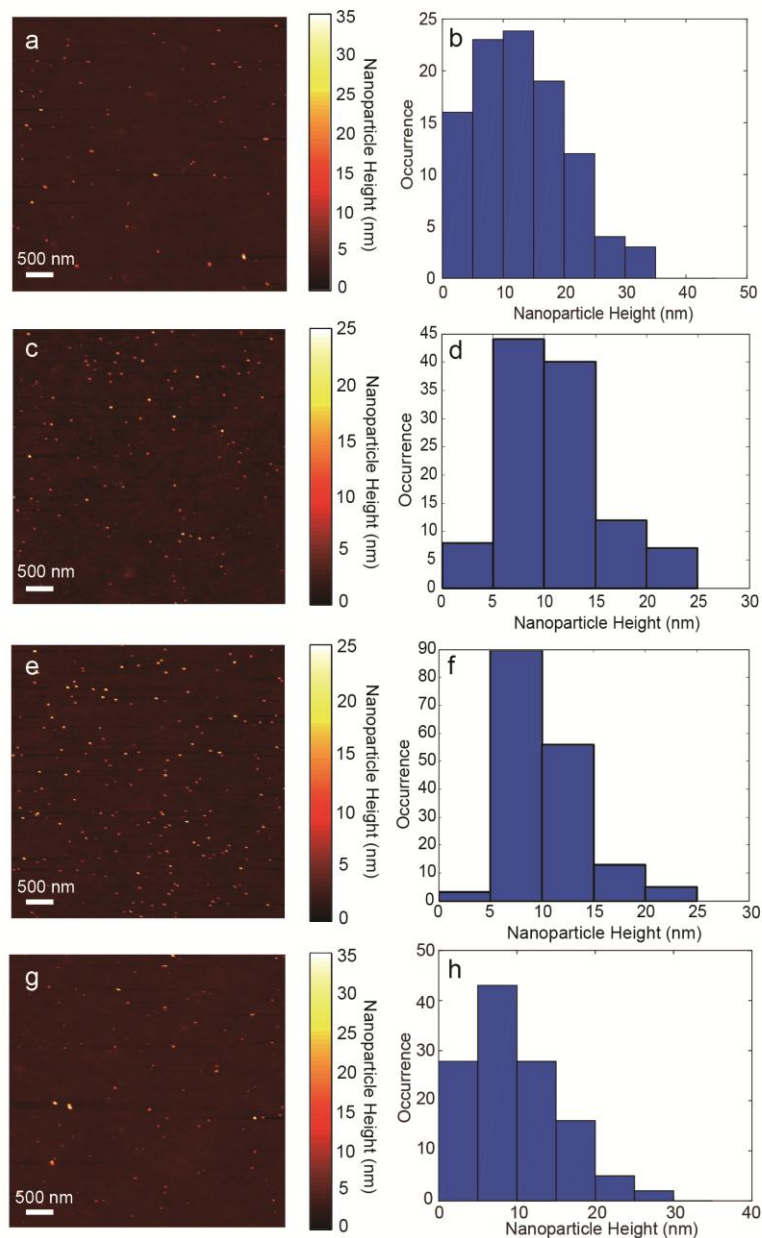
**Figure 3.2.** (a) AFM image and (b) size distribution of 5% PCBM doped PFBT nanoparticles (12.9±5.8 nm); (c) AFM image and (d) size distribution of 10% PCBM doped PFBT nanoparticles (10.7±3.9 nm); (e) AFM image and (f) size distribution of 20% PCBM doped PFBT nanoparticles (9.9±4.2 nm); (g) AFM image and (h) size distribution of 40% PCBM doped PFBT nanoparticles (10.2±4.5 nm).

ratios to form precursors of varying dopant percentages (5%, 10%, 20%, 40%). 2 mL of the precursor solution was rapidly injected into 8 mL of water under mild sonication. Then the THF solvent was removed by partial vacuum evaporation. After evaporation, the sample was filtered through a 100 nm membrane filter (Millipore) to remove aggregates. The size distribution of the nanoparticles was determined using AFM and DLS. No significant difference in particle size was observed throughout the doping range, as shown in Fig. 3.1 b and Fig. 3.2. The typical particle sizes determined from AFM and DLS are $10.2\pm3.5$ nm, $14.4\pm4.4$ nm in diameter, respectively. As PCBM doping percentage increases, the nanoparticle absorption at low wavelength (< 400 nm) increases, which corresponds to PCBM absorption, while the absorption peak of PFBT remains unchanged at 450 nm (Fig. 3.1 c). The presence of PCBM effectively quenched the fluorescence of PFBT--at 5% PCBM doping ratio, the fluorescence quantum yield dropped by 70% as compared to undoped PFBT CPNs (Fig. 3.1 d). The pronounced fluorescence quenching observed is likely a combined effect of efficient charge generation at the polymer/PCBM interface and energy funneling from excitons to hole polarons, which has been previously discussed in spectroscopic study of other polymer/PCBM systems.[112, 113]


## 3.3 Picosecond Time-Resolved Fluorescence Measurement

The picosecond time-resolved fluorescence decay traces of PCBM doped PFBT CPNs were measured under $N_2$ atmosphere, using a TCSPC setup operating in the reverse mode. The fluorescence decay traces obtained were fit to single exponential, bi-
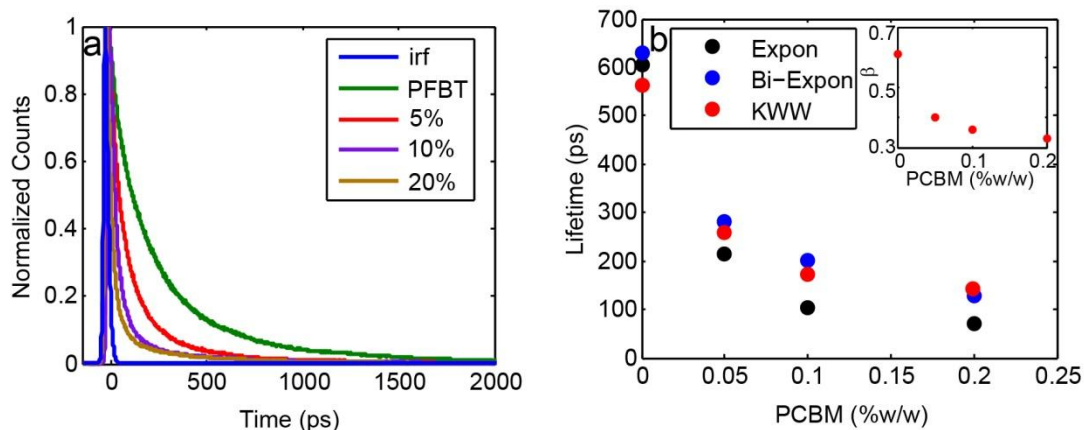
**Figure 3.3** (a) Normalized fluorescence intensity decays for PFBT and PCBM doped PFBT

CPNs. (b) The fluorescence lifetimes of PFBT and PCBM doped PFBT CPNs, obtained from

the single exponential fit time constants, the bi-exponential weighted average time constants,

and the zero moment of the KWW fit function $\langle \tau \rangle = \frac{\tau_{kww}}{\beta} \Gamma(\frac{1}{\beta})$. The inserted plot shows the

stretch parameter β from KWW fitting versus PCBM doping percentage.

exponential and the Kohlrausch-Williams-Watts (KWW) functions. Analysis of different runs yielded consistent lifetime results with <10% variation. The typical fitting results are summarized in Fig. 3.3. The intensity decays show poor fit to a single-exponential while fitting better to a bi-exponential or KWW function, indicating heterogeneity in the fluorescence decay rate. As PCBM doping percentage increases, the fluorescence lifetime of the PCBM doped PFBT CPNs decreases monotonically. For undoped PFBT CPNs, a weighted average fluorescence lifetime of ~600 ps was obtained from the bi-exponential fitting, which is consistent with the previously reported values.[10] As the PCBM doping percentage increases to 20%, the weighted average fluorescence lifetime drops to ~150 ps according to the bi-exponential fitting result. The fluorescence lifetime heterogeneity also increases with the PCBM percentage, as indicated by the smaller stretch parameter $\beta$ obtained from the KWW fitting at higher PCBM doping percentages. The reduced fluorescence lifetime and increased lifetime heterogeneity at high PCBM doping level are consistent with the physical picture of a large polaron population inside PCBM doped PFBT CPNs and energy funneling from excitons to hole polarons.

## 3.4 Single Particle Fluorescence and Localization Study

The single particle fluorescence study of PCBM doped PFBT CPNs was carried out with an inverted microscope. The CPNs were dispersed on a glass coverslip and excited with a 445 nm laser. A sequence of fluorescence microscopy images were acquired at multiple framerates (1Hz, 10Hz or 50Hz) using a sCMOS camera, for over 600 s. It is found that the blinking behavior of PCBM doped PFBT CPNs is highly sensitive to the
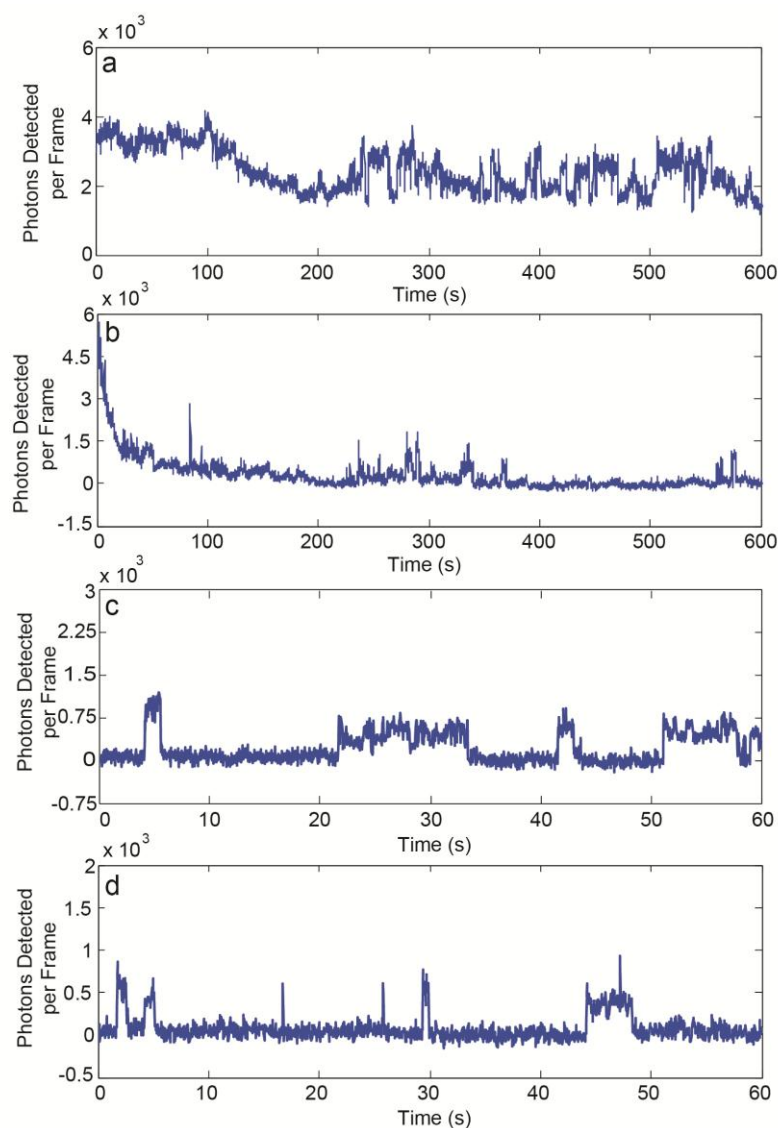
**Figure 3.4.** (a) The trajectory of a 10% PCBM doped PFBT CPN, showing multiple level blinking behavior without turning "off", acquired at 400 W/cm$^2$, 10 Hz framerate. (b) The trajectory of a 40% PCBM doped PFBT CPN, showing distinctive initial decay, acquired at 400 W/cm$^2$, 10 Hz framerate. (c) (d) Two trajectories of 20% PCBM doped PFBT CPNs, acquired at 400 W/cm$^2$, 50 Hz framerate. The trajectories were zoomed in to 60 s to show stepwise blinking.

dopant concentration. At low PCBM doping level (<10%), the fluorescence intensity of the doped CPNs jumps between multiple levels (Fig. 3.4 a), indicating fluctuations in the quencher population, however, most of the nanoparticles don't turn "off" during the experiment. When the PCBM percentage is higher (>20%), we typically observe transitions between a dark state and multiple "on" states in the single particle fluorescence (Fig. 3.4 c, d). Upon further increase of the PCBM doping level (>40%), the frequency and duration of "on" events is further reduced. The single particle fluorescence study was mainly focused on 20% and 40% PCBM doped PFBT CPNs because the frequency and duration of "on" events in this doping range appeared promising for single particle localization. For some CPNs, we observed a distinctive initial decay in fluorescence intensity followed by "on" and "off" blinking behavior (Fig. 3.4 b), which is likely caused by polaron population establishing an equilibrium. A similar phenomenon was also observed for undoped CPNs, discussion and modeling of the initial fluorescence decay dynamics arising from polaron generation can be found elsewhere.[12]

The blinking trajectories of PCBM doped PFBT CPNs were analyzed using a photon-counting histogram method in order to obtain information about the number and prevalence of various intensity states. The histogram constructed from the fluorescence intensities of each frame typically shows clustering indicating a few distinguishable states, including an "off" state and one or more "on' state(s), as shown in Fig. 3.5. A threshold to differentiate the "off" state from the "on" states can be set in the flat region between the "off" state peak and the first "on" state peak (Fig. 3.5 b). Based on the threshold, the "on"/"off" contrast ratio can be calculated by $\langle I_{on} \rangle / \langle I_{off} \rangle$. Then we built
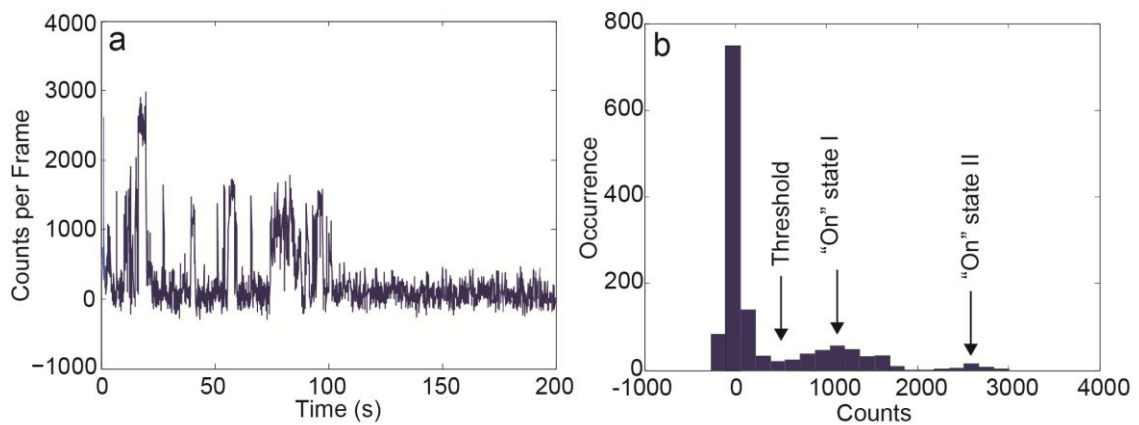
**Figure 3.5.** (a) The intensity trajectory of a 40% PCBM doped PFBT CPNs, showing blinking behavior. (b) The corresponding fluorescence intensity histogram, showing multiple peaks.

histograms of "on" durations, number of photons detected per "on" event according to the threshold. Single exponential decays were employed in fitting of the histograms. Parameters such as the average "on" duration, average number of photons detected per "on" event were determined from the fitting.

Since polaron generation is a photo-driven process and polaron population in CPNs is likely to be excitation intensity dependent, we used various excitation intensities to modulate the blinking behavior of 20% PCBM doped PFTB CPNs. For each laser intensity, dozens of single particle blinking trajectories were analyzed. The results are summarized in the table 3.1. According to the table 3.1, the duty cycle of the blinking CPNs (fraction of time in the "on" state) depends on excitation intensity. At higher excitation intensity, the increased polaron generation rate and equilibrium population lead both to fewer "on" events per unit time and reduced "on" state durations (Fig. 3.6 d). If we assume that the polaron population fluctuations in CPNs follow Poisson statistics, the duty cycle $D$ can be written as a function of the equilibrium polaron population in CPNs,

$$D = 1 - \sum_{i=0}^{n_q} \frac{n_{eq}^i e^{-n_{eq}}}{i!}, \tag{3.1}$$

where $n_q$ is the number of polarons required to totally quench the fluorescence of a CPN and $n_{eq}$ is the equilibrium polaron population inside the CPN. Based on the previously estimated polaron quenching efficiency (~10%) in undoped PFBT CPNs, we assume that $n_q = 10$. According to the equation 3.1 and duty cycles determined in the table 3.1, we estimated that the equilibrium polaron populations in 20% PCBM doped PFBT CPNs
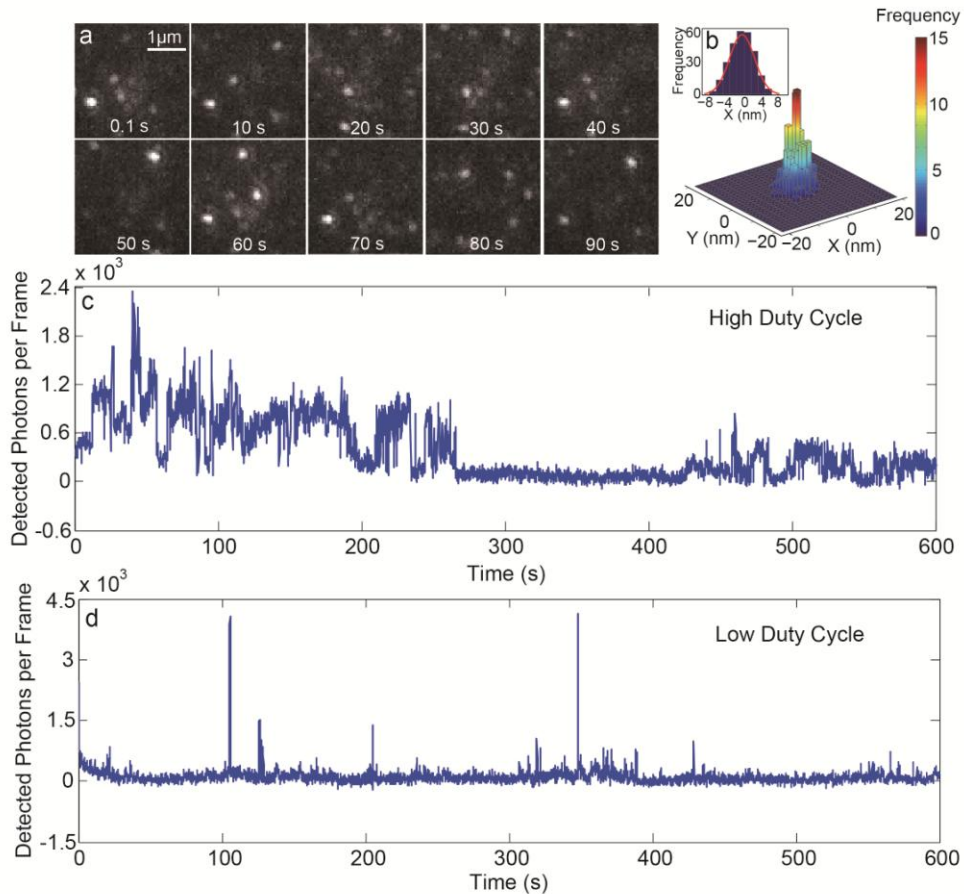
**Figure 3.6.** (a) A sequence of fluorescence microscopy images showing the blinking behavior of 20% PCBM doped PFBT CPNs. (b) 3D histogram of the localized centroid position of a blinking 20% PCBM doped PFBT CPN, determined frame by frame from a trajectory acquired at $200W/cm^2$, 1 Hz framerate. The inserted plot shows the centroid position histogram along X axis of the same CPN, which is fit to a Gaussian distribution ($\sigma = 2.1$ nm). (c, d) Fluorescence intensity trajectories of 20% PCBM doped PFBT CPNs acquired at 10 Hz framerate, two excitation powers, (c) 200 W/cm$^2$, (d) 800 W/cm$^2$, showing different duty cycles.

**Table 3.1.** Blinking parameters of 20% PCBM doped PFBT CPNs, determined at 50 Hz framerate.

| Excitation Intensity | "On"/"off" contrast | "On" duration (s) | Duty cycle | Photons detected per "on" event | Number of cycles before photobleach |
|---|---|---|---|---|---|
| 200 W/cm$^2$ | 10.1±4.3 | 8.2±5.9 | 0.28±0.10 | 5.2±2.8×10$^4$ | 22.6±8.8 |
| 400 W/cm$^2$ | 13.9±6.2 | 4.9±3.5 | 0.16±0.07 | 3.8±2.0×10$^4$ | 19.9±6.9 |
| 800 W/cm$^2$ | 15.3±6.5 | 3.4±1.6 | 0.05±0.04 | 3.5±2.2×10$^4$ | 20.7±7.4 |
| 1600 W/cm$^2$ | 16.7±5.9 | 2.1±1.2 | 0.008±0.01 | 3.0±1.8×10$^4$ | 15.9±9.0 |

under 200W/cm$^2$, 400W/cm$^2$, 800W/cm$^2$, 1600W/cm$^2$ excitation intensities to be 12, 14, 17, 21 respectively, assuming $n_q = 10$. The larger polaron population at high excitation intensities nearly completely suppresses the polymer fluorescence--only low probability large fluctuations in the polaron population lead to occasional, rare fluorescence bursts.

Assuming the localization precision is shot noise limited, the theoretical localization precision or uncertainty is given by $\sigma = s/\sqrt{N}$, where $s$ is the STD of the PSF and $N$ is the number of detected photons.[85] For 20% PCBM doped PFTB CPNs, under low laser excitation intensity (200W/cm$^2$) and 1 Hz framerate, an average of $6.3 \times 10^3$ photons were detected per frame during "on" state, yielding a theoretical per frame localization precision of ~1.7 nm. The total number of photons detected per switching event was calculated by integrating over all the frames during an "on" event. Under 200W/cm$^2$, the average "on" duration is ~8 s, an average of $5.2 \times 10^4$ photons were detected per switching event (1-2 orders of magnitude higher than dye molecules), resulting in an expected theoretical localization precision of ~0.6 nm, about 4 times better than the typical resolution obtained by localization of photoswitching dye molecules.[110] The expected resolution is confirmed by frame-by-frame centroid analysis of single burst events. Fig. 3.6 b shows the centroid position histogram of a representative 20% PCBM doped PFTB CPN, imaged under 200W/cm$^2$, 1 Hz framerate for 600 s. For this CPN, an average of $6.1 \times 10^3$ photons were detected per frame during each "on" event. An experimental per frame localization uncertainty of 2.08 nm was calculated from the STD of X and Y centroid positions ($\sigma_x = 2.10$ nm, $\sigma_y = 2.06$ nm) using equation $\sigma = (\sigma_x + \sigma_y)/2$. The experimental per-frame localization precision is roughly consistent with the theoretical

localization uncertainty (based on spot width and photon counting noise) of 1.7 nm per frame. Averaging the centroids from the (typical) ~8 frames from a single "on" event yields an expected localization precision of 0.74 nm (per "on" event), roughly consistent with the theoretical shot-noise-limited value of 0.6 nm, indicating that the particles perform as expected for single particle localization and confirming our initial assumption that the high brightness of PCBM-doped CPNs should yield significantly improved localization precision as compared to dyes.

**3.5 Simulation of Power Dependent Blinking of PCBM Doped PFBT CPNs**

Above, we used a Poisson statistics model to explain the power dependent duty cycle of PCBM doped PFBT CPNs. An alternative approach to understand the phenomenon is to use rate equations to simulate polaron population fluctuation inside CPNs. The polaron kinetics equation can be written as:

$$\frac{dn_p}{dt} = k_{gen} - k_{rec}n_p. \tag{3.2}$$

The first term $k_{gen}$ represents the polaron generation rate, which is excitation power dependent. The second term represents the polaron recombination rate, $n_p$ is the polaron population and $k_{rec}$ is the recombination rate constant. When a CPN is exposed to excitation, the polaron population will grow from 0 to a steady state value. As discussed previously, this process can be described by the following equations,[12]

$$n_p(t) = \frac{k_{gen}}{k_{rec}} - \frac{k_{gen}}{k_{rec}}e^{-k_{rec}t}, \tag{3.3}$$

$$n_p^* = \frac{k_{gen}}{k_{rec}}. \tag{3.4}$$

The equation 3.3 describes the polaron population growth process and the equation 3.4 gives the expression of equilibrium polaron population $n_p^*$, which depends on the excitation power. Previous single molecular study of undoped PFBT CPNs yielded polaron lifetimes ranging from several seconds to tens of seconds.[59] Therefore, $k_{rec}=$ 0.05 s$^{-1}$ was used for the simulation. In the previous section, we estimated that the equilibrium polaron populations $n_p^*$ in 20% PCBM doped PFBT CPNs under 200W/cm$^2$, 400W/cm$^2$, 800W/cm$^2$, 1600W/cm$^2$ excitation intensities to be 12, 14, 17, 21 respectively. According to these numbers and the equation 3.4, $k_{gen}=$ 0.6 s$^{-1}$, 0.7 s$^{-1}$, 0.85 s$^{-1}$, 1.05 s$^{-1}$ were used to simulate the blinking behavior of 20% PCBM doped PFBT CPNs under 200W/cm$^2$, 400W/cm$^2$, 800W/cm$^2$, 1600W/cm$^2$ excitation intensities respectively. Based on the previously estimated polaron quenching efficiency and quenching radius,[59] we assumed that each polaron has a quenching efficiency $Q_e = 10\%$ and we assumed that the quenching process is linear such that 10 polarons will completely quench the fluorescence of a CPN. There is probably some deviation from linearity, but we don't currently know the functional form, and in any case the fluctuations in polaron population are small in the context of this simulation, so we can treat the quenching as linear. The fluorescence intensity $I$ of a CPN then can be written as a function of the polaron population,

$$I = I_0(1 - Q_e n_p), n_p < 10 \tag{3.5}$$

$$I = 0, n_p \geq 10 \tag{3.6}$$
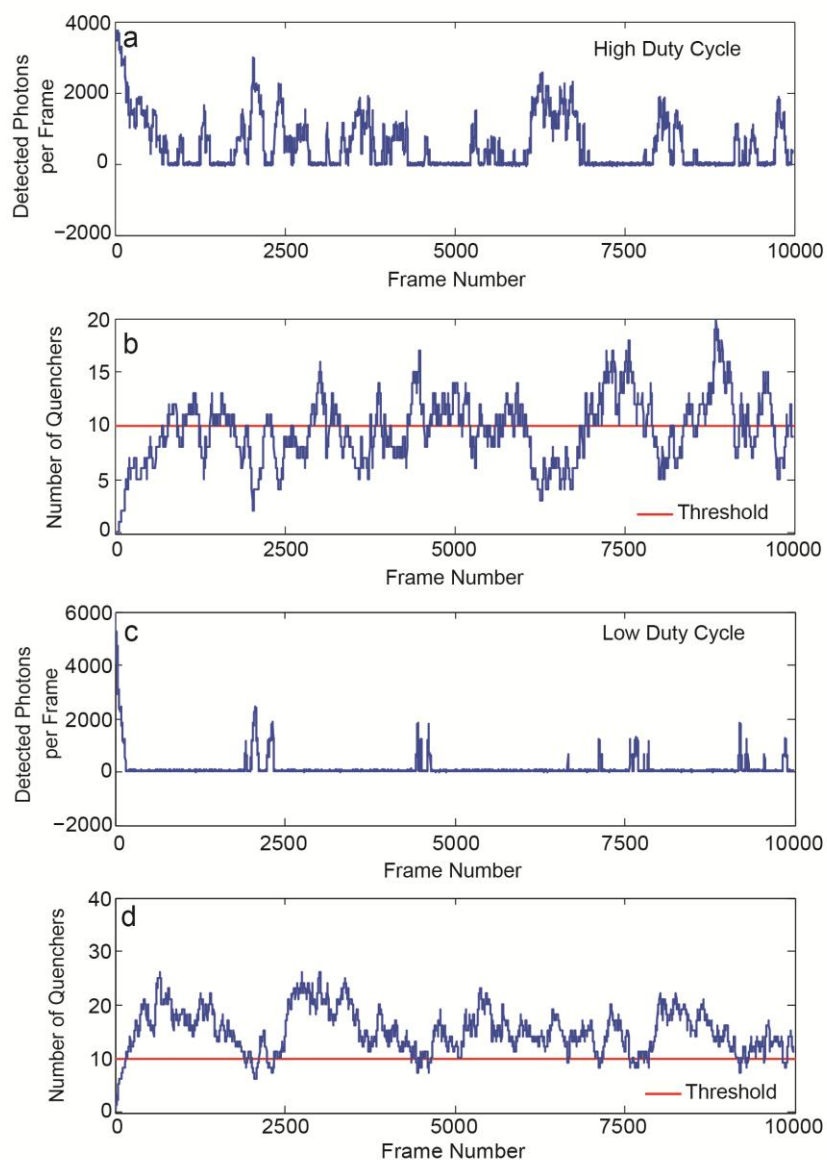
**Figure 3.7.** (a,b) Stochastic simulations of internal polaron population fluctuations and the corresponding fluorescence intensity trajectory of a PCBM doped PFBT CPN under $200W/cm^2$. (c,d) Stochastic simulations of internal polaron population fluctuations and the corresponding fluorescence intensity trajectory of a PCBM doped PFBT CPN under $800W/cm^2$.

**Table 3.2.** Blinking parameters determined from the simulations

| Excitation Intensity | "On" duration (s) | Duty cycle | Photons detected per "on" event |
|---|---|---|---|
| 200 W/cm$^2$ | 6.7±0.7 | 0.36±0.06 | 4.3±1.1×10$^4$ |
| 400 W/cm$^2$ | 4.0±0.5 | 0.14±0.02 | 3.7±1.1×10$^4$ |
| 800 W/cm$^2$ | 2.7±0.3 | 0.05±0.01 | 3.4±1.0×10$^4$ |
| 1600 W/cm$^2$ | 1.6±0.4 | 0.007±0.005 | 3.1±0.8×10$^4$ |

$I_0$ is the number of photons detected per second without quencher, which is proportional to the excitation power. $I_0 = 4 \times 10^4$ counts/s, $8 \times 10^4$ counts/s, $1.6 \times 10^5$ counts/s, $3.2 \times 10^5$ counts/s were used for $200W/cm^2$, $400W/cm^2$, $800W/cm^2$, $1600W/cm^2$ excitation intensities, respectively. Using the equations and the parameters above, we simulated stochastic fluorescence intensity trajectories of 20% PCBM doped PFBT CPNs at four excitation intensities, 10 Hz framerate. For each condition, $4 \times 10^4$ frames were simulated and repeated for 10 runs. The blinking parameters determined from the simulations (table 3.2) are highly consistent with the experimental values. As shown in Fig. 3.7, at higher excitation intensities, the increased polaron generation rate and equilibrium population lead both to fewer "on" events per unit time and reduced "on" state durations, which results in the lower duty cycles. It should be noted that the polaron generation/recombination dynamics are highly dependent on the local structure. At the polymer/PCBM interface, charge separation is likely to be instantaneous whereas in the regions far away from the interface, charge generation is much slower. Therefore, the parameters obtained from the kinetic model here are the averages of highly heterogeneous dynamics. Addition experiment is required in order to obtain a complete physical picture of charge generation/recombination processes in such a complex system.

### 3.6 Superresolution Imaging of *E. coli*

Superresolution microscopy based on PCBM doped PFBT CPNs was demonstrated on *Escherichia coli* (*E. coli*). *E. coli* stocks were frozen in glycerol at -80 °C. Prior to each experiment, *E. coli* was streaked on a LB-Kan-Amp plate, single colonies were selected
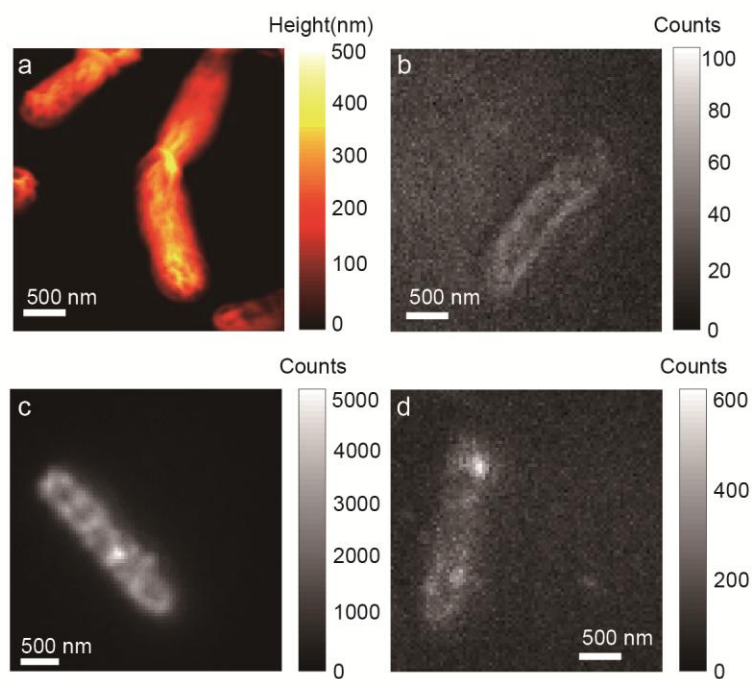
**Figure 3.8.** (a) An AFM image of unlabeled *E. coli*, (b, c, d) Fluorescence microscopy images of (b) unlabeled *E. coli*, (c) *E. coli* labeled with PFBT CPNs, (d) *E. coli* labeled with 40% PCBM doped PFBT CPNs, imaged under 800W/cm$^2$ excitation, 10 Hz framerates.

for growth in low-fluorescence media (1X Gibco M9 minimal media, 1% glucose, 100 ug/mL leucine, 25 mg/L ferric citrate, 50 ug/mL thiamine), supplemented with kanamycin and ampicillin, overnight at 37 °C (approximately 16-20 hours). The bacteria were then dispersed on a glass coverslip and washed with phosphate-buffered saline (PBS) three times. The bacteria fixation was carried out by submerging *E. coli* under ice cold methanol for 10 min. The *E. coli* were washed with PBS buffer for three times after fixation. The fixed bacteria were rinsed with a solution of a cationic surfactant, (1-hexadecyl) trimethylammonium bromide (0.01M), to introduce positive charges to the bacteria surface. The bacteria were then submerged under $200\,\mu L$ of nanoparticle suspension (~1 nM) for 30 mins and washed with PBS buffer afterwards. It was observed that PCBM doped PFBT CPNs (with a zeta potential around -35mV) were efficiently adsorbed on the positively charged bacteria surface (hundreds of CPNs per *E. coli* after 30 mins). In contrast, poor labeling efficiency was observed for *E. coli* that had not been treated with the cationic surfactant (0 to a few CPNs per *E. coli* after 30 mins), likely due to repulsion between CPNs and the naturally negatively charged bacteria surfaces. The *E. coli* were imaged under 800W/cm$^2$ excitation, N$_2$ atmosphere using 10 Hz framerates. *E. coli* labeled with 20% or 40% PCBM doped PFBT CPNs exhibited pronounced blinking (Fig. 3.9 a). While the background autofluorescence from *E. coli* is typically dim as compared to the brightness of 20% and 40% PCBM doped PFBT CPNs (Fig. 3.8 b, d), background subtraction was performed to ensure optimal localization accuracy. The background fluorescence was determined from frames with no CPN switched "on". ~100 frames of the background fluorescence were averaged and subtracted from each frame
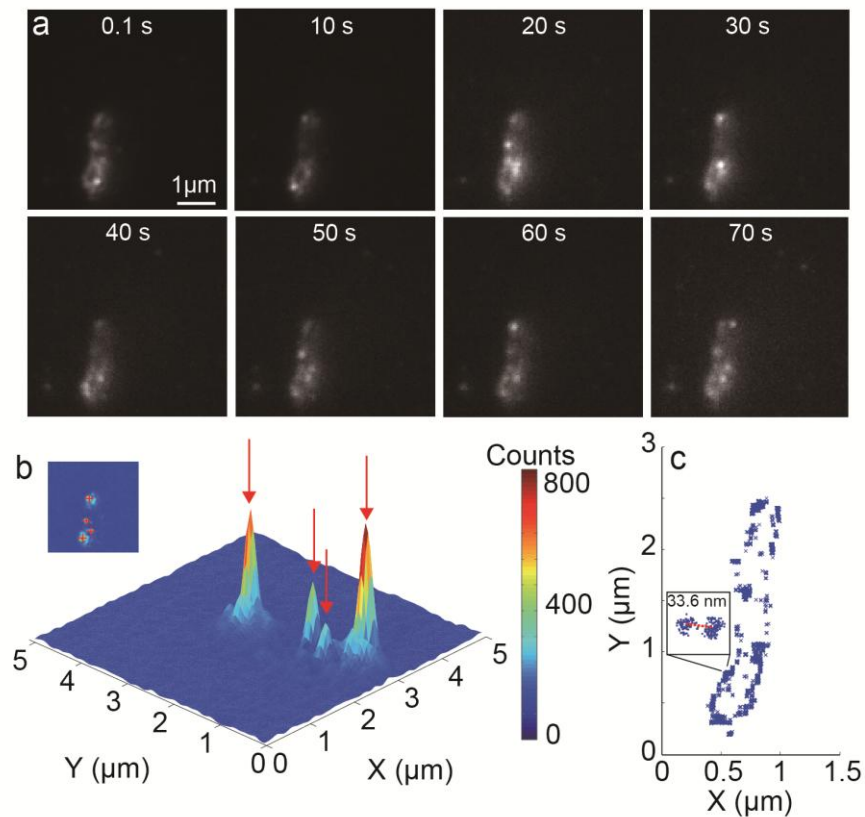
**Figure 3.9.** (a) A sequence of fluorescence microscopy images showing the blinking behavior of an *E. coli* labeled with 20% PCBM doped PFBT CPNs. (b) A 3D fluorescence intensity map shows a few switched "on" CPNs on an *E. coli*, which are indicated by the red arrows. The inserted plot shows a 2D view of the same image with localized positions of switched "on" CPNs indicated by red crosses. (c) A scatter plot shows the superresolution image of an *E. coli* constructed from the localized positions of blinking CPNs. The subplot shows the zoomed in view of two clusters in the scatter plot, indicating CPNs separated by ~30 nm are clearly resolved.

prior to analysis. The position of each CPN was determined using the single particle localization method (details given in chapter 2). The localized positions obtained from each frame were then used to reconstruct the shape of the *E. coli*, which is shown by the scatter plot in Fig. 3.9 c. Analysis of the scatter plot shows that features well below the diffraction limit were resolved. As shown in the Fig. 3.9 c subplot, the two clusters correspond to the localized positions of two nearby CPNs, which are clearly separated. The 33.6 nm distance between the centers of the clusters is highlighted with a red dashed line. These results suggest that nanoparticles separated by ~30 nm are readily resolved. From the standard deviation $(\sigma_x + \sigma_y)/2$ of the two clusters, we determined the per frame localization uncertainty of the two CPNs to be 5.95 nm (left) and 6.82 nm (right), which are consistent with the brightness of 20% PCBM doped PFTB CPNs under the imaging conditions.


## 3.7 Conclusions

In summary, we have developed a new class of fluorescent nanoparticles for superresolution imaging with significantly improved spatial resolution. PCBM doped PFBT CPNs establish large polaron populations inside the nanoparticles that nearly completely suppress the polymer fluorescence. However, the fluctuations in the number of charge carriers lead to occasional bursts of fluorescence. For 20% PCBM doped PFBT CPNs, we determined that around $3\text{-}5\times10^4$ photons were detected during the fluorescence burst, which results in a localization precision of ~0.6 nm, about 4 times better than the typical resolution obtained by localization of dye molecules. Since polaron generation is

a photo-driven process, we showed that the blinking duty cycle of PCBM doped PFBT CPNs can be controlled by excitation intensity as well as by PCBM fraction. Finally, we demonstrated superresolution microscopy of *E. coli* using 20% PCBM doped PFBT CPNs. At 10 Hz framerates, we obtained the precise shape of the bacteria with a localization precision of ~5 nm. These results suggest that PCBM doped PFBT CPNs represent a novel class of promising superresolution probes with unprecedented localization precision and tunable spontaneous photoswitching (blinking) properties, which provide clear advantages for imaging of various biological systems.

In modeling of the blinking behavior of PCBM doped PFBT CPNs, we observed that the polaron generation rate in CPNs only increases moderately with the excitation intensity. In contrast, the previous single molecular study and modeling of charge generation in CPNs/single polymer chains indicated a linear relationship between the polaron generation rate and the excitation intensity.[31] The discrepancy is likely due to the fact that PCBM doped PFBT CPNs are highly heterogeneous compared to CPNs consisting of just polymers, as indicated by the small stretch parameter β obtained from the KWW fitting of the picosecond time-resolved fluorescence decay traces. In different regions of a PCBM doped PFBT CPN (close to versus far away from PCBM/polymer interface), the charge generation rate is likely to vary substantially and respond differently to excitation intensity changes. In addition, it is likely that at the parts far away from the PCBM/polymer interface, excitons are funneled to the hole polarons via a dynamic quenching mechanism, whereas at the PCBM/polymer interface, static quenching may be involved. Overall, PCBM doped PFBT CPN is a complex system, the

parameters obtained from the kinetic model in this chapter are the averages of highly heterogeneous dynamics. The detailed relationships between doping level, excitation intensity, duty cycle, and various other aspects (fluorescence lifetime, etc) are still under investigation.

CHAPTER FOUR

NANOSCOPY OF SINGLE CHARGE CARRIER JUMPS IN A CONJUGATED
POLYMER NANOPARTICLE

## 4.1 Introduction

In recent years, there has been intense research interest in conjugated polymer based photovoltaic devices.[1, 2, 18] Conjugated polymers exhibit high absorption coefficient with tunable electronic band gaps, which make them promising materials for a variety of electro-optical applications.[10-12, 18, 29, 114] The good flexibility and processability of conjugated polymers make it easy and cost-effective to manufacture thin film solar cells.[3, 20, 34] However, the efficiency of organic solar cells is often limited by charge carrier mobility.[1, 21, 65] Due to disorder and chemical defects, charge transport in conjugated polymer systems is often characterized as dispersive, consistent with mostly trapped charge carriers and hopping transport.[21-23] Improving our understanding of the nature of dispersive charge transport is important to the continued development of conjugated polymer photovoltaic devices.

Obtaining a detailed picture of charge carrier motion in disordered semiconductor materials has been an ongoing challenge. ToF and I-V analysis are the common methods employed to characterize charge transport in semiconductors.[63, 115, 116] ToF and I-V analysis are ensemble measurements that average over large number of charge carriers. A broad range of carrier arrival times is commonly observed in ToF measurement of disordered materials. [63, 117, 118] The transport parameters of individual charge carriers can only be inferred indirectly through extensive modeling and simulation. In addition, there

are studies that use optical imaging methods.[119, 120] However, these methods lack the sensitivity and spatial resolution required to monitor the motion of a single charge carrier.

Recently, we reported that, under some conditions, CPNs fixed on a coverslip exhibit small fluctuations in the fluorescence centroid that likely result from hole polaron motion.[59] There is evidence that hole polarons act as highly efficient fluorescence quenchers with a quenching radius of several nm.[108, 121-123] For a conjugated polymer nanoparticle with a radius comparable to or several times larger than the quenching radius, under the proper conditions, a hole polaron can form a "dark spot" that moves with the polaron and results in the displacements in the fluorescence spot or centroid. These position fluctuations thus can be used to track nanometer-scale motion of hole polarons within the nanoparticle. Based on this phenomenon, we proposed a novel method for tracking individual polaron motion with nm resolution, which could provide an unprecedented level of detail about the motion of charge carriers in conjugated polymers. In principle, the residence time of single carriers in individual traps, and the distances and frequencies of hopping between various traps, i.e., the key parameters of the single carrier equations of motion, could be determined.

Charge transport in disordered materials typically spans over several time and length scales.[64, 65, 124] In our previous publication, we observed some single step hopping of polarons, however, there was also "rolling" behavior indicative of smaller fluctuations perhaps occurring too quickly to resolve with the 50 Hz framerate camera.[59] In this work, we combined fast polaron tracking (up to 1 kHz framerate) with single particle spectrum analysis. The improved temporal resolution and the additional analysis reveal several

interesting phenomena. Analysis of the fluorescence centroid position trajectories indicates a broader range of length scales and time scales than the previous results. Mean square displacement (MSD) analysis indicates anomalous diffusive motion occurring on several length scales and timescales, yielding diffusion coefficients spanning over three orders of magnitude, corresponding to zero-field polaron mobilities ranging from $10^{-10}$ $cm^2/Vs$ to $10^{-7}$ $cm^2/Vs$. Position autocorrelation analysis yields a complex exponential decay with time constants ranging from one millisecond to several seconds. These results qualitatively agree with the basic physical picture of multiple trap states with a range of energies and barrier heights reflected in a range of rates for polaron hopping between trap sites. By determining the spectra of the emission sites quenched by a hole polaron as it moves inside a CPN, we obtained a nanoscale map of local emission characteristics inside a CPN. It is found that nanoparticle of conjugated polymer PFBT exhibit a two-tier energy landscape for charge transport. Two dominate polymer chain conformations were observed, a glassy "blue" emitting phase ($\lambda_{max}$ ~550 nm)  and an ordered "red" emitting phase ($\lambda_{max}$ ~595 nm). We found that hole polarons are preferably generated and trapped within the red-emitting regions inside CPNs. In the centroid position histogram, we observed that the polaron spent most of the time at a few "red" emitting sites, which correspond to polaron trap sites. To obtain more detailed information about trap to trap variation and spatial distribution, we separated the position trajectories into segments of various durations. In some segments, repeated hopping between two red emitting trap sites can be observed. For those segments, we estimated polaron hopping times and distances from position autocorrelation time constants and MSD confinement lengths,

respectively. The hopping times range (mostly) from several ms to 1 s, following a power law distribution. The hopping distances range from 2-5 nm and were fit to an exponential distribution. From the polaron hopping time constant distribution, we estimated the energy barrier heights for polaron hopping in CPNs based on the Arrhenius equation. The barrier height determined ranges from 430 to 570 meV, which is on the larger side of activation energies reported for polymer films,[9, 22, 23] likely indicating the presence of deep traps with nearest-neighbor distances of 2-5 nm, consistent with a low or moderate density of chemical or structural defects.

**4.2 Polaron Tracking Method and Single Particle Spectrum Measurement**

Nanoparticles of conjugated polymer PFBT with diameters of 16.2 ± 4.8 nm were prepared and characterized as described previously.[10] The particles were dispersed on a glass coverslip and imaged with an inverted fluorescence microscope. Under 100 W/cm$^2$ excitation power, 1-7 $\times 10^3$ photons were detected per particle per 1 ms exposure. We determined the fluorescence centroid positions of the CPNs by least-squares fitting of a Gaussian function to the fluorescence spot. Based on the width of fluorescent spot and number of photons detected per frame, typical expected localization uncertainty per frame, at 1 kHz is around 1.6-3.8 nm (the determination procedure is given in chapter 2). To perform single particle localization and spectra measurement simultaneously, a transmission grating was used to disperse the single particle fluorescence. The disperse fluorescence formed long stripes at the first order fluorescence spot. Each long stripe was
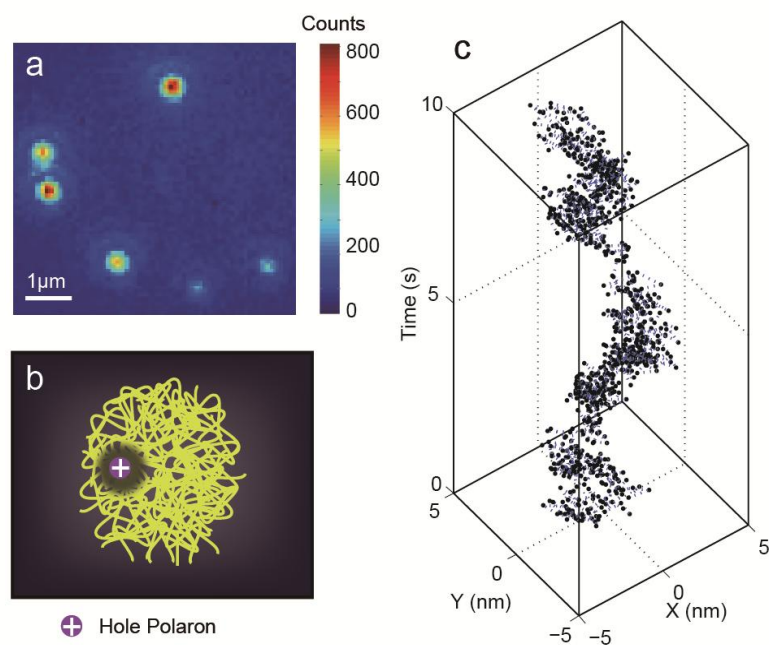
**Figure 4.1.** (a) A typical fluorescence microscopy image of PFBT CPNs; (b) Illustration of a hole polaron quenching the local fluorescence in a CPN; (c) A trajectory of the X and Y centroid position of a CPN, acquired at 1 kHz framerate. For plotting, every 10 frames were binned together to reduce noise.

summed along the Y axis (10 pixels in total) to obtain the emission spectra of individual particles, as discussed in the chapter 2. With the grating, due to less photons employed for localization, the tracking uncertainty per frame increased to 7.7-15 nm, which was reduced to 1-3 nm through binning. The centroid trajectory shows distinct fluctuations above noise (Fig. 4.1 c). As discussed above, it is likely that a hole polaron effectively quenches luminescence of nearby chromophores and results in a dark spot in the nanoparticle,[125, 107] and as the polaron moves inside the particle, the fluorescence centroid of the particle will also be displaced (Fig. 4.1 b).[59] These position fluctuations thus serve as a measure of the nanometer-scale motion of hole polarons within the nanoparticle. The position of the hole polaron can be estimated from the displacement of fluorescent centroid using the relationship we previously determined from exciton diffusion and energy transfer simulations of CPNs, [59]

$$\delta x_f \approx -x_p Q_p, \tag{4.1}$$

where $\delta x_f$ is the displacement of the fluorescent centroid caused by polaron, $x_p$ is the position of the polaron relative to the center of the particle, and $Q_p$ is the quenching efficiency of a single polaron, which is estimated from the fluorescence intensity trajectories of CPNs (details shown below).

## 4.3 Characterization of Polaron Generation and Recombination Dynamics

The polaron generation and recombination dynamics in CPNs were characterized by the fluorescence intensity fluctuations. It was previously reported that generation and recombination of a single hole polaron in a conjugated polymer chain result in abrupt

fluorescence intensity jumps, "on" and "off" rates of the intensity fluctuations indicate polaron recombination and generation rates, respectively.[31, 32] The fluorescence intensity fluctuations of CPNs are more complex than in single chains, sometimes involving multiple polarons. In some fluorescence intensity trajectories, we observed fast initial decays within the first 5-20 s, which are likely caused by the growth of the polaron population from 0 to a steady state value around 2-5 (modeling of this phenomenon is given in later sections).[12] We selectively studied CPNs with minimal fast initial intensity decay (<10 %) so that typically a single polaron or none is presented in the particle during the experiment (Fig. 4.2 a).

The fluorescence intensity trajectories of CPNs were analyzed with autocorrelation. The intensity autocorrelation typically fits poorly to a single exponential decay while it shows a good fit to a bi-exponential function (Fig. 4.2 c), indicating heterogeneous dynamics. Table 4.1 shows the time constants resulting from the bi-exponential fits to the autocorrelation of the intensity trajectories acquired at three different excitation intensities, 50 Hz framerates. The smaller time constants show no dependence on excitation intensity while the time constants > 1 s show a decreasing trend. It is likely that the slower intensity fluctuations are primarily caused by polaron generation and recombination dynamics and the low-amplitude sub-second scale fluctuations are primarily due to non-photo-driven processes such as polaron diffusion. The "on" and "off" durations of two-state blinking trajectories were determined via change point analysis described as follows. Haar wavelet transform was used to detect abrupt intensity changes above small, fast fluctuations. Local maxima in the Haar wavelet transform
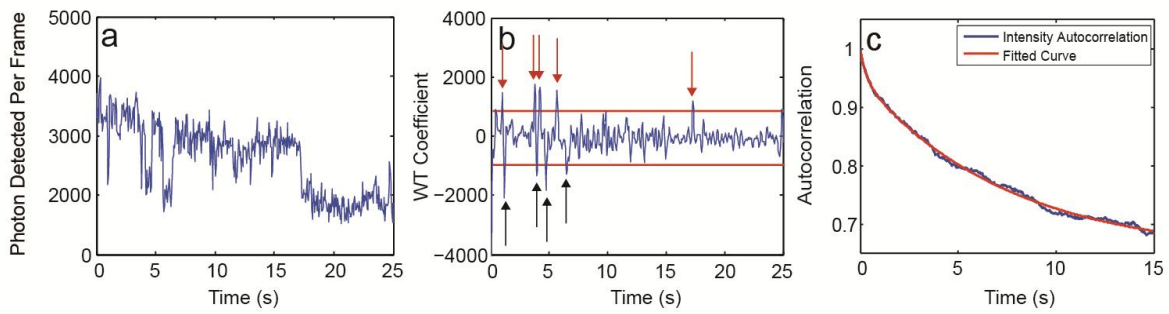
**Figure 4.2.** (a) An intensity trajectory segment showing two-level fluctuations. (b) The corresponding wavelet transform coefficients of the segment (scale:8). The "on" and "off" transitions were indicated by black and red arrows respectively. The threshold (red lines) was calculated from median absolute deviation of the wavelet transform coefficients at scale 2. (c) The autocorrelation curve of the full intensity trajectory with fit to the bi-exponential decay formula ($y = A_1 e^{-x/\tau_1} + A_2 e^{-x/\tau_2} + y_0$). $\tau_1$= 0.31 s, $\tau_2$=5.40 s.

**Table 4.1.** Time constants $\tau_1$ and $\tau_2$ from the intensity autocorrelation analysis. $\tau_{on}$ and $\tau_{off}$ from change point analysis of the intensity trajectories of CPNs

|  | 50W/cm$^2$ | 100W/cm$^2$ | 200W/cm$^2$ |
|---|---|---|---|
| $\tau_1$ | $3.66 \pm 1.71s$ | $2.72 \pm 1.50s$ | $2.03 \pm 0.95s$ |
| $\tau_2$ | $0.57 \pm 0.24s$ | $0.54 \pm 0.21s$ | $0.48 \pm 0.26s$ |
| $\tau_{on}$ | $10.7 \pm 2.13s$ | $5.0 \pm 1.76s$ | $3.3 \pm 1.29s$ |
| $\tau_{off}$ | $6.7 \pm 1.52s$ | $6.8 \pm 1.67s$ | $5.7 \pm 1.33s$ |

(WT) coefficients indicate transitions between the "on" and the "off" states. Since WT coefficients at small scales are dominated by noise, the median absolute deviation of the WT coefficients at scale 2 was used as a threshold to differentiate real transitions from noise. As we gradually increase the scale, the blinking events can be separated from noise, indicated by peaks above the threshold in the WT coefficients (Fig. 4.2 b). The positive and the negative peaks indicate polaron recombination and generation events respectively. Once the transition events were located, we can determine the durations of each individual "on" and "off" event. In the end, the average "on" and "off" durations determined from the change point analysis were compared to the corresponding autocorrelation time constant to ensure consistency $(1/\tau_{ac} = 1/\tau_{on} + 1/\tau_{off})$. $\tau_{on}$ and $\tau_{off}$ from the analysis are summarized in table 4.1. It is observed that $\tau_{on}$ decreases with the increase of the excitation intensity while $\tau_{off}$ is independent, which is expected since the polaron generation process is photo-driven while the recombination process is pseudo-first-order. [31]

In the single particle spectra, we observed changes highly correlated with the blinking events that PFBT CPNs typically exhibit "red" emission ($\lambda_{max}$~595 nm) during the "on" state while show "blue" emission ($\lambda_{max}$ ~550 nm) during the "off" state. (Fig. 4.3) By subtracting the "off" spectrum from the adjacent "on" state spectrum, we obtain the spectrum of the emission sites that the hole polaron was generated on. The "quenched" spectra are typically sharp and red-shifted (Fig. 4.3 d). According to the previous discussion, due to tetrahedral defects, conjugated polymer chains tend to folded into an ordered cylindrical conformation, which is known to be associated with generation of
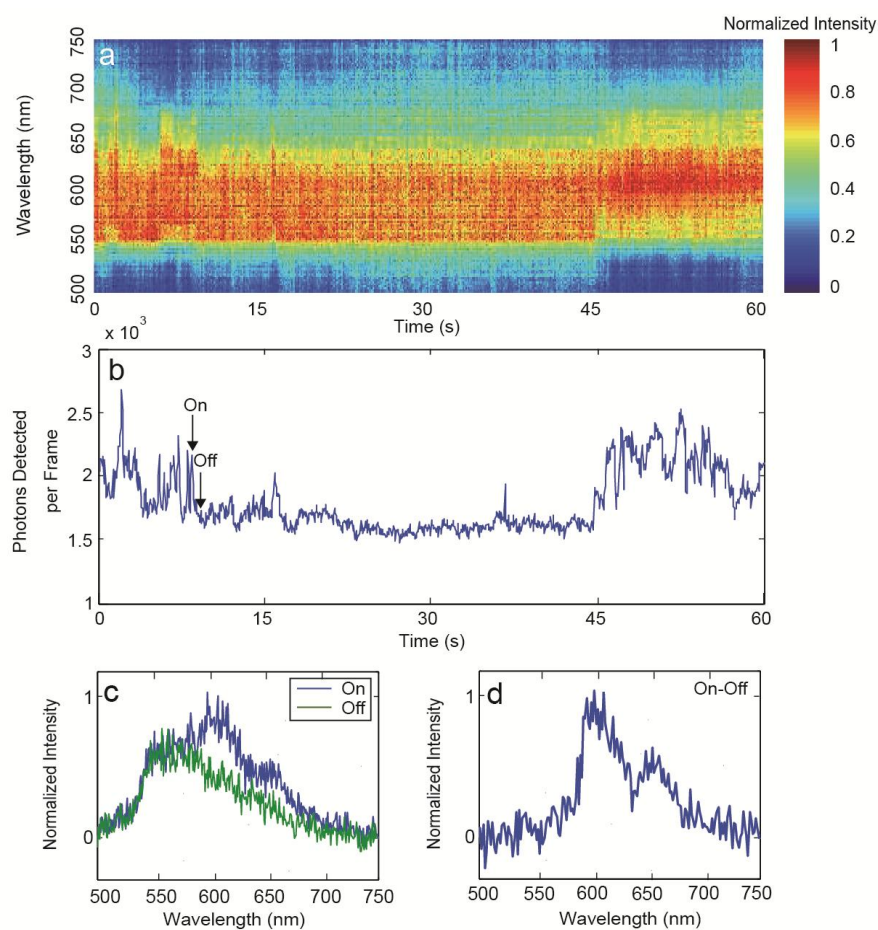
**Figure 4.3.** (a) Stacked single particle fluorescence spectra of a CPN showing changes over time. The shifts in the spectra can be correlated with blinking events in the corresponding fluorescence intensity trajectory shown in plot (b). (b) The corresponding fluorescence intensity trajectory. (c)(d)The spectra of (c) two adjacent "on" and "off" states, (d) "on"-"off" state of the CPN.

hole polarons.[32, 39] Excitons generated within the area can efficiently migrate to the lowest energy sites, which results in the narrow and red-shifted emission spectra.

Overall, these results indicate a small polaron population presented in the particle during the experiment, typically a single polaron or none. We determined that the polaron generation and recombination dynamics in CPNs are on the timescale of several seconds and thus should not significantly affect the measurement of fast polaron hopping dynamics.

## 4.4 Determination of Quenching Efficiency of Single Hole Polaron

It was previously reported that generation and recombination of a single hole polaron in a conjugated polymer chain result in abrupt fluorescence intensity jumps.[31] From the quenching depth, it is estimated that a single hole polaron can quench up to 90% of the single polymer chain fluorescence.[31, 121] In CPNs, due to the larger number of chromophore units (i.e., the larger system size), the quenching efficiency of a single polaron is typically much lower.[59] However, stepwise blinking behavior can still be observed with some CPNs (typically relatively dim ones). For these CPNs, histograms constructed from the fluorescence intensities of each frame typically show clustering indicating a few distinguishable states (Fig. 4.4 d). $Q_p$ ranging from 10% to 30% were determined from the fluorescence intensity histogram. For bright CPNs, $Q_p$ is typically small (Fig. 4.4 a) that the fluorescence intensity histograms do not clearly show different states (Fig. 4.4 b). $Q_p$ of these nanoparticles were estimated from the STD of the intensity fluctuations, typically ranging from 3%-10%.
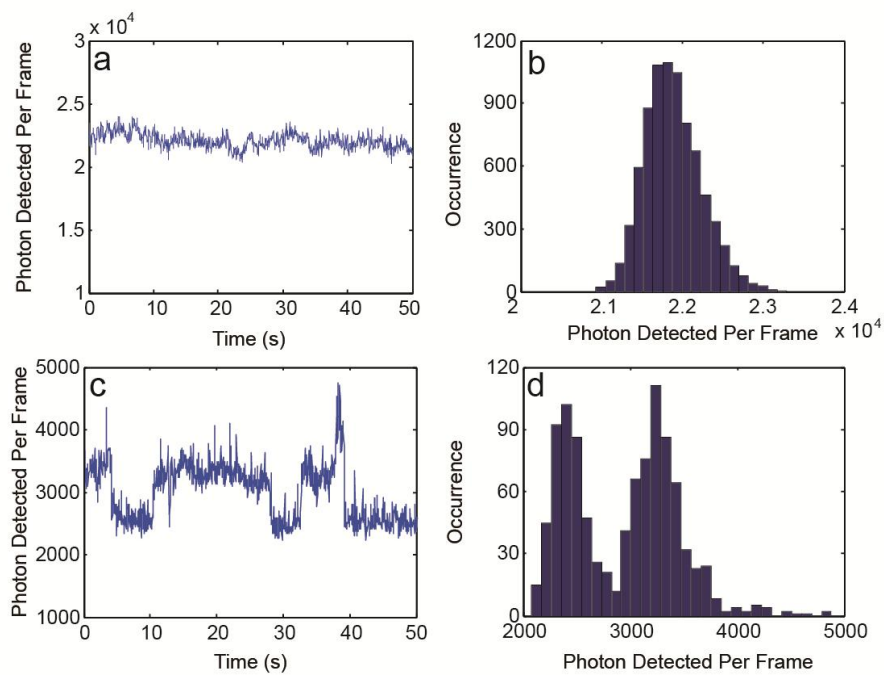
**Figure 4.4.** (a) The intensity trajectory and (b) the corresponding intensity histogram of a bright CPN; (c) The intensity trajectory and (d) the corresponding intensity histogram of a dim CPN.

## 4.5 Characterization of the Initial Fluorescence Decay

Sometimes, at higher excitation intensities, a rapid fluorescence intensity decay within the first 10-20 s can be observed with CPNs (Fig. 4.5 a), which has been previously attributed to the growth of the polaron population from 0 to a steady state value.[12] We monitored the spectra change during the fluorescence intensity decay process. We observed that, as the fluorescence intensity approaching equilibrium, the "red" emission in CPNs were selectively quenched (Fig. 4.5 b, c, d), indicating that the red-emitting sites were occupied by hole polarons. Based on this phenomenon, we determined the number of red-emitting sites per CPN from the number of steps in the initial fluorescence decay. We found that the number of red-emitting sites per CPN follows a Poisson distribution with $\lambda = 3$, indicating there are typically three red-emitting sites per nanoparticle.

In order to obtain addition information about the timescales of the polaron generation and recombination dynamics in CPNs, we modeled the initial intensity decay with a set of rate equations,

$$\frac{dn_{ex}}{dt} = k_{abs} - k_f n_{ex} - k_q n_{ex} n_p - k_{diss} n_{ex} + k_{rec} n_p, \tag{4.2}$$

$$\frac{dn_p}{dt} = k_{diss} n_{ex} - k_{rec} n_p. \tag{4.3}$$

The equation 4.2 and 4.3 describe exciton and polaron kinetics, respectively, $n_{ex}$ and $n_p$ are the numbers of excitons and polarons per nanoparticle, $k_{abs}$ is the photon absorption rate constant, $k_f$ is the rate constant of radiative and non-radiative relaxation, $k_q$ is the rate constant of exciton quenching by polaron, $k_{diss}$ is the rate constant of exciton
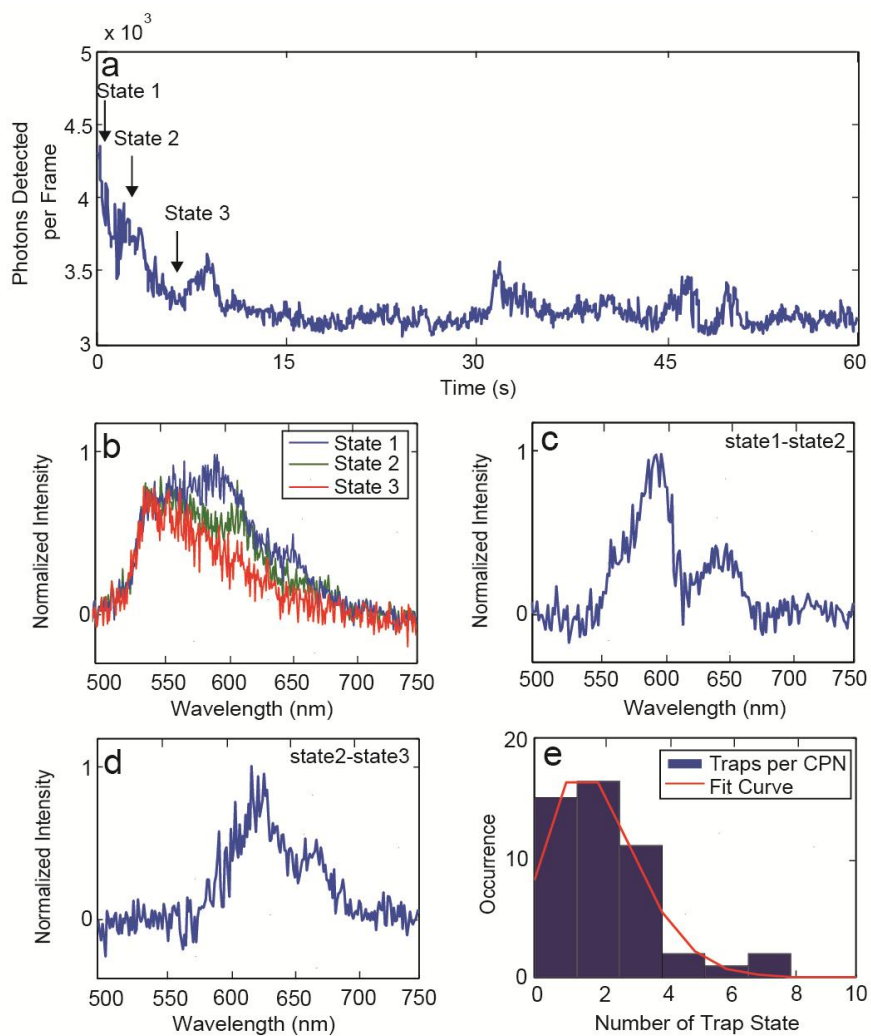
**Figure 4.5.** (a) A fluorescence intensity trajectory showing stepwise decay at early time. (b) The single particle fluorescence spectra at different states of the decay. (c) The "state1"-"state2" spectrum. (d) The "state2"-"state3" spectrum. (e) The distribution of number of red-emitting sites/charge carrier traps per CPNs, fit to a Poisson distribution with λ=3.

dissociation to form polarons and $k_{rec}$ is the recombination rate constant for polarons. The solutions to the above equations are complex expressions, making them difficult to use in data modeling or fitting. A possible simplification is to assume that a large portion of polarons are directly generated by photoexcitation so that polaron generation rate is proportional to excitation power. Then the polaron kinetics equation can be re-written as:

$$\frac{dn_p}{dt} = k_{abs}\phi - k_{rec}n_p,$$ (4.4)

where $\phi$ is the polaron generation quantum yield.

As discussed previously,[12] solving the equation 4.2 and 4.4 gives the analytical solution of the initial fluorescence decay process:

$$n_{ex}(t) = \frac{1}{\dfrac{k_f}{k_{abs}} + \dfrac{k_q\emptyset}{k_{rec}} - \dfrac{k_q\emptyset}{k_{rec}}e^{-k_{rec}t}}.$$ (4.5)

According to the equation 4.5, we fit the decay part of the intensity trajectories to function $f(t) = 1/(A + Be^{-k_{rec}t})$. As shown in Fig. 4.6, a polaron recombination rate constant of 0.17 s$^{-1}$ was obtained from the fitting, which is consistent with $\tau_{off}$ determined from the blinking analysis.

### 4.6 Fluorescence Centroid Position Trajectory Analysis

The fluorescence centroid trajectories obtained at 1 kHz were analyzed by autocorrelation and MSD. Results for a representative trajectory are shown in Fig. 4.7. While the results for lag times of ~100 ms or higher are similar to those obtained at 50 Hz framerates that we reported previously,[59] at shorter lag times, additional dynamics are evident. As shown in Fig. 4.7 a, the position autocorrelation fits to a bi- exponential
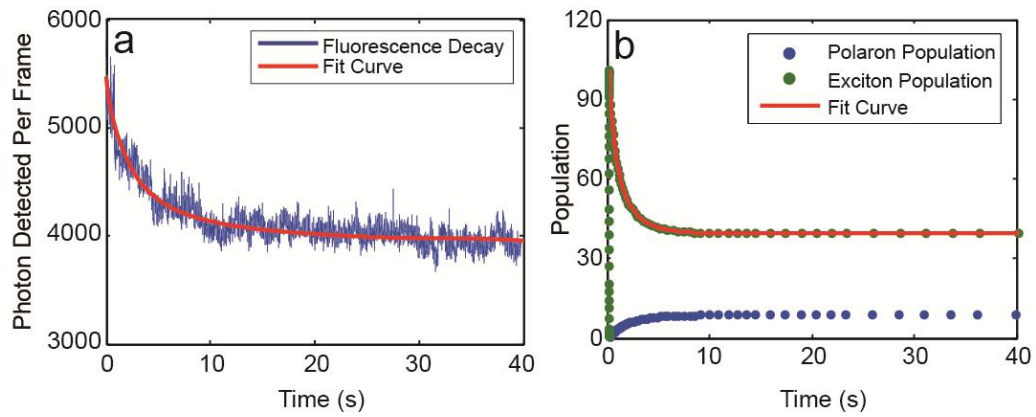
**Figure 4.6.** (a) An intensity trajectory showing initial intensity decay with fit to $f(t) = 1/(A + Be^{-k_{rec}t})$, $k_{rec} = 0.17s^{-1}$; (b) Polaron population growth (blue) and exciton population decay (green) simulated from the equations 4.2 and 4.4. The exciton population decay was fit to the equation 4.5.

or stretched-exponential (KWW) function. In a 4 s (lag) time window, typical time constant and $\beta$ value obtained from the KWW fitting were 1.9 s and 0.65, respectively. An average time constant $\langle\tau\rangle$ of 2.6 s was obtained from the zero order moment of the KWW fit function $\langle\tau\rangle = \tau_{kww}\,\beta^{-1}\Gamma(\beta^{-1})$. As is often the case for complex dynamics spanning multiple timescales, the time constants obtained from fitting the autocorrelation were found to depend on the time window or range used in the fitting procedure. When the time window is set to the first 15 ms, the early autocorrelation decay can be fit to a single exponential function to yield a time constant $\tau_{early} = 3.0$ ms for the example trajectory autocorrelation (Fig. 4.7 c). The tail part (lag time 2-4 s) of the autocorrelation can also be fit to a single exponential function with a time constant of $\tau_{late} = 3.2$ s. $\tau_{early}$ and $\tau_{late}$ roughly indicate the lower and upper limit of the dynamics timescales, which span over three orders of magnitude. Similar complex dynamics were also observed for the MSD of the position trajectories. The MSD shows a steep increase within the first tens of milliseconds (Fig. 4.7 b) and does not yield a good fit for a single diffusion constant. If we discard the early part, the tail MSD can be fit to a confined diffusion function $\langle x_f^2(t)\rangle = \langle x_f^2(0)\rangle + L_f^2\{1 - \exp(-2D_f t/L_f^2)\}$ and yield parameters similar to values obtained at 50Hz framerates. When the time window is set to the first 15 ms, the early MSD can also be fit to a confined diffusion function (Fig. 4.7 d). The diffusion coefficient $D_f$ and the confinement length $L_f$ of fluorescence centroid obtained from the fitting were used to calculate the diffusion coefficient $D_p$ and the confinement length $L_p$ of polaron using the expressions $D_p = D_f/Q_p^2$, $L_p = L_f/Q_p$,[59] where $Q_p$ is the quenching efficiency of a single polaron (expressions are obtained by applying Eq. (4.1)).
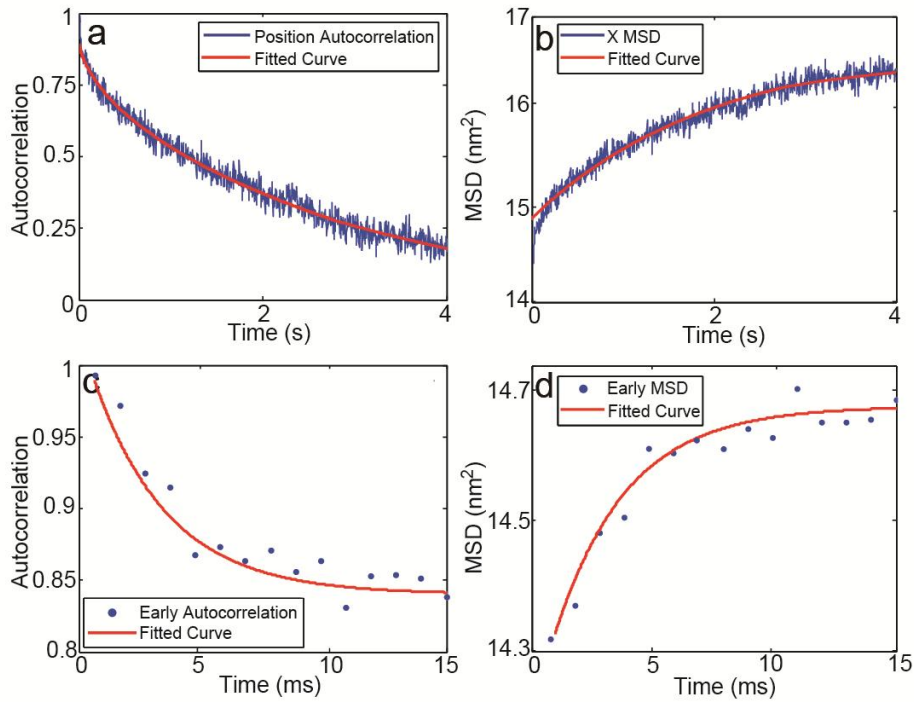
**Figure 4.7.** The position autocorrelation and MSD of a single particle fluorescence centroid trajectory (1 ms dwell). (a) The X position autocorrelation (0-4 s) with fit to a KWW function, $\tau_{kww}$ = 1.90 s, $\beta$ = 0.65. (b) The X MSD (0-4 s) with fit to a confined diffusion function, $D_f$ = 0.5 nm$^2$/s, $L_f$ = 1.3 nm. (c) The X position autocorrelation (0-15 ms) fit to a single-exponential function, $\tau = 3$ ms. (d) The X MSD (0-15 ms) fit to a confined diffusion function, $D_f$ = 87 nm$^2$/s, $L_f$ = 0.58 nm.

Using $Q_p = 0.15$ determined from the corresponding intensity trajectory, a polaron confinement length of 3.8 nm and zero field polaron mobilities of $1.5 \times 10^{-8}$ cm$^2$/Vs were obtained from the early part of the MSD. The polaron mobilities determined are one or two orders of magnitude higher than what we have previously reported and similar to the values obtained by I-V analysis of the corresponding polymer films,[126, 127] which suggests that the small single polaron mobilities we reported previously are likely an underestimate caused by a combined effect of the multiple time scales involved in carrier transport and the limited temporal resolution previously employed. The broad range of polaron mobilities and confinement lengths determined agree with the basic physical picture of dispersive charge transport, i.e., that there are multiple trap states with a range of barrier heights and distances for polaron hopping from trap to trap, which will be explored in more detail below.

## 4.7 Nanoscale Mapping of Energy Landscape for Charge Transport

In long trajectories, hole polaron can explore large areas inside a CPN. Changes in the single particle spectra can be observed over time as different area of the CPN is quenched by the hole polaron, which enable us to obtain a nanoscale map of local emission characteristics inside a CPN. To perform this kind of analysis, we picked CPNs that showed clear two-level blinking behavior with long polaron lifetime. The spectrum of each frame during the intensity "off" state was subtracted from the spectrum of the adjacent intensity "on" state to obtain the spectrum of the emission sites that were quenched by the hole polaron, as polaron moves inside a CPN. The trajectories of polaron
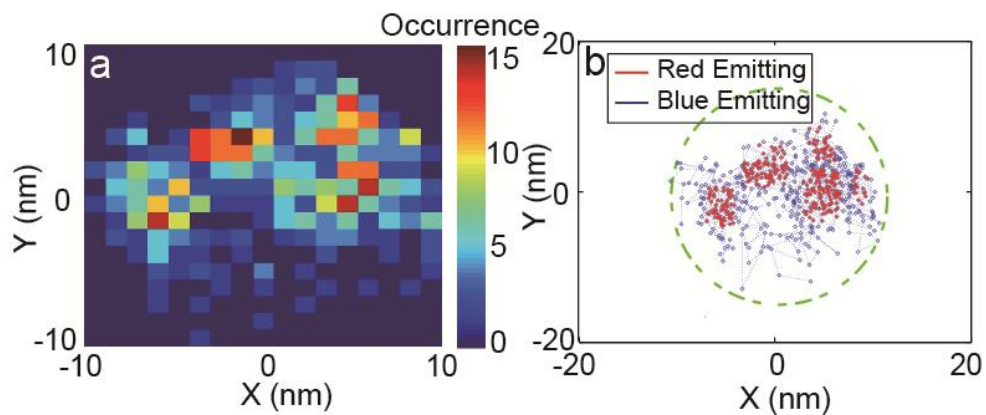
**Figure 4.8.** (a) The position histogram constructed from the trajectories of polaron motion during the intensity "off" states of a CPN. (b) The corresponding 2D polaron position plot. The red and blue lines indicate that the area exhibit "red" and "blue" emission, respectively. The green dashed lines indicate the boundary of a CPN with 20 nm diameter.

motion during the intensity "off" states of a CPN were used to construct a position histogram. As shown in Fig. 4.8, a two-tier energy landscape for charge transport can be clearly observed from the 2D polaron position histogram. The red and blue lines indicate that the area exhibit "red" and "blue" emission, respectively. The position histogram shows that the hole polaron spends most of the time within the "red" emitting areas of the CPNs (Fig. 4.8 a), likely indicating that the ordered "red" phase act as charge carrier traps. It is likely that "blue" phase is glassy that the emission comes from large numbers of localized sites, which leads to featureless, high energy emission spectra.[38] In such a heterogeneous system, it is statistically favorable for charge carriers at the order/disorder interface to hop back to the ordered (red-emitting) areas. In addition, previous researches indicated that polarons in crystalline domains are stabilized by $\pi$-stacking interactions, thus process lower energies than polarons in glassy regions.[128, 129]

## 4.8 Segmented Position Trajectory Analysis

In order to investigate possible dynamic heterogeneity and examine how the position trajectories varied over time, we divided the trajectories into segments. When the segment duration is long, for example, 20-40 s, the autocorrelation and MSD of each segment are similar to those of the full trajectory--the autocorrelation fits well to KWW or bi-exponential function, and the MSD fits to confined diffusion function with deviation at early time. When the segment duration is short, for example, 4-10 s, we observed different kinds of behavior in different segments. The first type is rapid, confined diffusion, which is most commonly seen. The position segment shows
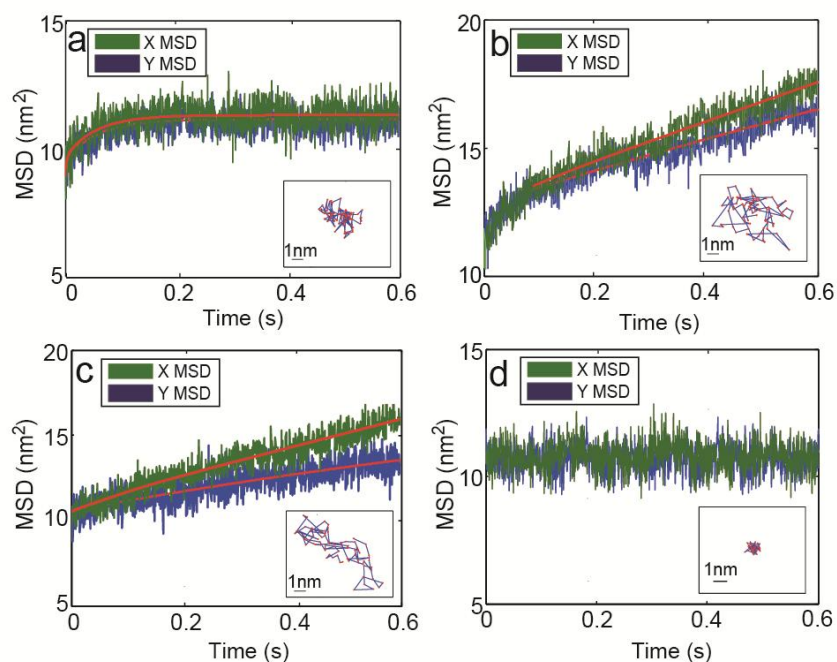
**Figure 4.9.** Representative segments of a 1 kHz framerate centroid position trajectories showing different types of behavior. (a) X (green) and Y (blue) MSD of a 10 s segment showing confined diffusion behavior (fit curves shown in red), $D_{fx} = 28.5 \text{ nm}^2/s$, $L_{fx} = 1.1 \text{ nm}$, $D_{fy} = 21.6 \text{ nm}^2/s$, $L_{fy} = 1.0 \text{ nm}$. 2D trajectory of the segment is shown in subplot, bin size = 32 frames; (b) X (green) and Y (blue) MSD of a 10 s segment showing mixed behavior. The tail part (0.3-1.2 s) was fit to free diffusion function (red), $D_{fx} = 4.2 \text{ nm}^2/s$, $D_{fy} = 3.0 \text{ nm}^2/s$. 2D trajectory of the segment is shown in subplot, bin size = 32 frames; (c) X (green) and Y (blue) MSD of a 10 s segment showing free diffusion behavior (fit lines shown in red), $D_{fx} = 5.2 \, nm^2/s$, $D_{fy} = 3.0 nm^2/s$, 2D trajectory of the segment is shown in subplot, bin size = 32 frames; (d) X (green) and Y (blue) MSD of a 10 s segment showing flat MSD. 2D trajectory of the segments is shown in subplot, bin size = 32 frames.

fluctuations confined to a small area. The MSD of the segment increases at early time then flattens within ~100 ms (Fig. 4.9 a). The second type is slower free diffusion, indicated by the MSD increasing almost linearly over several hundred ms (Fig. 4.9 c). Polaron mobilities ranging from $10^{-10}$ cm$^2$/Vs to $10^{-9}$ cm$^2$/Vs were obtained from a linear fit of the MSD, which are within the range of the polaron mobilities discussed above. In some segments, the first two types of behavior are mixed in that the polaron exhibits rapid motion for the first ~100 ms, followed by slower free Brownian motion for several hundred ms (Fig. 4.9 b). The fourth type of segment shows flat position autocorrelation and MSD, likely indicating there was no polaron present in the particle at the time (Fig. 4.9 d). The segments with flat position autocorrelation and MSD typically coincide with the "on" (higher intensity) state in the intensity trajectories.

We analyzed the position trajectory segments with confined diffusion-like behavior using the following method. The position autocorrelation was first fit to a bi-exponential function $y = A_1 e^{-x/\tau_1} + A_2 e^{-x/\tau_2}$ in a broad time window to yield an averaged time constant $\tau_0 = A_1 * \tau_1 + A_2 * \tau_2$. Then the autocorrelation from lag time 0 to $0.5*\tau_0$ was fit to a single exponential to yield a time constant $\tau_{early}$, the autocorrelation from $\tau_0$ to $2*\tau_0$ was fit to a single exponential to yield a time constant $\tau_{late}$. Using similar time windows, we can obtain $L_{early}$ and $L_{late}$ by fitting different part of the MSD to confined diffusion functions. Histograms were constructed from the $\tau_{early}$ and $\tau_{late}$, $L_{early}$ and $L_{late}$ values obtained from analysis of all the segments. While in a particular segment, the X, Y autocorrelation and MSD might behave differently from one another and yield different fitting parameters depending on how the polaron moves along each axis during

111

a given time segment, the fitting parameter histograms constructed from the X and Y segments were similar. $\tau_{early}$ and $\tau_{late}$, $L_{early}$ and $L_{late}$ determined from dozens of 20 s segments are shown in Fig. 4.10 c and 4.10 e, the histograms show well separated distributions, $\tau_{early}$ is typically less than 0.2 s while $\tau_{late}$ is in the range of 0.7-2 s, $L_{early}$ typically ranges from 0.5-1.4 nm, while $L_{late}$ ranges from 1.5-2.5 nm. These observations indicate dynamic heterogeneity likely due to segment-to-segment variability in terms of which trap sites (and corresponding trap-to-trap hopping rates) were involved. When the segment duration is reduced to 4 s, $\tau_{early}$ and $\tau_{late}$ obtained from the same segment become closer in value (Fig. 4.10 d) as compared to the results obtained for 20 s segments (Fig. 4.10 c), and similar behavior is also observed for $L_{early}$ and $L_{late}$, indicating that the underlying dynamics become less heterogeneous as the segment duration is reduced. This is consistent with a picture in which apparent heterogeneity is reduced at shorter timescales because a smaller region is explored by the polaron.

In some segments, $\tau_{early}$ and $\tau_{late}$ show almost no difference, i.e. the position autocorrelation fits well to a single exponential decay. For these segments, if the autocorrelation time constant is relatively large so that we can use binning to reduce position uncertainty, repeated hopping between two trap sites can be tentatively observed in the position histogram (Fig. 4.10 b). For the two-state hopping dynamics, the autocorrelation time constant $\tau_{ac}$ and 2D confinement length $L_{f2D}^2 = L_{fx}^2 + L_{fy}^2$ can be used to estimate polaron hopping time and distance,

$$\tau_{ac} = \frac{\tau_1 \tau_2}{\tau_1 + \tau_2} = \frac{\tau_2}{1 + K_{eq}}, \tag{4.6}$$

$$L_{f2D} = \frac{\sqrt{2\tau_1\tau_2}}{\tau_1+\tau_2} L_{hop}Q_p = \frac{\sqrt{2K_{eq}}}{1+K_{eq}} L_{hop}Q_p, \tag{4.7}$$

where $\tau_1$ and $\tau_2$ are the forward and backward hopping time constants, respectively, $K_{eq} = \tau_2/\tau_1$ is the equilibrium constant, which can be roughly estimated from peak height ratio in the position histogram. The hopping distances calculated from the MSD confinement lengths were compared with the position histogram to ensure consistency. For segments with small autocorrelation time constants and relatively high noise level such that $K_{eq}$ can't be extracted from the position histogram, $K_{eq} = 1$ was used (rationale discussed in later sections). Dozens of trajectories were analyzed using the method discussed above, and all of the segments that showed single exponential decay in the position autocorrelation were summarized to construct the hopping time and distance histograms (to check the validity of the analysis approach, the same analysis approach was applied to stochastic hopping simulations, described in later sections). The hopping time distribution can be roughly fit to a power law function $y = Ax^{-k}$ (Fig. 4.10 g), which is consistent with the power law waiting time distribution often featured in models of charge transport in disordered materials.[64, 130, 131] $k = 1.1$ was obtained from the fitting, which indicates a long tail in the hopping time distribution.[130, 131] It should be noted that the fitting result here is only approximate as we only resolved time constants over three orders of magnitude. A broader range of time constants is required in order to obtain a more reliable power law fit. The hopping distance histogram fits to a single exponential distribution $y = Ae^{-x/D}$ (Fig. 4.10 h), which shows that the hopping probability decays over distance. $D$ of 0.9 nm was obtained from the fitting. Due to
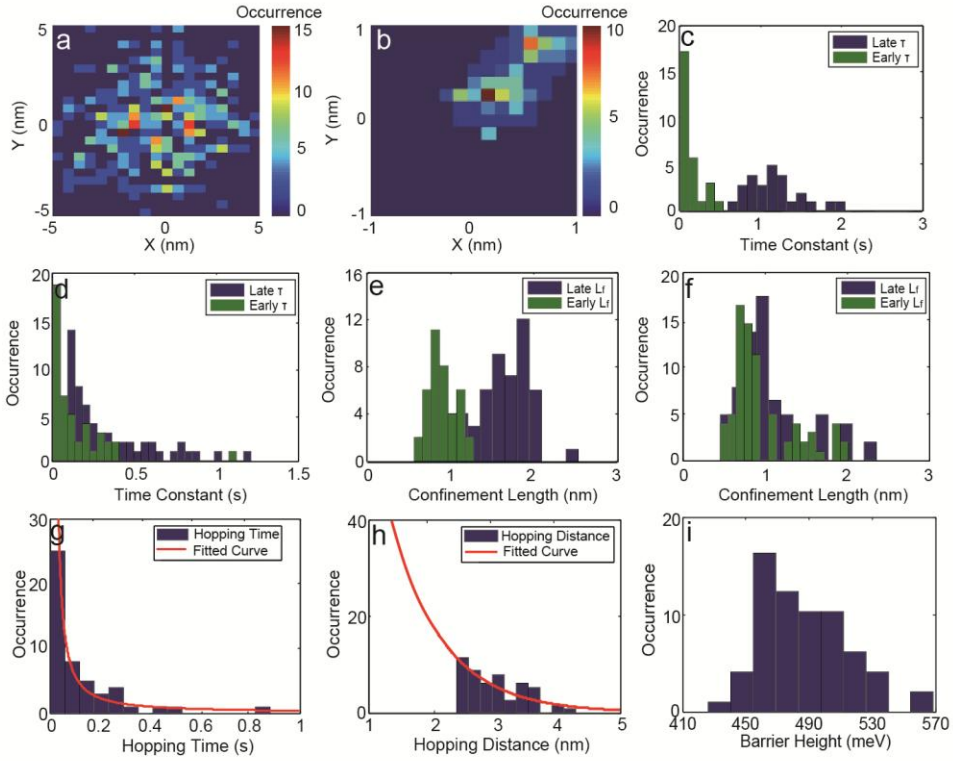
**Figure 4.10.** (a)(b) The centroid position histogram of a 40 s segment (a) and a 4 s segment (b), (bin size = 32 frames); (c)(d) Histograms of time constants $\tau_{early}$ and $\tau_{late}$ obtained from analysis of 20 s segments (c) and 4 s segments (d); (e)(f) Histograms of confinement lengths $L_{early}$ and $L_{late}$ obtained from analysis of 20 s segments (e) and 4 s segments (f); (g) The polaron hopping time constant distribution fit to a power law function $y = Ax^{-k}$, $k = 1.1$; (h) The hopping distance distribution fit to a single exponential function $y = Ae^{-x/D}$, $D = 0.9$ (i) The barrier height distribution with peak values around 460 meV.

114

limited spatial and temporal resolution, we have only resolved long range charge transport happening above the ms timescale (we did not take into account the possibility that motion within the traps could contribute to the measured carrier motion--while such motion could occur, it would likely occur on shorter time and length scales that cannot be resolved by the current experiment). Based on the hopping time constants determined, we used an Arrhenius type hopping equation to estimate polaron hopping barrier heights in CPNs,

$$v_{ij} = v_0 e^{-\frac{\Delta E_{ij}}{kT}}, \tag{4.8}$$

where $v_{ij}$ is the hopping rate, $\Delta E_{ij}$ is the energy barrier height, $v_0$ is the attempt rate, which is defined as the fastest hopping rate. In a disordered system, $v_0$ is determined by the inter-molecular coupling between the adjacent traps. In temperature dependent ToF studies, $v_0$ can be roughly estimated by extrapolating carrier mobilities to infinite temperature.[65] Typical $v_0$ values reported for conjugated polymer films range from $10^{10}$ s$^{-1}$ to $10^{11}$ s$^{-1}$.[64, 65] When $T$ is set to 298 K and $v_0$ is set to $10^{10}$ s$^{-1}$, the energy barrier heights determined from the equation 4.8 range from 430 meV to 570 meV with peak values around 460 meV. Both polaron binding energy and trap depth contribute to the barrier height estimated. Since ToF studies and modeling of electron-phonon interaction in various polymer films typically yield polaron binding energy of 60-180 meV,[132, 133] we attribute most of the barrier height to energetic disorder in CPNs. The activation energy we obtained is similar to the activation energy associated with energetic disorder reported for disordered polymer films.[9, 22, 23]

**Figure 4.11.** (a) Scheme showing the detail of a two-state hopping simulation. The trap positions are shown by the black dots and the hopping path are shown by the red line. (b)(c)(d) The X position autocorrelation of simulated two-state hopping trajectories, with (b) $K_{eq} = 1$, (c) $K_{eq} = 3$, (d) $K_{eq} = 10$, respectively.

## 4.9 Two-State Hopping Simulation

In order to test how the equilibrium constant affects hopping dynamics, we simulated reversible hopping between two sites A and B (Fig. 4.11 a), with various equilibrium constants $K_{eq} = \tau_{AB}/\tau_{BA}$. Trajectories of 4000 points were simulated. $K_{eq}$ values ranging from 0.1 to 10 were employed for the simulation. For all the $K_{eq}$ tested, $\tau_{AB}$ and $\tau_{BA}$ were adjusted to yield an autocorrelation time constant of 50. Gaussian-noise with STD of 1.5 nm was added to the trajectories. When $K_{eq}$ is close to 1, the position autocorrelation of the trajectories show clear decay and yield time constants that are consistent with the simulation parameter (Fig. 4.11 b), whereas very large or small $K_{eq}$ (>3 or <0.33) typically result in poor autocorrelation with high noise level due to reduced number of transition events (Fig. 4.11 d). Considering the typical segment durations (4000-8000 frames) and the experimental noise level (1.3-2.9 nm), it is unlikely that the experimentally observed two-state polaron hopping dynamics have very large or small $K_{eq}$. Therefore, for segments with small autocorrelation time constants and relatively high noise level such that $K_{eq}$ can't be extracted from the position histogram, $K_{eq} = 1$ was used in order to obtain an approximate estimation of the hopping time and distance using the equations 4.6 and 4.7.


## 4.10 Multiple-State Hopping Simulation

In order to test our hypothesis that the fluorescence centroid movements of CPNs indicate polaron hopping between traps, we simulated random hopping trajectories and compared them to the experimental results. An example is shown in Fig. 4.12, we
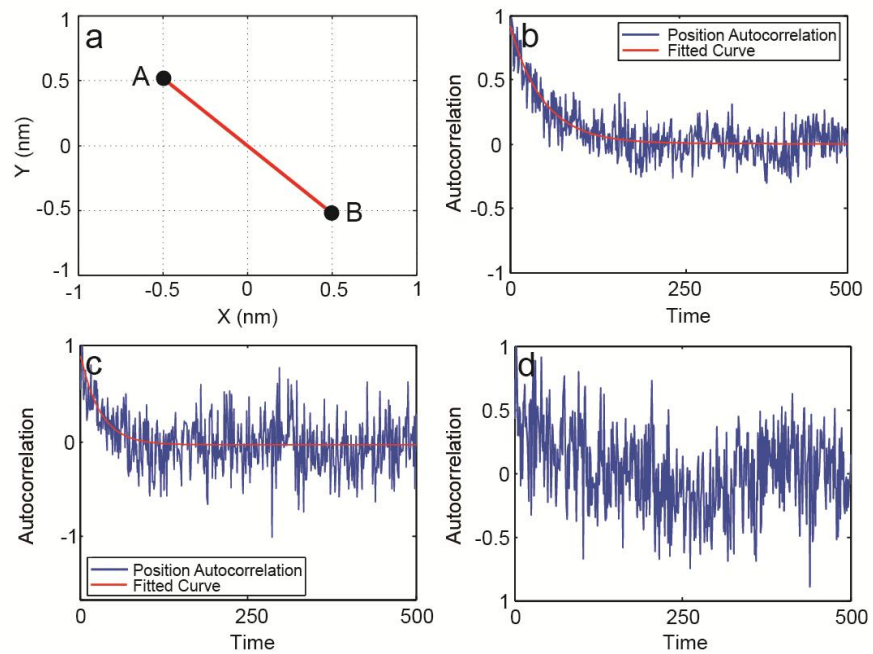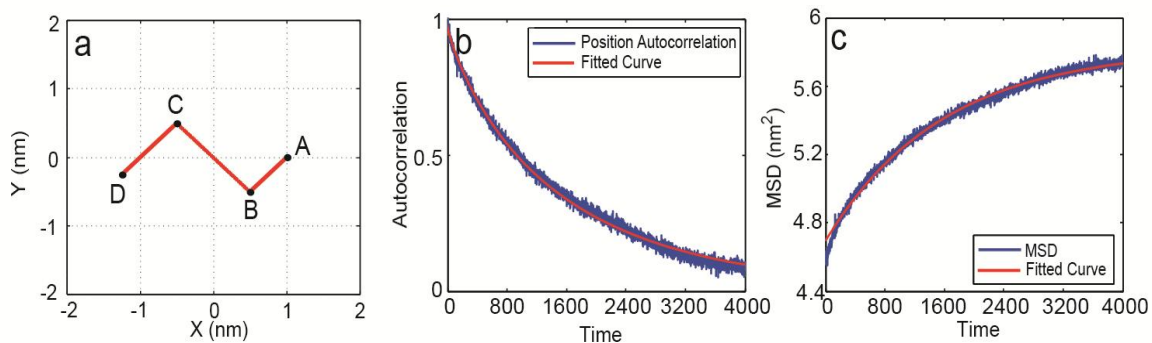
**Figure 4.12.** (a) Scheme showing the detail of a four-state hopping simulation. The trap positions are shown by the black dots and the hopping paths are shown by the red lines. (b) X autocorrelation fit to a KWW function $y = Ae^{-(x/\tau)^{\beta}}$ with fitting parameters $\tau = 1120$, $\beta = 0.77$;(c) X MSD fit to a confined diffusion function with diffusion coefficient $D_f$ and confinement length $L_f$ of 4.2 x $10^{-3}$ nm$^2$/frame and 1.15 nm, respectively.

simulated random hopping between 4 traps A, B, C, D, hopping time constants used for simulation were $\tau_{AB} = \tau_{BA} = 100$ , $\tau_{CD} = \tau_{DC} = 300$ , $\tau_{CB} = 1000$ , $\tau_{BC} = 2000$ . Trajectories of 200000 points were simulated. Gaussian-noise with STD of 1.5 nm was added to the trajectories. The autocorrelation of the trajectories typically fits poorly to a single exponential function while they fit much better to a bi-exponential or KWW functions (Fig. 4.12 b). The MSD shows confined diffusion behavior with deviation at early time (Fig. 4.12 c), similar to what we observed in the microscopy experiment. As shown in Fig. 4.12 b, time constant and $\beta$ value of 1120 and 0.77 were obtained from the KWW fitting to the X autocorrelation. According to the zero order moment of the KWW fit function, an average autocorrelation time constant $\langle \tau \rangle$ of 1310 was obtained. When the first 200 points of the X autocorrelation were fit to a single exponential decay, $\tau_{early} = 166$ was obtained from the fitting. Whereas $\tau_{late} = 1540$ was obtained from a single exponential fit to the X autocorrelation from lag time 2000 to 4000. Applying similar time windows used above, $L_{early} = 0.49$ nm and $L_{late} = 1.1$ nm were obtained by fitting different parts of the MSD to confined diffusion functions. Since the underlying dynamics are multiple exponential, $\tau_{early}$ and $\tau_{late}$, $L_{early}$ and $L_{late}$ do not directly indicate the hopping time constants or distances between the sites, rather they roughly provide the range of time and length scales of the hopping dynamics.

To extract more information, the simulated trajectories were divided into segments and analyzed in the same way as we discussed in the sections above. $\tau_{early}$ and $\tau_{late}$, $L_{early}$ and $L_{late}$ were extracted from each segment to construct histograms. As shown in Fig. 4.13 a, b, when the segment duration is long, for example 16000 points, the distributions
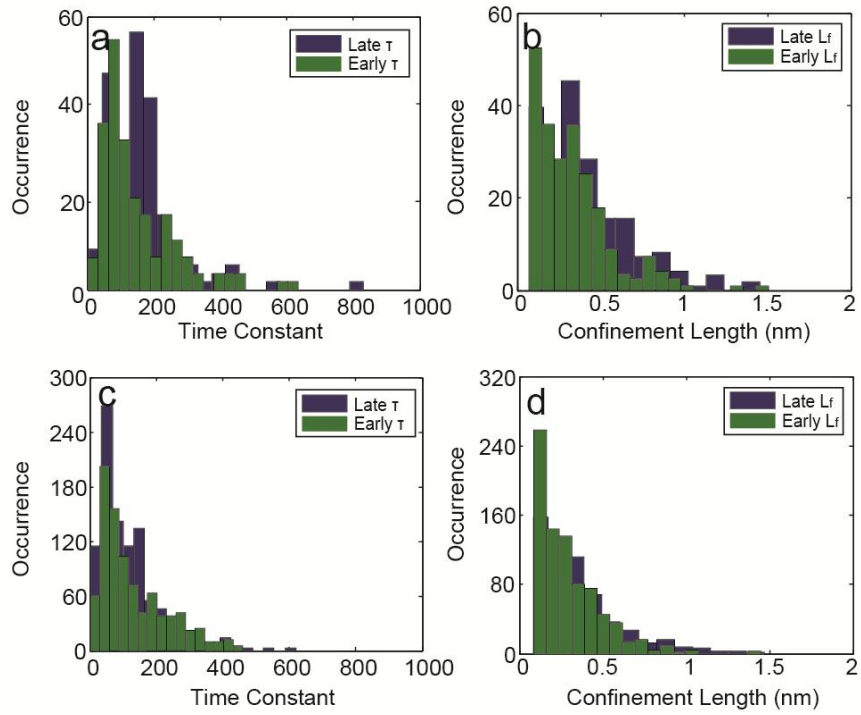
**Figure 4.13.** (a)(c) Histograms of time constants $\tau_{early}$ and $\tau_{late}$, obtained from analysis of (a) 16000 points segments and (c) 4000 points segments; (b)(d) Histograms of confinement lengths $L_{early}$ and $L_{late}$, obtained from analysis of (b) 16000 points segments and (d) 4000 points segments.

of $\tau_{early}$ and $\tau_{late}$, $L_{early}$ and $L_{late}$ show well separated peaks. As the segment length reduces, the distributions of $\tau_{early}$ and $\tau_{late}$, $L_{early}$ and $L_{late}$ become mostly overlapped, indicating that the dynamics in each segment become less heterogeneous in time and length scales (Fig. 4.13 c, d). When the segment duration is short, for example 4000 to 8000 points, the position autocorrelation of some segments show good fit to a single exponential decay, which likely indicates hopping between 2 traps. For these segments, the hopping times and distances were estimated from the autocorrelation time constants and MSD confinement lengths using the relationship derived in the previous section. The hopping time and distance distributions determined show discrete peaks, which are roughly consistent with the simulation parameters (Fig. 4.14). From the width of the distributions, we estimated that, under the typical experimental noise level (localization uncertainty of 1.5 nm), the hopping time and distance determined from segments of 4000 points have ~25% uncertainty. It should be noted that in this simulation, polaron spends most of the time hopping between the trap A, B and between the trap C, D. Transitions between the trap B and C are relatively rare, therefore, $\tau_{CB}$ and $\tau_{BC}$ were not extracted from the segmental analysis. However, the hopping time constants between the trap B and C can still be roughly estimated from the position autocorrelation of a long trajectory. As we discussed above, by fitting to the tail part of the X autocorrelation (lag time 2000 to 4000) to a single exponential decay, we obtain the approximate timescale of the slower hopping dynamics $\tau_{late} = 1540$, which is roughly consistent with $\tau_{CB}$ and $\tau_{BC}$ employed for the simulation.

121
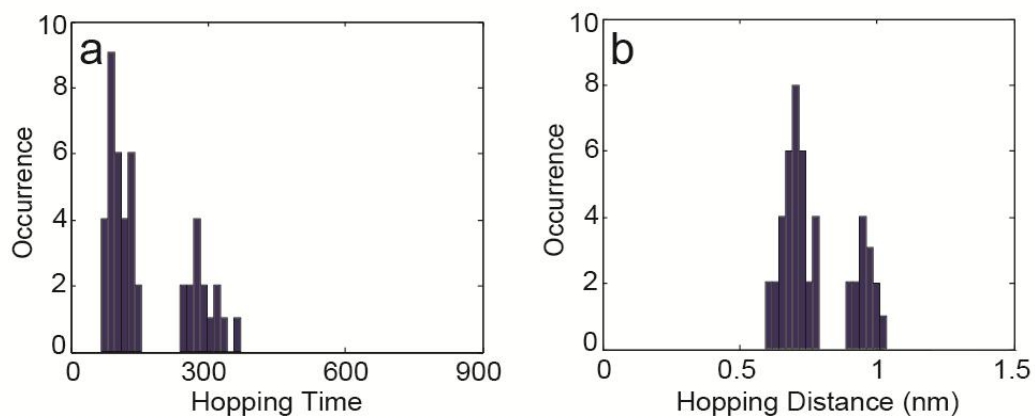
**Figure 4.14.** (a) Hopping time and (b) hopping distance distributions, determined from the segmented analysis of the simulated trajectories.

**4.11 Conclusions**

In conclusion, we have observed a broad range of polaron dynamics at kHz framerates. From the fluorescence intensity fluctuations of CPNs, we determined the timescale of the polaron generation and recombination dynamics to be around several seconds under the experimental conditions employed. While the prior published results from our lab indicated polaron motion on the ~0.1-10 s timescale (limited by the temporal resolution of the instrument),[59] our results with 1 kHz framerates indicate motion on timescale as short as 1 ms. In addition, we performed nanoscale mapping of energy landscape for single carrier transport. A two-tier energy landscape consisting of two dominate polymer chain conformations was observed, a glassy "blue" emitting phase and an ordered "red" emitting phase. We found that hole polarons are preferably generated and trapped within the red-emitting regions inside CPNs. Sometimes, repeated hopping between two red emitting trap sites can be observed in short segments of the trajectory. We estimated polaron hopping times and distances from the autocorrelation time constants and the MSD confinement lengths of these segments. The hopping time follows a power law distribution and the hopping distance roughly follows a single exponential distribution, indicating that fast and short ranged hops occur more frequently. From the hopping time distribution, we estimated the energy barrier height for polaron hopping in CPNs to be from 430 to 570 meV, which is on the larger side of the typical trap depth reported for disordered polymer films.[22, 23] likely indicating the presence of deep traps with nearest-neighbor distances of 2-5 nm, consistent with a low or moderate density of traps dominating charge transport at low carrier densities. Overall, these results provide an

unprecedented level of detail about the physical picture of polaron transport at the single

carrier level, offering an unique window to such processes in conjugated polymer films

and devices.

CHAPTER FIVE

CONCLUSIONS AND FUTURE DIRECTIONS

## 5.1 Characterization of Polaron Dynamics in CPNs

As discussed earlier, polaron dynamics have great impact on the photophysical properties of CPNs. For example, the fluorescence blinking behavior of CPNs is caused by the reversible generation and recombination dynamics of polarons.[31] Polaron population in CPNs is likely to be excitation power dependent. Abrupt changes in excitation intensity can cause polaron population to increase or decrease, which result in the fluorescence decay and recovery behavior.[11] Also, the large polaron population in CPNs at high excitation intensities likely causes the fluorescence saturation behavior.[10, 26] In addition, a hole polaron can effectively quench the local fluorescence and induce a dark spot in a CPN, which moves with the polaron and results in the displacement of the fluorescence centroid.[59] Improving our understanding of polaron dynamics is important for tunning the photophysical properties of CPNs for specific applications. In this dissertation, we have systematically investigated various phenomena associated with polaron dynamics in CPNs, including photoblinking, reversible fluorescence decay as well as twinkling behavior associated with polaron hopping. The timescales of polaron generation/recombination dynamics, the quenching efficiencies of single polarons, the distributions of polaron hopping time and distances have been determined in these studies.

The polaron generation and recombination dynamics in CPNs were characterized from the fluorescence intensity fluctuations. At low excitation intensities ($<100$ W/cm$^2$), there

is typically a single polaron or none present in CPNs. The intensity trajectories exhibit two-level fluctuations. The timescales of the polaron generation and recombination dynamics are typically around several seconds under such excitation powers, as determined from the durations of the "on" and "off" events. As the excitation power increases, the fluorescence intensity fluctuations of CPNs become more complex due to a larger population of polarons. Sometimes, a rapid fluorescence intensity decay within the first 5-20 s can be observed with CPNs, which is due to the growth of the polaron population from 0 to a steady state value. To understand this phenomenon better, we used a set of rate equations to model the polaron population growth process. Based on the model, we determined that the polaron recombination rate constant typically ranges from 0.1 s$^{-1}$ to 0.4 s$^{-1}$, which is consistent with $\tau_{\text{off}}$ determined from the blinking analysis. In the single particle spectrum analysis, we observed that CPNs typically exhibit "red" emission during the "on" state while show "blue" emission during the "off" state, indicating that hole polarons are preferably generated on the low energy emission sites inside CPNs.

The hopping motions of individual photo-generated hole polarons were investigated using the superresolution method developed previously. [59] At 1 kHz framerate, a broad range of hopping dynamics were observed. The MSD analysis indicated anomalous diffusive motion occurring on several length and time scales, yielding diffusion coefficients spanning over three orders of magnitude, corresponding to zero-field polaron mobilities ranging from $10^{-10}$ cm$^2$/Vs to $10^{-7}$ cm$^2$/Vs. The position autocorrelation analysis yielded a complex exponential decay with time constants ranging from one millisecond to

several seconds. These results qualitatively agree with the basic physical picture of multiple trap states with a range of energies and barrier heights reflected in a range of rates for polaron hopping between trap sites. By determining the spectra of the emission sites quenched by a hole polaron as it moves inside a CPN, we obtained a nanoscale map of the local emission characteristics inside a CPN. A two-tier energy landscape consisting of two dominate polymer chain conformations was observed for PFBT nanoparticles, a glassy "blue" emitting phase ($\lambda_{max}$ ~550 nm) and an ordered "red" emitting phase ($\lambda_{max}$ ~595 nm). Hole polarons were found to be highly trapped within the red-emitting regions inside CPNs. Sometimes, repeated hopping between two "red" emitting trap sites can be observed in short segments of the trajectory. We estimated the polaron hopping times and distances from the autocorrelation time constants and the MSD confinement lengths of these segments. The hopping time follows a power law distribution and the hopping distance roughly follows a single exponential distribution, indicating that fast and short ranged hops occur more frequently. From the hopping time distribution, we estimated the energy barrier height for polaron hopping in CPNs to be from 430 to 570 meV, which is on the larger side of the typical trap depth reported for disordered polymer films.[22, 23] likely indicating the presence of deep traps with nearest-neighbor distances of 2-5 nm, consistent with a low or moderate density of structural or chemical defects dominating charge transport at low carrier densities.

**5.2 Photoswitching Behavior of PCBM doped PFBT CPNs**

Owing to the exceptional brightness and photostability of CPNs,[10-12] there has been considerable interest in developing photoswitchable nanoparticle based on CPNs.[105, 106] However, designing photoswitchable CPNs have been proven to be challenging. Previous efforts in modifying CPNs for superresolution imaging typically involved incorporating photochromic dyes into CPNs.[105, 106] Due to the high chromophore density in CPNs, it typically requires a large number of dye molecules per nanoparticle in order to completely quench the emission from the conjugated polymers. One of the problems with this approach is that it is difficult to get so many dye molecules to synchronize. In addition, there are other competing processes in CPNs (quenching by hole polarons, energy transfer to low energy emitters) that can reduce the efficiency of energy transfer to the photochromic dyes. As a result, photochromic dye doped CPNs typically exhibit more or less linear rather than single-step photoswitching behavior.

In chapter 3, we demonstrated a novel method that utilizes controlled reversible generation and recombination of hole polarons inside CPNs to achieve superresolution imaging. By doping CPNs with fullerene derivative PCBM, a large population of polarons can be efficiently generated in CPNs, sufficient to nearly completely suppress the nanoparticle fluorescence. However, fluctuations in the number of polarons lead to occasional bursts of fluorescence, which is similar to the random telegraph signal noise observed in semiconductor devices. In this approach, the PCBMs act as master switches, hole polarons are efficiently generated at the PCBM/polymer interface and transported to different parts of the nanoparticles. For 20% PCBM doped PFBT CPNs, we determined that around $3\text{-}5 \times 10^4$ photons were detected during a switching event, which results in a

localization precision of ~0.6 nm, about 4 times better than the typical resolution obtained by localization of dye molecules. Since polaron generation is a photo-driven process, we showed that the blinking duty cycle of PCBM doped PFBT CPNs can be controlled by excitation intensity as well as by PCBM fraction. We demonstrated superresolution microscopy of *E. coli* using 20% PCBM doped PFBT CPNs. At 10 Hz framerates, we obtained the precise shape of the bacteria with a localization precision of ~5 nm. These results suggest that PCBM doped PFBT CPNs represent a novel class of promising superresolution probes with unprecedented localization precision and tunable spontaneous photoswitching (blinking) properties, which provide clear advantages for imaging of various biological systems.

## 5.3 Future Directions

There is still a lot to be learnt about polaron dynamics in conjugated polymers. It is known that generation of hole polarons involves electron transfer from conjugated polymers to singlet oxygen. However, it is currently unclear why the electron transfer reaction prefers to occur on the low energy emission sites in conjugated polymers. Based on the Marcus theory, one of the possible explanations is that, for the low energy excitons and singlet oxygen, there is a close match between the reorganization energy and the overall free energy of the transfer reaction. Or perhaps, polaron generation could occur at any part inside a CPN. However, due to energy funneling effect, only polarons generated on the low energy sites result in stepwise fluorescence blinking. There are also questions regarding the polaron recombination mechanism. It is assumed that the fluorescence

recovery involves electrons being back transferred to conjugated polymers. However, it is unclear what species is responsible for this process (particularly in undoped CPNs) and how do we control the recombination rate. Overall, carefully designed experiments are required in future research in order to shed light upon these issues.

In this dissertation, we demonstrated that PCBM doped PFBT nanoparticles exhibit spontaneous photoswitching behavior with unprecedented brightness. There is still a lot to be improved for these nanoparticles. In particular, we would like to achieve a more even distribution of PCBM in CPNs to reduce particle-to-particle variations in brightness, duty cycles, etc. It is also important to demonstrate bio-conjugation of these nanoparticles and obtain superresolution images of more complex biological samples. Besides spontaneous blinking, the reversible photobleaching and recovery processes could also be exploited for superresolution imaging. Through modulations of laser intensity or electric field strength, we should be able to switch the emission of PCBM doped CPNs "on" and "off". It is also important to obtain a deeper understanding of the various photophyscial processes in these nanoparticles. It is currently not well understood why PCBM doped PFBT nanoparticles exhibit slow spontaneous blinking (millisecond to second scale). As indicated by the previous researches,[113] the photo-induced charge separation at the polymer/PCBM interface is very fast (on the fs timescale). It could be that the slow fluorescence blinking observed for PCBM doped CPNs is mostly caused by hole polarons generated far away from the interface. Another possibility is that the fluorescence blinking is controlled by polaron transport from the interface, the duration of the "on" state is the amount of time that a hole polaron takes to hop from the interface to a

currently unoccupied spot inside a CPN. Hopefully, additional single particle/ultrafast experiments and modeling could improve our understanding of charge generation/transport processes in these complex nanoscale systems.

# REFERENCES

(1)     Günes, S.; Neugebauer, H.; Sariciftci, N. S. Conjugated Polymer-Based Organic Solar Cells. *Chem. Rev.* **2007,** *107* (4), 1324-1338.

(2)     Ma, W.; Yang, C.; Gong, X.; Lee, K.; Heeger, A. J. Thermally Stable, Efficient Polymer Solar Cells with Nanoscale Control of the Interpenetrating Network Morphology. *Adv. Funct. Mater.* **2005,** *15* (10), 1617-1622.

(3)     Kim, J. Y.; Lee, K.; Coates, N. E.; Moses, D.; Nguyen, T.-Q.; Dante, M.; Heeger, A. J. Efficient Tandem Polymer Solar Cells Fabricated by All-Solution Processing. *Science* **2007,** *317* (5835), 222-225.

(4)     Babel, A.; Jenekhe, S. A. High Electron Mobility in Ladder Polymer Field-Effect Transistors. *J. Am. Chem. Soc.* **2003,** *125* (45), 13656-13657.

(5)     Liu, J.; Zhang, R.; Sauvé, G.; Kowalewski, T.; McCullough, R. D. Highly Disordered Polymer Field Effect Transistors: N-alkyl dithieno [3, 2-d: 2′, 3′-d] pyrrole-Based Copolymers with Surprisingly High Charge Carrier Mobilities. *J. Am. Chem. Soc.* **2008,** *130* (39), 13167-13176.

(6)     Zhang, W.; Smith, J.; Watkins, S. E.; Gysel, R.; McGehee, M.; Salleo, A.; Kirkpatrick, J.; Ashraf, S.; Anthopoulos, T.; Heeney, M. Indacenodithiophene Semiconducting Polymers for High-Performance, Air-Stable Transistors. *J. Am. Chem. Soc.* **2010,** *132* (33), 11437-11439.

(7)     Bozano, L.; Carter, S.; Scott, J.; Malliaras, G.; Brock, P. Temperature-and Field-Dependent Electron and Hole Mobilities in Polymer Light-Emitting Diodes. *Appl. Phys. Lett.* **1999,** *74* (8), 1132.

(8)     Tessler, N.; Medvedev, V.; Kazes, M.; Kan, S.; Banin, U. Efficient Near-Infrared Polymer Nanocrystal Light-Emitting Diodes. *Science* **2002,** *295* (5559), 1506-1508.

(9)     Tanase, C.; Meijer, E.; Blom, P.; De Leeuw, D. Unification of the Hole Transport in Polymeric Field-Effect Transistors and Light-Emitting Diodes. *Phys. Rev. Lett.* **2003,** *91* (21), 216601.

(10)    Wu, C.; Bull, B.; Szymanski, C.; Christensen, K.; McNeill, J. Multicolor Conjugated Polymer Dots for Biological Fluorescence Imaging. *ACS nano* **2008,** *2* (11), 2415-2423.

(11)    Tian, Z.; Yu, J.; Wu, C.; Szymanski, C.; McNeill, J. Amplified Energy Transfer in Conjugated Polymer Nanoparticle Tags and Sensors. *Nanoscale* **2010,** *2* (10), 1999-2011.

(12)    Jiang, Y.; McNeill, J. Light-Harvesting and Amplified Energy Transfer in Conjugated Polymer Nanoparticles. *Chem. Rev.* **2017,** *117* (2), 838–859.

(13)    Wu, C.; Bull, B.; Christensen, K.; McNeill, J. Ratiometric Single-Nanoparticle Oxygen Sensors for Biological Imaging. *Angew. Chem. Int. Ed.* **2009,** *48* (15), 2741-2745.

(14)    Ye, F.; Wu, C.; Jin, Y.; Chan, Y.-H.; Zhang, X.; Chiu, D. T. Ratiometric Temperature Sensing with Semiconducting Polymer Dots. *J. Am. Chem. Soc.* **2011,** *133* (21), 8146-8149.

(15)    McCullough, R. D.; Williams, S. P. Toward Tuning Electrical and Optical Properties in Conjugated Polymers Using Side-Chains: Highly Conductive Head-to-Tail, Heteroatom Functionalized Polythiophenes. *J. Am. Chem. Soc.* **1993,** *115* (24), 11608-11609.

(16)    Hutchison, G.; Zhao, Y.-J.; Delley, B.; Freeman, A.; Ratner, M.; Marks, T. Electronic Structure of Conducting Polymers: Limitations of Oligomer Extrapolation Approximations and Effects of Heteroatoms. *Phys. Rev. B* **2003,** *68* (3), 035204.

(17)    Wudl, F. The Chemical Properties of Buckminsterfullerene ($C_{60}$) and the Birth and Infancy of Fulleroids. *Acc. Chem. Res.* **1992,** *25* (3), 157-161.

(18)    Reyes-Reyes, M.; Kim, K.; Carroll, D. L. High-Efficiency Photovoltaic Devices Based on Annealed Poly (3-hexylthiophene) and 1-(3-methoxycarbonyl)-propyl-1-phenyl-(6, 6) $C_{61}$ Blends. *Appl. Phys. Lett.* **2005,** *87* (8), 3506.

(19)    Kim, H.-C.; Park, S.-M.; Hinsberg, W. D. Block Copolymer Based Nanostructures: Materials, Processes, and Applications to Electronics. *Chem. Rev.* **2009,** *110* (1), 146-177.

(20)    Krebs, F. C.; Tromholt, T.; Jørgensen, M. Upscaling of Polymer Solar Cell Fabrication Using Full Roll-to-Roll Processing. *Nanoscale* **2010,** *2* (6), 873-886.

(21)    Tessler, N.; Preezant, Y.; Rappaport, N.; Roichman, Y. Charge Transport in Disordered Organic Materials and Its Relevance to Thin-Film Devices: A Tutorial Review. *Adv. Mater.* **2009,** *21* (27), 2741-2761.

(22)    Pasveer, W.; Cottaar, J.; Tanase, C.; Coehoorn, R.; Bobbert, P.; Blom, P.; De Leeuw, D.; Michels, M. Unified Description of Charge-Carrier Mobilities in Disordered Semiconducting Polymers. *Phys. Rev. Lett.* **2005,** *94* (20), 206601.

(23)     Noriega, R.; Rivnay, J.; Vandewal, K.; Koch, F. P.; Stingelin, N.; Smith, P.; Toney, M. F.; Salleo, A. A General Relationship between Disorder, Aggregation and Charge Transport in Conjugated Polymers. *Nat. Mater.* **2013,** *12* (11), 1038-1044.

(24)     Wu, C.; Hansen, S. J.; Hou, Q.; Yu, J.; Zeigler, M.; Jin, Y.; Burnham, D. R.; McNeill, J. D.; Olson, J. M.; Chiu, D. T. Design of Highly Emissive Polymer Dot Bioconjugates for in Vivo Tumor Targeting. *Angew. Chem. Int. Ed.* **2011,** *50* (15), 3430-3434.

(25)     Tian, Z.; Yu, J.; Wang, X.; Groff, L. C.; Grimland, J. L.; McNeill, J. D. Conjugated Polymer Nanoparticles Incorporating Antifade Additives for Improved Brightness and Photostability. *J. Phys. Chem. B* **2012,** *117* (16), 4517-4520.

(26)     Wang, X.; Groff, L. C.; McNeill, J. D. Photoactivation and Saturated Emission in Blended Conjugated Polymer Nanoparticles. *Langmuir* **2013,** *29* (45), 13925-13931.

(27)     Groff, L. C.; Jiang, Y.; Wang, X.; McNeill, J. D. Effect of Swelling on Multiple Energy Transfer in Conjugated Polymer Nanoparticles. *J. Phys. Chem. C* **2017,** *121* (13), 7549-7557.

(28)     Wang, X.; Groff, L. C.; McNeill, J. D. Multiple Energy Transfer Dynamics in Blended Conjugated Polymer Nanoparticles. *J. Phys. Chem. C* **2014,** *118* (44), 25731-25739.

(29)     Jiang, Y.; Novoa, M.; Nongnual, T.; Powell, R.; Bruce, T. F.; McNeill, J. D. Improved Superresolution Imaging Using Telegraph Noise in Organic Semiconductor Nanoparticles. *Nano Lett.* **2017,** *17* (6), 3896–3901.

(30)     Wu, C.; Zheng, Y.; Szymanski, C.; McNeill, J. Energy Transfer in a Nanoscale Multichromophoric System: Fluorescent Dye-Doped Conjugated Polymer Nanoparticles. *J. Phys. Chem. C* **2008,** *112* (6), 1772-1781.

(31)     Vanden Bout, D. A.; Yip, W.-T.; Hu, D.; Fu, D.-K.; Swager, T. M.; Barbara, P. F. Discrete Intensity Jumps and Intramolecular Electronic Energy Transfer in the Spectroscopy of Single Conjugated Polymer Molecules. *Science* **1997,** *277* (5329), 1074-1077.

(32)     Yu, J.; Hu, D.; Barbara, P. F. Unmasking Electronic Energy Transfer of Conjugated Polymers by Suppression of $O_2$ Quenching. *Science* **2000,** *289* (5483), 1327-1330.

(33)     Yang, Z.; Huck, W. T.; Clarke, S. M.; Tajbakhsh, A. R.; Terentjev, E. M. Shape-Memory Nanoparticles from Inherently Non-Spherical Polymer Colloids. *Nat. Mater.* **2005,** *4* (6), 486-490.

(34)    Helgesen, M.; Søndergaard, R.; Krebs, F. C. Advanced Materials and Processes for Polymer Solar Cell Devices. *J. Mater. Chem.* **2010,** *20* (1), 36-60.

(35)    Niles, E. T.; Roehling, J. D.; Yamagata, H.; Wise, A. J.; Spano, F. C.; Moulé, A. J.; Grey, J. K. J-Aggregate Behavior in Poly-3-hexylthiophene Nanofibers. *J. Phys. Chem. Lett.* **2012,** *3* (2), 259-263.

(36)    Wu, C.; McNeill, J. Swelling-Controlled Polymer Phase and Fluorescence Properties of Polyfluorene Nanoparticles. *Langmuir* **2008,** *24* (11), 5855-5861.

(37)    Labastide, J. A.; Baghgar, M.; Dujovne, I.; Venkatraman, B. H.; Ramsdell, D. C.; Venkataraman, D.; Barnes, M. D. Time-and Polarization-Resolved Photoluminescence of Individual Semicrystalline Polythiophene (P3HT) Nanoparticles. *J. Phys. Chem. Lett.* **2011,** *2* (17), 2089-2093.

(38)    Kaake, L.; Barbara, P. F.; Zhu, X.-Y. Intrinsic Charge Trapping in Organic and Polymeric Semiconductors: A Physical Chemistry Perspective. *J. Phys. Chem. Lett.* **2010,** *1* (3), 628-635.

(39)    Hu, D.; Yu, J.; Wong, K.; Bagchi, B.; Rossky, P. J.; Barbara, P. F. Collapse of Stiff Conjugated Polymers with Chemical Defects into Ordered, Cylindrical Conformations. *Nature* **2000,** *405* (6790), 1030-1033.

(40)    Hu, Z.; Tenery, D.; Bonner, M. S.; Gesquiere, A. J. Correlation between Spectroscopic and Morphological Properties of Composite P3HT/PCBM Nanoparticles Studied by Single Particle Spectroscopy. *J. Lumin.* **2010,** *130* (5), 771-780.

(41)    Frenkel, J. On the Transformation of Light into Heat in Solids. I. *Phys. Rev.* **1931,** *37* (1), 17.

(42)    Spano, F. C.; Silva, C. H- and J-Aggregate Behavior in Polymeric Semiconductors. *Annu. Rev. Phys. Chem.* **2014,** *65*, 477-500.

(43)    Yamagata, H.; Hestand, N. J.; Spano, F. C.; Köhler, A.; Scharsich, C.; Hoffmann, S. T.; Bässler, H. The Red-Phase of Poly [2-methoxy-5-(2-ethylhexyloxy)-1, 4-phenylenevinylene](MEH-PPV): A Disordered HJ-Aggregate. *J. Chem. Phys.* **2013,** *139* (11), 114903.

(44)    Kasha, M.; Rawls, H.; Ashraf El-Bayoumi, M. The Exciton Model in Molecular Spectroscopy. *Pure Appl. Chem.* **1965,** *11* (3-4), 371-392.

(45)    Davydov, A. S. The Theory of Molecular Excitons. *Sov. Phys. Usp.* **1964,** *7* (2), 145.

(46) Emelianova, E.; Athanasopoulos, S.; Silbey, R. J.; Beljonne, D. 2D Excitons as Primary Energy Carriers in Organic Crystals: The Case of Oligoacenes. *Phys. Rev. Lett.* **2010,** *104* (20), 206405.

(47) Förster, T. Zwischenmolekulare Energiewanderung Und Fluoreszenz. *Annu. Phys.* **1948,** *437* (1-2), 55-75.

(48) Kasha, M. Characterization of Electronic Transitions in Complex Molecules. *Disc. Faraday Soc.* **1950,** *9*, 14-19.

(49) Dexter, D. L. A Theory of Sensitized Luminescence in Solids. *J. Chem. Phys.* **1953,** *21* (5), 836-850.

(50) Franck, J.; Dymond, E. Elementary Processes of Photochemical Reactions. *Trans. Faraday Soc.* **1926,** *21* (February), 536-542.

(51) Huang, K.; Rhys, A. Theory of Light Absorption and Non-Radiative Transitions in F-Centres, *Proc. R. Soc. A* **1950,** *204*, 406-423.

(52) Spano, F. C. Absorption in Regio-Regular Poly (3-hexyl) thiophene Thin Films: Fermi Resonances, Interband Coupling and Disorder. *Chem. Phys.* **2006,** *325* (1), 22-35.

(53) Spano, F. C. The Spectral Signatures of Frenkel Polarons in H-and J-Aggregates. *Acc. Chem. Res.* **2009,** *43* (3), 429-439.

(54) Birks, J.; Dyson, D.; Munro, I. Excimer' fluorescence. II. Lifetime Studies of Pyrene Solutions, *Proc. R. Soc. A* **1963,** *275*, 575-588.

(55) Walker, M. S.; Bednar, T. W.; Lumry, R. Exciplex Formation in the Excited State of Indole. *J. Chem. Phys.* **1966,** *45* (9), 3455-3456.

(56) Su, W. P.; Schrieffer, J.; Heeger, A. J. Solitons in Polyacetylene. *Phys. Rev. Lett.* **1979,** *42* (25), 1698.

(57) Barth, S.; Bässler, H. Intrinsic Photoconduction in PPV-Type Conjugated Polymers. *Phys. Rev. Lett.* **1997,** *79* (22), 4445.

(58) Wayne, R. Singlet Molecular Oxygen. *Adv. Photochem.* **1969,** *7* (3), 1.

(59) Yu, J.; Wu, C.; Tian, Z.; McNeill, J. Tracking of Single Charge Carriers in a Conjugated Polymer Nanoparticle. *Nano Lett.* **2012,** *12* (3), 1300-1306.

(60)    Lochner, K.; Bässler, H.; Tieke, B.; Wegner, G. Photoconduction in Polydiacetylene Multilayer Structures and Single Crystals. Evidence for Band-to-Band Excitation. *Phys.Status Solidi B* **1978,** *88* (2), 653-661.

(61)    Holstein, T. Studies of Polaron Motion: Part I. The Molecular-Crystal Model. *Annu. Phys.* **1959,** *8* (3), 325-342.

(62)    Emin, D.; Holstein, T. Studies of Small-Polaron Motion IV. Adiabatic Theory of the Hall Effect. *Annu. Phys.* **1969,** *53* (3), 439-520.

(63)    Lebedev, E.; Dittrich, T.; Petrova-Koch, V.; Karg, S.; Brütting, W. Charge Carrier Mobility in Poly (p-phenylenevinylene) Studied by the Time-of-Flight Technique. *Appl. Phys. Lett.* **1997,** *71* (18), 2686-2688.

(64)    Bässler, H. Charge Transport in Disordered Organic Photoconductors a Monte Carlo Simulation Study. *Phys. Status Solidi B* **1993,** *175* (1), 15-56.

(65)    Bässler, H.; Köhler, A. Charge Transport in Organic Semiconductors. In *Unimolecular and Supramolecular Electronics I*, Springer: 2012; pp 1-65.

(66)    Bloch, F. Über Die Quantenmechanik Der Elektronen in Kristallgittern. *Z. Phys. A: Hadron. Nucl.* **1929,** *52* (7), 555-600.

(67)    Wannier, G. H. The Structure of Electronic Excitation Levels in Insulating Crystals. *Phys. Rev.* **1937,** *52* (3), 191.

(68)    Mott, N. F. The Basis of the Electron Theory of Metals, with Special Reference to the Transition Metals. *Proc. Phys. Soc. A* **1949,** *62* (7), 416.

(69)    Kasha, M. Energy Transfer Mechanisms and the Molecular Exciton Model for Molecular Aggregates. *Radiat. Res.* **1963,** *20* (1), 55-70.

(70)    Köhler, A.; Bässler, H. *Electronic Processes in Organic Semiconductors: An Introduction*. John Wiley & Sons: 2015.

(71)    Mott, N. Conduction in Glasses Containing Transition Metal Ions. *J. Non-Cryst. Solids* **1968,** *1* (1), 1-17.

(72)    Marcus, R. A. On the Theory of Oxidation-Reduction Reactions Involving Electron Transfer. I. *J. Chem. Phys.* **1956,** *24* (5), 966-978.

(73)    Marcus, R. A. Chemical and Electrochemical Electron-Transfer Theory. *Annu. Rev. Phys. Chem.* **1964,** *15* (1), 155-196.

(74)     Miller, J.; Calcaterra, L.; Closs, G. Intramolecular Long-Distance Electron Transfer in Radical Anions. The Effects of Free Energy and Solvent on the Reaction Rates. *J. Am. Chem. Soc.* **1984,** *106* (10), 3047-3049.

(75)     Miller, A.; Abrahams, E. Impurity Conduction at Low Concentrations. *Phys. Rev.* **1960,** *120* (3), 745.

(76)     Kirkpatrick, S. Percolation and Conduction. *Rev. Mod. Phys.* **1973,** *45* (4), 574.

(77)     Abbe, E. Beiträge Zur Theorie Des Mikroskops Und Der Mikroskopischen Wahrnehmung. *Arch. Mikrosk. Anat.* **1873,** *9* (1), 413-418.

(78)     Betzig, E.; Lewis, A.; Harootunian, A.; Isaacson, M.; Kratschmer, E. Near Field Scanning Optical Microscopy (NSOM): Development and Biophysical Applications. *Biophys. J.* **1986,** *49* (1), 269-279.

(79)     Synge, E., Xxxviii. A Suggested Method for Extending Microscopic Resolution into the Ultra-Microscopic Region. *Lond. Edinb. Dubl. Phil. Mag.* **1928,** *6* (35), 356-362.

(80)     Hell, S. W.; Wichmann, J. Breaking the Diffraction Resolution Limit by Stimulated Emission: Stimulated-Emission-Depletion Fluorescence Microscopy. *Opt. Lett.* **1994,** *19* (11), 780-782.

(81)     Hell, S. W.; Kroug, M. Ground-State-Depletion Fluorscence Microscopy: A Concept for Breaking the Diffraction Resolution Limit. *Appl. Phys. B* **1995,** *60* (5), 495-497.

(82)     Bretschneider, S.; Eggeling, C.; Hell, S. W. Breaking the Diffraction Barrier in Fluorescence Microscopy by Optical Shelving. *Phys. Rev. Lett.* **2007,** *98* (21), 218103.

(83)     Betzig, E.; Patterson, G. H.; Sougrat, R.; Lindwasser, O. W.; Olenych, S.; Bonifacino, J. S.; Davidson, M. W.; Lippincott-Schwartz, J.; Hess, H. F. Imaging Intracellular Fluorescent Proteins at Nanometer Resolution. *Science* **2006,** *313* (5793), 1642-1645.

(84)     Rust, M. J.; Bates, M.; Zhuang, X. Sub-Diffraction-Limit Imaging by Stochastic Optical Reconstruction Microscopy (STORM). *Nat. Methods* **2006,** *3* (10), 793-796.

(85)     Thompson, R. E.; Larson, D. R.; Webb, W. W. Precise Nanometer Localization Analysis for Individual Fluorescent Probes. *Biophys. J.* **2002,** *82* (5), 2775-2783.

(86)     Yildiz, A.; Forkey, J. N.; McKinney, S. A.; Ha, T.; Goldman, Y. E.; Selvin, P. R. Myosin V Walks Hand-over-Hand: Single Fluorophore Imaging with 1.5-nm Localization. *Science* **2003,** *300* (5628), 2061-2065.

(87)    Dertinger, T.; Colyer, R.; Iyer, G.; Weiss, S.; Enderlein, J. Fast, Background-Free, 3D Super-Resolution Optical Fluctuation Imaging (SOFI). *Proc. Natl. Acad. Sci. U. S. A.* **2009,** *106* (52), 22287-22292.

(88)    Szymanski, C.; Wu, C.; Hooper, J.; Salazar, M. A.; Perdomo, A.; Dukes, A.; McNeill, J. Single Molecule Nanoparticles of the Conjugated Polymer MEH-PPV, Preparation and Characterization by Near-Field Scanning Optical Microscopy. *J. Phys. Chem. B* **2005,** *109* (18), 8543-8546.

(89)    Rugar, D.; Hansma, P. Atomic Force Microscopy. *Phys. Today* **1990,** *43* (10), 23-30.

(90)    Giessibl, F. J. Advances in Atomic Force Microscopy. *Rev. Mod. Phys.* **2003,** *75* (3), 949.

(91)    Eaton, P.; West, P. *Atomic Force Microscopy*. Oxford University Press: 2010.

(92)    Berne, B. J.; Pecora, R. *Dynamic Light Scattering: With Applications to Chemistry, Biology, and Physics*. Courier Corporation: 2000.

(93)    Frisken, B. J. Revisiting the Method of Cumulants for the Analysis of Dynamic Light-Scattering Data. *Appl. Opt.* **2001,** *40* (24), 4087-4091.

(94)    Press, W. H. *Numerical Recipes 3rd Edition: The Art of Scientific Computing*. Cambridge university press: 2007.

(95)    Chenouard, N.; Smal, I.; De Chaumont, F.; Maška, M.; Sbalzarini, I. F.; Gong, Y.; Cardinale, J.; Carthel, C.; Coraluppi, S.; Winter, M. Objective Comparison of Particle Tracking Methods. *Nat. Methods* **2014,** *11* (3), 281-289.

(96)    Michalet, X.; Berglund, A. J. Optimal Diffusion Coefficient Estimation in Single-Particle Tracking. *Phys. Rev. E* **2012,** *85* (6), 061916.

(97)    Meijering, E.; Dzyubachyk, O.; Smal, I. 9 Methods for Cell and Particle Tracking. *Methods Enzymol.* **2012,** *504* (9), 183-200.

(98)    Klar, T. A.; Hell, S. W. Subdiffraction Resolution in Far-Field Fluorescence Microscopy. *Opt. Lett.* **1999,** *24* (14), 954-956.

(99)    Subach, F. V.; Patterson, G. H.; Manley, S.; Gillette, J. M.; Lippincott-Schwartz, J.; Verkhusha, V. V. Photoactivatable Mcherry for High-Resolution Two-Color Fluorescence Microscopy. *Nat. Methods* **2009,** *6* (2), 153-159.

(100)   Bates, M.; Blosser, T. R.; Zhuang, X. Short-Range Spectroscopic Ruler Based on a Single-Molecule Optical Switch. *Phys. Rev. Lett.* **2005,** *94* (10), 108101.

(101)   Fölling, J.; Belov, V.; Kunetsky, R.; Medda, R.; Schönle, A.; Egner, A.; Eggeling, C.; Bossi, M.; Hell, S. W. Photochromic Rhodamines Provide Nanoscopy with Optical Sectioning. *Angew. Chem. Int. Ed.* **2007,** *46* (33), 6266-6270.

(102)   Habuchi, S.; Ando, R.; Dedecker, P.; Verheijen, W.; Mizuno, H.; Miyawaki, A.; Hofkens, J. Reversible Single-Molecule Photoswitching in the GFP-Like Fluorescent Protein Dronpa. *Proc. Natl. Acad. Sci. U.S.A.* **2005,** *102* (27), 9511-9516.

(103)   Brakemann, T.; Stiel, A. C.; Weber, G.; Andresen, M.; Testa, I.; Grotjohann, T.; Leutenegger, M.; Plessmann, U.; Urlaub, H.; Eggeling, C. A Reversibly Photoswitchable GFP-Like Protein with Fluorescence Excitation Decoupled from Switching. *Nat. Biotechnol.* **2011,** *29* (10), 942-947.

(104)   Hu, D.; Tian, Z.; Wu, W.; Wan, W.; Li, A. D. Photoswitchable Nanoparticles Enable High-Resolution Cell Imaging: PULSAR Microscopy. *J. Am. Chem. Soc.* **2008,** *130* (46), 15279-15281.

(105)   Chan, Y.-H.; Gallina, M. E.; Zhang, X.; Wu, I.-C.; Jin, Y.; Sun, W.; Chiu, D. T. Reversible Photoswitching of Spiropyran-Conjugated Semiconducting Polymer Dots. *Anal. Chem.* **2012,** *84* (21), 9431-9438.

(106)   Harbron, E. J.; Davis, C. M.; Campbell, J. K.; Allred, R. M.; Kovary, M. T.; Economou, N. J. Photochromic Dye-Doped Conjugated Polymer Nanoparticles: Photomodulated Emission and Nanoenvironmental Characterization. *J. Phys. Chem. C* **2009,** *113* (31), 13707-13714.

(107)   McNeill, J. D.; O'Connor, D. B.; Adams, D. M.; Barbara, P. F.; Kämmer, S. B. Field-Induced Photoluminescence Modulation of MEH-PPV under Near-Field Optical Excitation. *J. Phys. Chem. B* **2001,** *105* (1), 76-82.

(108)   Gesquiere, A. J.; Park, S.-J.; Barbara, P. F. Hole-Induced Quenching of Triplet and Singlet Excitons in Conjugated Polymers. *J. Am. Chem. Soc.* **2005,** *127* (26), 9556-9560.

(109)   Ralls, K.; Skocpol, W.; Jackel, L.; Howard, R.; Fetter, L.; Epworth, R.; Tennant, D. Discrete Resistance Switching in Submicrometer Silicon Inversion Layers: Individual Interface Traps and Low-Frequency (1/F?) Noise. *Phys. Rev. Lett.* **1984,** *52* (3), 228.

(110)   Dempsey, G. T.; Vaughan, J. C.; Chen, K. H.; Bates, M.; Zhuang, X. Evaluation of Fluorophores for Optimal Performance in Localization-Based Super-Resolution Imaging. *Nat. Methods* **2011,** *8* (12), 1027-1036.

(111)   Groff, L. C.; Wang, X.; McNeill, J. D. Measurement of Exciton Transport in Conjugated Polymer Nanoparticles. *J. Phys. Chem. C* **2013,** *117* (48), 25748-25755.

(112)   Hu, Z.; Gesquiere, A. J. Charge Trapping and Storage by Composite P3HT/PC60BM Nanoparticles Investigated by Fluorescence-Voltage/Single Particle Spectroscopy. *J. Am. Chem. Soc.* **2011,** *133* (51), 20850-20856.

(113)   Clafton, S. N.; Huang, D. M.; Massey, W. R.; Kee, T. W. Femtosecond Dynamics of Excitons and Hole-Polarons in Composite P3HT/PCBM Nanoparticles. *J. Phys. Chem. B* **2013,** *117* (16), 4626-4633.

(114)   Piok, T.; Plank, H.; Mauthner, G.; Gamerith, S.; Gadermaier, C.; Wenzl, F. P.; Patil, S.; Montenegro, R.; Bouguettaya, M.; Reynolds, J. R. Solution Processed Conjugated Polymer Multilayer Structures for Light Emitting Devices. *Jpn. J. Appl. Phys.* **2005,** *44* (1S), 479.

(115)   Im, C.; Bässler, H.; Rost, H.; Hörhold, H. Hole Transport in Polyphenylenevinylene-ether under Bulk Photoexcitation and Sensitized Injection. *J. Chem. Phys.* **2000,** *113* (9), 3802-3807.

(116)   Blom, P.; De Jong, M.; Vleggaar, J. Electron and Hole Transport in Poly (p-phenylene vinylene) Devices. *Appl. Phys. Lett.* **1996,** *68* (23), 3308-3310.

(117)   Fong, H. H.; Papadimitratos, A.; Hwang, J.; Kahn, A.; Malliaras, G. G. Hole Injection in a Model Fluorene–triarylamine Copolymer. *Adv. Funct. Mater.* **2009,** *19* (2), 304-310.

(118)   Khan, R.; Poplavskyy, D.; Kreouzis, T.; Bradley, D. Hole Mobility within Arylamine-Containing Polyfluorene Copolymers: A Time-of-Flight Transient-Photocurrent Study. *Phys. Rev. B* **2007,** *75* (3), 035215.

(119)   McNeill, J. D.; O'Connor, D. B.; Barbara, P. F. Imaging Organic Device Function with Near-Field Scanning Optical Microscopy. *J. Chem. Phys.* **2000,** *112* (18), 7811-7821.

(120)   McNeill, J. D.; Barbara, P. F. NSOM Investigation of Carrier Generation, Recombination, and Drift in a Conjugated Polymer. *J. Phys. Chem. B* **2002,** *106* (18), 4632-4639.

(121)   Yu, J.; Song, N. W.; McNeill, J. D.; Barbara, P. F. Efficient Exciton Quenching by Hole Polarons in the Conjugated Polymer MEH-PPV. *Isr. J. Chem.* **2004,** *44* (1-3), 127-132.

(122)   Palacios, R. E.; Fan, F.-R. F.; Grey, J. K.; Suk, J.; Bard, A. J.; Barbara, P. F. Charging and Discharging of Single Conjugated-Polymer Nanoparticles. *Nat. Mater.* **2007,** *6* (9), 680-685.

(123)   Bolinger, J. C.; Traub, M. C.; Adachi, T.; Barbara, P. F. Ultralong-Range Polaron-Induced Quenching of Excitons in Isolated Conjugated Polymers. *Science* **2011,** *331* (6017), 565-567.

(124)   Coropceanu, V.; Cornil, J.; da Silva Filho, D. A.; Olivier, Y.; Silbey, R.; Brédas, J.-L. Charge Transport in Organic Semiconductors. *Chem. Rev.* **2007,** *107* (4), 926-952.

(125)   Hu, D.; Yu, J.; Barbara, P. F. Single-Molecule Spectroscopy of the Conjugated Polymer MEH-PPV. *J. Am. Chem. Soc.* **1999,** *121* (29), 6936-6937.

(126)   Yan, H.; Swaraj, S.; Wang, C.; Hwang, I.; Greenham, N. C.; Groves, C.; Ade, H.; McNeill, C. R. Influence of Annealing and Interfacial Roughness on the Performance of Bilayer Donor/Acceptor Polymer Photovoltaic Devices. *Adv. Funct. Mater.* **2010,** *20* (24), 4329-4337.

(127)   Blakesley, J. C.; Castro, F. A.; Kylberg, W.; Dibb, G. F.; Arantes, C.; Valaski, R.; Cremona, M.; Kim, J. S.; Kim, J.-S. Towards Reliable Charge-Mobility Benchmark Measurements for Organic Semiconductors. *Org. Electron.* **2014,** *15* (6), 1263-1272.

(128)   Sirringhaus, H.; Brown, P.; Friend, R.; Nielsen, M. M. Two-Dimensional Charge Transport in Self-Organized, High-Mobility Conjugated Polymers. *Nature* **1999,** *401* (6754), 685.

(129)   Beljonne, D.; Cornil, J.; Sirringhaus, H.; Brown, P.; Shkunov, M.; Friend, R.; Bredas, J. Optical Signature of Delocalized Polarons in Conjugated Polymers. *Adv. Funct. Mater.* **2001,** *11* (3), 229-234.

(130)   Nelson, J.; Chandler, R. E. Random Walk Models of Charge Transfer and Transport in Dye Sensitized Systems. *Coord. Chem. Rev.* **2004,** *248* (13), 1181-1194.

(131)   Nelson, J. Continuous-Time Random-Walk Model of Electron Transport in Nanocrystalline $TiO_2$ Electrodes. *Phys. Rev. B* **1999,** *59* (23), 15374.

(132)   Meisel, K.; Vocks, H.; Bobbert, P. Polarons in Semiconducting Polymers: Study within an Extended Holstein Model. *Phys. Rev. B* **2005,** *71* (20), 205206.

(133)   Kreouzis, T.; Poplavskyy, D.; Tuladhar, S.; Campoy-Quiles, M.; Nelson, J.; Campbell, A.; Bradley, D. Temperature and Field Dependence of Hole Mobility in Poly (9, 9-dioctylfluorene). *Phys. Rev. B* **2006,** *73* (23), 235201.